

**REPORT DOCUMENTATION PAGE**Form Approved  
OMB No. 074-0188

Public reporting burden for this collection of information is estimated to average 1 hour per response, including the time for reviewing instructions, searching existing data sources, gathering and maintaining the data needed, and completing and reviewing this collection of information. Send comments regarding this burden estimate or any other aspect of this collection of information, including suggestions for reducing this burden to Washington Headquarters Services, Directorate for Information Operations and Reports, 1215 Jefferson Davis Highway, Suite 1204, Arlington, VA 22202-4302, and to the Office of Management and Budget, Paperwork Reduction Project (0704-0188), Washington, DC 20503.

<b>1. AGENCY USE ONLY (Leave blank)</b>		<b>2. REPORT DATE</b> Jan. 1996	<b>3. REPORT TYPE AND DATES COVERED</b> Scientific paper	
<b>4. TITLE AND SUBTITLE</b>  Methane and Methanol Oxidation in Supercritical Water: Chemical Kinetics and Hydrothermal Flame Studies			<b>5. FUNDING NUMBERS</b>  DOE Contract No. DE-AC04-94AL85000	
<b>6. AUTHOR(S)</b> R.R. Steeper				
<b>7. PERFORMING ORGANIZATION NAME(S) AND ADDRESS(ES)</b>  Sandia National Laboratories Albuquerque, NM 87185 and Livermore, CA 94551			<b>8. PERFORMING ORGANIZATION REPORT NUMBER</b> SAND96-8208, UC-1409	
<b>9. SPONSORING / MONITORING AGENCY NAME(S) AND ADDRESS(ES)</b>  SERDP 901 North Stuart St. Suite 303 Arlington, VA 22203			<b>10. SPONSORING / MONITORING AGENCY REPORT NUMBER</b>  N/A	
<b>11. SUPPLEMENTARY NOTES</b> This paper prepared by Sandia National Laboratories, 1996. This work was supported in part by SERDP and the DOE under Contract No. DE-AC04-94AL85000.				
<b>12a. DISTRIBUTION / AVAILABILITY STATEMENT</b> Approved for public release: distribution is unlimited				<b>12b. DISTRIBUTION CODE</b> A
<b>13. ABSTRACT (Maximum 200 Words)</b> Supercritical water oxidation is an emerging technology for the treatment of wastes in the presence of a large concentration of water at conditions above water's thermodynamic critical point. A high-pressure, optically accessible reaction cell was constructed to investigate the oxidation of methane and methanol in the environment. Experiments were conducted to examine both flame and non-flame oxidation regimes. Optical access enabled the use of normal and shadowgraphy video systems for visualization, and Raman spectroscopy for <i>in situ</i> measurement of species concentrations.				
<b>14. SUBJECT TERMS</b> SERDP, Supercritical water, Methane oxidation, Raman spectroscopy, Methanol oxidation, Hydrothermal flame				<b>15. NUMBER OF PAGES</b> 159
				<b>16. PRICE CODE</b> N/A
<b>17. SECURITY CLASSIFICATION OF REPORT</b>  unclass.	<b>18. SECURITY CLASSIFICATION OF THIS PAGE</b>  unclass.	<b>19. SECURITY CLASSIFICATION OF ABSTRACT</b>  unclass.		<b>20. LIMITATION OF ABSTRACT</b> UL

NSN 7540-01-280-5500

Standard Form 298 (Rev. 2-89)  
Prescribed by ANSI Std. Z39-18  
298-102

DTIC QUALITY INSPECTED 1

# SANDIA REPORT

SAND96-8208 • UC-1409

Unlimited Release

Printed January 1996

## Methane and Methanol Oxidation in Supercritical Water: Chemical Kinetics and Hydrothermal Flame Studies

(Accepted in partial satisfaction of the requirements for the degree of Doctor of Philosophy in Engineering in the Office of Graduate Studies of the University of California, Davis.)

R. R. Steeper

Prepared by  
Sandia National Laboratories  
Albuquerque, New Mexico 87185 and Livermore, California 94551  
for the United States Department of Energy  
under Contract DE-AC04-94AL85000

Approved for public release; distribution is unlimited.

Issued by Sandia National Laboratories, operated for the United States Department of Energy by Sandia Corporation.

**NOTICE:** This report was prepared as an account of work sponsored by an agency of the United States Government. Neither the United States Government nor any agency thereof, nor any of their employees, nor any of the contractors, subcontractors, or their employees, makes any warranty, express or implied, or assumes any legal liability or responsibility for the accuracy, completeness, or usefulness of any information, apparatus, product, or process disclosed, or represents that its use would not infringe privately owned rights. Reference herein to any specific commercial product, process, or service by trade name, trademark, manufacturer, or otherwise, does not necessarily constitute or imply its endorsement, recommendation, or favoring by the United States Government, any agency thereof or any of their contractors or subcontractors. The views and opinions expressed herein do not necessarily state or reflect those of the United States Government, any agency thereof or any of their contractors or subcontractors.

This report has been reproduced from the best available copy.

Available to DOE and DOE contractors from:

Office of Scientific and Technical Information  
P. O. Box 62  
Oak Ridge, TN 37831

Prices available from (615) 576-8401, FTS 626-8401

Available to the public from:

National Technical Information Service  
U.S. Department of Commerce  
5285 Port Royal Rd.  
Springfield, VA 22161

SAND96-8208  
Unlimited Release  
Printed January 1996

**Methane and Methanol Oxidation in Supercritical Water:  
Chemical Kinetics and Hydrothermal Flame Studies**

(Accepted in partial satisfaction of the requirements for the degree of  
Doctor of Philosophy in Engineering in the Office of Graduate Studies of the  
University of California, Davis.)

R. R. Steeper  
Sandia National Laboratories  
P. O. Box 969  
Livermore, CA 94551-0969

**Abstract**

Supercritical water oxidation (SCWO) is an emerging technology for the treatment of wastes in the presence of a large concentration of water at conditions above water's thermodynamic critical point. A high-pressure, optically accessible reaction cell was constructed to investigate the oxidation of methane and methanol in this environment. Experiments were conducted to examine both flame and non-flame oxidation regimes. Optical access enabled the use of normal and shadowgraphy video systems for visualization, and Raman spectroscopy for *in situ* measurement of species concentrations.

Flame experiments were performed by steadily injecting pure oxygen into supercritical mixtures of water and methane or methanol at 270 bar and at temperatures from 390 to 510 °C. The experiments mapped conditions leading to the spontaneous ignition of diffusion flames in supercritical water. Above 470 °C, flames spontaneously ignite in mixtures containing only 6 mole% methane or methanol. This data is relevant to the design and operation of commercial SCWO processes that may be susceptible to inadvertent flame formation.

Non-flame oxidation kinetics experiments measured rates of methane oxidation in supercritical water at 270 bar and at temperatures from 390 to 442 °C. The initial methane concentration was nominally 0.15 gmol/L, a level representative of commercial SCWO processes. The observed methane concentration histories were fit to a one-step reaction rate expression indicating a reaction order close to two for methane and zero for oxygen. Experiments were also conducted with varying water concentrations (0 to 8 gmol/L) while temperature and initial reactant concentrations were held constant. The rate of methane oxidation rises steadily with water concentration up to about 5 gmol/L and then abruptly falls off at higher concentrations. A current elementary reaction mechanism designed for SCWO environments overpredicts rates observed in the kinetics experiments, but reproduces the observed downturn in reaction rate with increasing water concentration, albeit at too high a concentration.

## Acknowledgments

The work presented in this thesis was partially funded by the U.S. Department of Energy Office of Basic Science, Engineering and Geosciences Division. I am grateful to Dr. Oscar Manley for this extended support. Additional funding was provided by the Strategic Environmental Research and Development Program run by the Department of Energy, Department of Defense, and the Environmental Protection Agency.

I would like to acknowledge the contributions of my advisor at UC Davis, Professor Ian Kennedy, and the contributions of several colleagues at Sandia's Combustion Research Facility: Steven Rice, Tom Hunter, Alan Kerstein, Jason Aiken, John Hunter, Don Hardesty, George Fisk, and Sheridan Johnston.

I also am grateful for the help of Professor Barry Butler and Dr. Robert Schmitt at the University of Iowa, Professor Jeff Tester at MIT, and Dr. William Pitz at Lawrence Livermore Lab.

Finally, my family, Joan, Benjamin, and Stanley, deserves abundant acknowledgment for their super support.

# Table of Contents

<b>1. Introduction.....</b>	<b>1</b>
1.1. Definition of Supercritical Water Oxidation .....	1
1.2. Properties of Supercritical Water .....	2
1.3. Process Description .....	4
1.4. Supercritical Water Oxidation Research .....	6
1.5. Research Objectives .....	7
<b>2. Experimental Apparatus and Procedure .....</b>	<b>9</b>
2.1. High Pressure Reactor .....	9
2.1.1. Reaction Cell .....	9
2.1.2. Fluid Handling System.....	11
2.1.3. Oxygen Safety .....	12
2.2. Optical Diagnostic System .....	13
2.2.1. Shadowgraphy.....	13
2.2.2. Raman Spectroscopy.....	13
2.2.3. Emission Spectroscopy .....	14
2.3. Operating Procedures .....	15
2.3.1. Flame Experiments .....	15
2.3.2. Kinetics Experiments .....	17
2.4. Data Reduction .....	18
2.5. Assumptions .....	20
2.5.1. Raman Calibrations.....	20
2.5.2. Settling Times For Kinetics .....	20
2.5.3. Isothermal Assumption.....	24
2.5.4. Isobaric Assumption .....	25
<b>3. Hydrothermal Flame Experiments.....</b>	<b>27</b>
3.1. Introduction .....	27
3.2. Flame Phenomenology .....	28
3.2.1 Experimental Procedure.....	28
3.2.2. Flame Description .....	30
3.2.3. Flame Temperature .....	32
3.2.4. Flame Aspect Ratio .....	35
3.2.5. Flame Emission Spectra.....	38
3.3. Spontaneous Ignition Limits .....	40
3.3.1. Experimental Procedure.....	40
3.3.2. Experimental Results .....	40
3.3.3. Conclusions .....	43

<b>4. Methane Kinetics Experiments .....</b>	<b>45</b>
4.1. Introduction .....	45
4.2. Kinetics Measurements In Supercritical Water.....	46
4.2.1. Experimental Conditions .....	46
4.2.2. Experimental Procedure.....	49
4.2.3. Data Reduction .....	50
4.2.4. Experimental Results .....	51
4.2.5. Global Fit .....	55
4.3. Kinetics Measurements In Subcritical Water .....	63
4.3.1. Experimental Conditions .....	64
4.3.2. Experimental Procedure and Data Reduction .....	65
4.3.3. Experimental Results .....	65
4.3.4. Global Fit .....	69
4.4. Kinetics Measurements In Argon .....	73
4.5. Density Dependence of Kinetics .....	74
4.6. Conclusions .....	78
<b>5. Model Assessments .....</b>	<b>81</b>
5.1. Kinetics Models .....	81
5.2. Methane Model.....	82
5.3. Rate Prediction.....	85
5.4. Density Dependence .....	90
5.5. Flame Ignition Prediction.....	94
5.6. Conclusions .....	97
<b>6. Summary and Conclusions .....</b>	<b>99</b>
<b>7. Appendices .....</b>	<b>101</b>
7.1. Elementary Reaction Mechanism .....	101
7.2. Flame Ignition Experiments .....	107
7.2.1. Methane Hydrothermal Flame Ignition Trials.....	108
7.2.2. Methanol Hydrothermal Flame Ignition Trials .....	109
7.3. Methane Kinetics Experiments.....	111
<b>8. References.....</b>	<b>159</b>

# 1. Introduction

Supercritical water oxidation (SCWO) is an emerging waste treatment technology that has attracted interest from both industry and government agencies. Development of the technology began 15 years ago (Modell, 1989), and since that time, research efforts at universities, national labs, and in industry have revealed numerous advantages offered by the technology. Dozens of laboratory- and pilot-scale SCWO reactors have been built and operated in the course of this research. However, economic risks associated with the design and construction of full-scale equipment have delayed the commercialization of supercritical water oxidation until recently. The first full-scale commercial SCWO process has recently begun operation at a chemical research facility in Texas.

## 1.1. Definition of Supercritical Water Oxidation

Supercritical water oxidation is defined as the oxidation of organics in the presence of a large concentration of water at conditions above the critical temperature and pressure of water (374 °C, 221 bar). Process conditions typically entail temperatures ranging from 500 - 650 °C and pressures of 250 bar. Water at these conditions has a density about one-tenth that of liquid water and behaves for the most part as a dense gas. Combustion gases (O<sub>2</sub>, CO<sub>2</sub>, N<sub>2</sub>) and many organics are completely miscible in water at these densities. As a result, when an oxidizer (O<sub>2</sub>, air, or H<sub>2</sub>O<sub>2</sub>) is added to the waste and water, oxidation reactions proceed in a single-phase mixture.

Excellent destruction efficiencies at moderate temperatures and short residence times have been demonstrated for a long list of compounds (Tester, *et al.*, 1993a). The list includes simple compounds such as H<sub>2</sub>, CO, and CH<sub>4</sub>; common industrial chemicals such as ammonia, methanol, and methylene chloride; toxic compounds including chlorinated dioxins and furans; and surrogate mixtures that model the radionuclide-containing wastes found at several federal facilities (Bramlette, *et al.*, 1990). Solids are treatable as well, constrained only by the pumpability of the material. Feedstream organic concentration is governed by heat generation considerations, and typically ranges from 1 - 10 wt%. The oxidation products of simple hydrocarbons in supercritical water comprise CO<sub>2</sub> and H<sub>2</sub>O. If present in the waste, nitrogen is



primarily converted to  $N_2$ , and other heteroatoms and halides appear in the effluent as inorganic acid anions.

The advantages of SCWO are significant. In spite of moderate temperatures, reaction rates are relatively fast due to high reactant concentrations in the high-density environment. The high density also allows reduced reactor volumes compared to atmospheric pressure equipment—an advantage for the design of compact, on-line processing equipment or transportable units. In addition, the process is totally contained, which is a strong safety advantage in the handling of hazardous materials.

Limitations on the types and concentrations of wastes treatable by SCWO mean that this technology complements rather than competes with other waste-processing methods. At low organic loading, bioremediation or activated carbon technologies are technically and economically viable. Above 1 wt% organic, however, these technologies are not appropriate. At the other extreme of organic concentration, incineration can be effectively applied. But because of its elevated process temperature, incineration is not viable below about 25 wt% organic (Modell, 1989). The candidate materials for treatment with SCWO include aqueous waste streams that contain 1 - 10 wt% combustibles, materials that are pumpable when slurried with water (e.g. soil or coal wastes), and materials that are best handled in water for safety reasons (e.g., energetic materials).

## **1.2. Properties of Supercritical Water**

The supercritical region of water is shown in the phase diagram of Figure 1.1. The region contains no phase boundaries—it is a single phase region—and properties vary continuously with pressure and temperature. At high pressures, the supercritical region includes fluids at liquid-like densities; at high temperatures, it includes superheated steam with ideal-gas-like densities. Close to the critical point, the region's boundary demarks a zone of dramatic changes in physical properties with small changes in temperature and pressure.

Figure 1.2 illustrates the rapid drop in density that occurs as temperature is increased near  $T_{\text{critical}}$  for a fluid at 270 bar (Haar, *et al.*, 1984). At conditions typical of SCWO processes, the density is about one-tenth that of liquid water, but still 100 times more dense than steam at ambient pressure. An even more

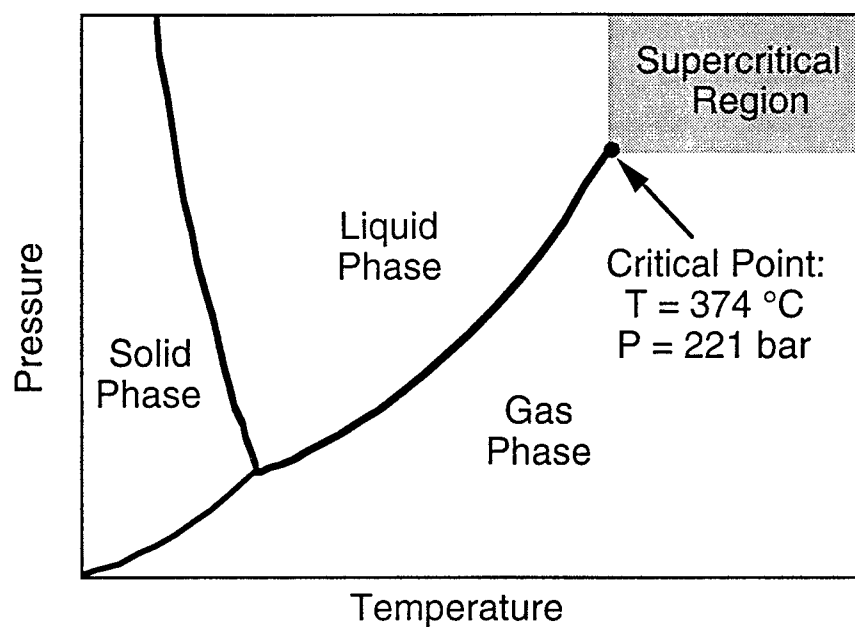


Figure 1.1. Phase diagram of water indicating the critical point and supercritical region.

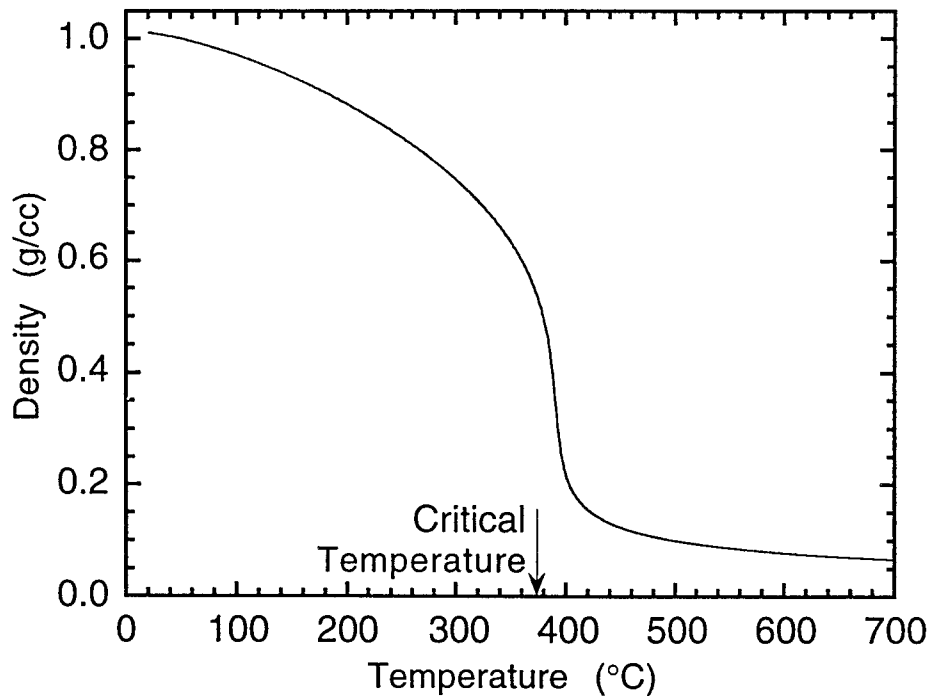


Figure 1.2. Density of water at P = 270 bar as a function of temperature.

dramatic change occurs in the ionic dissociation and dielectric constants along an isobar in this range. From the familiar value of  $10^{-14}$  at ambient temperature, the ionic dissociation constant drops six orders of magnitude by 400 °C (Marshall and Franck, 1981). The dielectric constant, a measure of molecular association, steadily decreases from a value of 80 to a value near 2 by 400 °C (Uematsu and Franck, 1980). As a result of these significant changes, the solvation properties of water change dramatically as well. Many hydrocarbons, such as benzene, that are normally insoluble in liquid water exhibit high solubility in supercritical water, even at liquid-like densities (Franck, 1987). In addition, combustion gases such as CO<sub>2</sub>, O<sub>2</sub>, and N<sub>2</sub> are completely miscible in this environment (Connolly, 1966). On the other hand, solubilities of inorganic salts are often low (Martynova, 1976), making the separation of such materials feasible in a SCWO process.

The miscibility of organics and combustion gases in supercritical water means that oxidation reactions can take place in a single-phase environment without the limitations of interphase transport. Furthermore, transport properties in the supercritical phase are favorable for chemical reaction as well. Despite high densities, diffusivities remain high (Lamb, *et al.*, 1981), and viscosities low (Haar, *et al.*, 1984).

### **1.3. Process Description**

Many different configurations of the supercritical water oxidation process have been designed and built, including tubular reactors, tank reactors, and batch reactors. Most can be represented, however, by the simple schematic in Figure 1.3. The components of the generic process in Figure 1.3 can be divided into three sections: pump and preheater, reactor, and cooldown and separation.

In the pump and preheater section, two parallel lines handle the waste and oxidizer streams separately. The waste stream is a mixture of water plus combustible waste at an appropriate concentration. The oxidizer can be liquid oxygen, air, or hydrogen peroxide, although the latter is seldom economically viable. Each of the two streams is preheated sufficiently to assure initiation of reaction upon mixing. The point of mixing of the two streams depends on the nature of the waste stream. If the waste has a tendency to char upon heating, the two streams can be mixed during, or even before, preheating. In other cases, mixing takes place after both streams are at supercritical conditions to facilitate

complete mixing. The mixing strategy is important since chemical reactions that are initiated in the mixing zone can range from controlled, distributed reactions to diffusion flames, and even explosions.

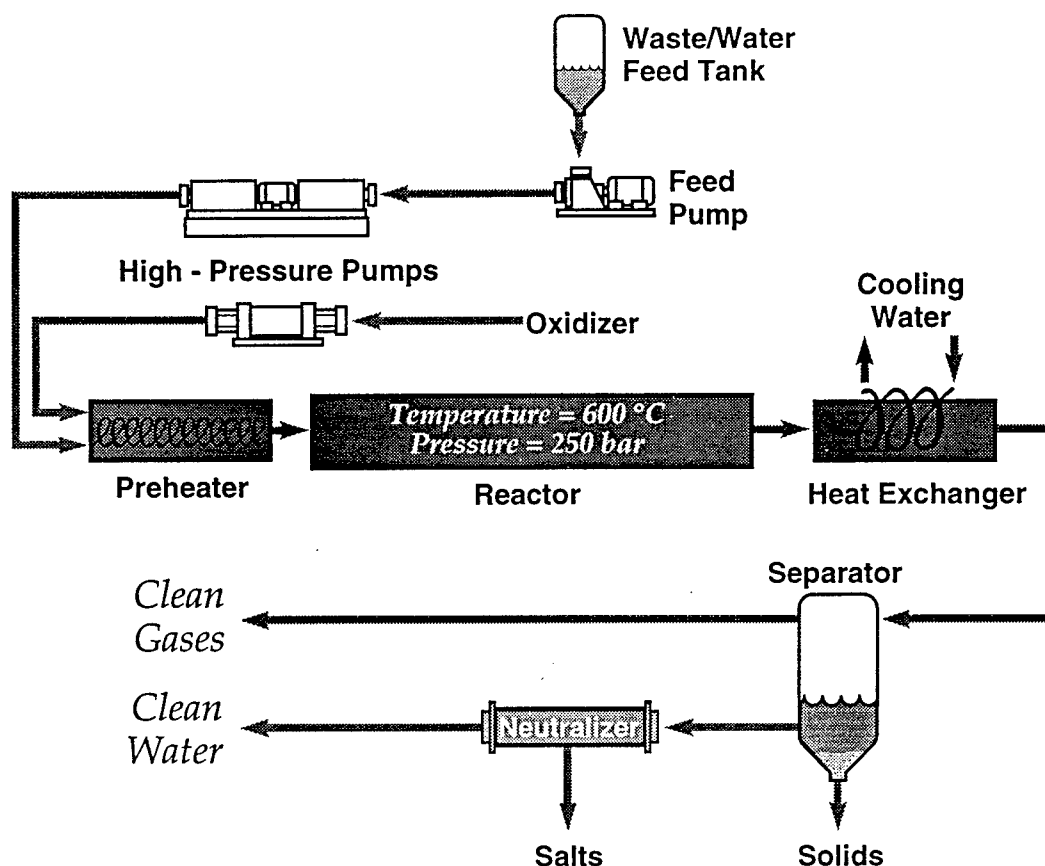


Figure 1.3. Schematic of a generic supercritical water oxidation process.

The reactor section is typically made of a high-nickel superalloy such as Inconel or Hastelloy which offers strength combined with corrosion resistance at elevated temperatures. Tubular reactors are common, although the problem of plugging by salt formation must be addressed (Armellini and Tester, 1991). Alternatively, tank reactors with water-flushed walls have been built to address both corrosion and plugging issues (Barner, *et al.*, 1992). The reactor is sized to provide adequate residence time for complete destruction of the hazardous components; typical residence times are in the range of ten seconds.

Following reaction, the stream passes into the cooldown and separation section. Depending on the contents of the waste stream, separators can be located on either side of the heat exchanger. For salts that are insoluble in

supercritical water, a separator operating prior to cooldown is effective. For wastes with sufficient heat content, the heat exchanger can be used to transfer energy to the feed streams in the preheater section. Additionally, processes have been designed to include steam generators and turbines to extract energy for use in the compression of the oxidizer feedstream (Thomason and Modell, 1984). The separator following cool down separates gaseous and liquid products. The gases are primarily CO<sub>2</sub> and N<sub>2</sub>, with possible inclusion of small amounts of carbon monoxide and nitrous oxide. The liquid effluent is principally water but may contain acids and some redissolved salts requiring an additional treatment step as indicated in the schematic.

#### **1.4. Supercritical Water Oxidation Research**

A wide variety of research projects has supported the development of supercritical water oxidation. Early experiments were mostly concerned with establishing destruction efficiencies (percent of parent material destroyed in a given residence time) to catalog compounds appropriate for treatment with SCWO technology (Modell, 1989). Since then, the need to understand reaction chemistry has motivated extensive research. Several research groups have performed experiments to determine oxidation kinetics rates in supercritical water. At MIT, researchers have published extensive plug flow reactor results for a variety of simple organic compounds including carbon monoxide (Helling and Tester, 1988; Holgate, *et al.*, 1992; Holgate and Tester, 1994a; Holgate and Tester, 1994b), hydrogen (Holgate and Tester, 1993; Holgate and Tester, 1994a; Holgate and Tester, 1994b), methane (Webley and Tester, 1991), methanol (Webley and Tester, 1989; Webley, *et al.*, 1991; Tester, *et al.*, 1993b), and ammonia (Helling and Tester, 1988; Webley, *et al.*, 1991). Thornton and Savage (1990, 1992) at Michigan examined the kinetics of phenol at near-critical and supercritical conditions in a flow reactor. Wightman (1979) performed flow reactor experiments and extracted global rate expressions for acetic acid and phenol. A group at the University of Texas at Austin also examined the kinetics of acetic acid and phenol in a batch reactor (Lee, *et al.*, 1990; Lee and Gloyna, 1990). At Sandia, experiments in a SCWO flow reactor provided data on a number of organics including methanol, phenol, and other industrial chemicals as well as military munitions (Rice, *et al.*, 1993; Rice, *et al.*, 1994).

Commercial SCWO processes are designed to be flameless: wastes are destroyed through oxidation reactions at temperatures typically less than 700 °C. Most prior research has examined this oxidation regime. However, Franck and colleagues at Karlsruhe, Germany demonstrated the existence of stable, high-temperature flames (*hydrothermal* flames) in supercritical water-fuel-oxygen mixtures (Schilling and Franck, 1988). In a mixture of 30 mole% methane in supercritical water, for example, he found that flames spontaneously ignited upon injection of oxygen. The flames were qualitatively described in this work, but no attempt was made to determine the limits of ignition in the temperature, pressure, and concentration range associated with SCWO processes. The possibility of more than a single oxidation regime in SCWO processes is a potentially important design consideration.

### **1.5. Research Objectives**

The present research project has been motivated by several goals: to understand the physics and chemistry controlling oxidation in supercritical water; to contribute to combustion science by performing fundamental studies in a unique environment; and to advance the development of new environmental and energy technologies. The project comprises research in two related areas: experimental investigations of diffusion flames in supercritical water, and experimental measurements of chemical kinetics rates in supercritical water. Specific objectives of this research are listed below.

1. Characterize the phenomenology of hydrothermal diffusion flames.
2. Map the limits of spontaneous ignition of such flames in the range of conditions characteristic of SCWO processes.
3. Measure the oxidation kinetics of methane in supercritical water at concentrations representative of commercial SCWO processes.
4. Evaluate the ability of existing reaction mechanisms to predict both the hydrothermal flame ignition data and the kinetics data.

## 2. Experimental Apparatus and Procedure

### 2.1. High Pressure Reactor

#### 2.1.1. Reaction Cell

An optically accessible high-pressure reaction cell (referred to as the SCW reaction cell, or reactor) was used to conduct both flow and batch experiments. In the flow configuration, used for the study of hydrothermal diffusion flames, the reactor was held at constant pressure using a back-pressure regulator. In batch configuration, used to measure oxidation rates, the reactor was sealed off and measurements were made at constant volume.

Figure 2.1 is a cutaway schematic of the SCW reaction cell. It is constructed of Inconel 718, an alloy offering strength and corrosion resistance at elevated temperatures. The 718 alloy rather than the more commonly used Inconel 625 was chosen for its hardenability. This property is used to advantage in the design of the main seal as described below. Three cylindrical arms with outside diameter of 7.6 cm protrude from the center of the reactor. Each houses a window and main seal assembly that provides optical access to the 18-mL reaction chamber. Five high-pressure ports (Autoclave type F-250-C) located radially around the center of the reactor are used for adding and removing fluids at pressures as high as 350 bar. In addition, the ports accommodate 1.6-mm-diameter, Inconel-sheathed thermocouples. Each arm is fitted with a 700-W electrical band heater and the whole reactor is wrapped in alumina insulation allowing operation at temperatures as high as 550 °C.

Two types of seals, visible in Figure 2.1, are used in the reactor. The main seal relies on a knife-edge, metal-to-metal design. Two slightly mismatched bevels on the main seal and the reactor body intersect along a line (circle) to generate the required contact pressure. Use of Inconel 718 allows hardening of the reactor body so that contact deformation occurs primarily on the main seal. Periodically the main seal is reconditioned by polishing it on a lathe. A large preload by the threaded clamp is necessary to prevent leaks since reactor pressure unloads this seal. Not shown in the figure are Belleville washers located between the main seals and the clamps that maintain uniform thrust on the seal during unequal thermal expansion of the sapphire and metal parts. The second

type of seal takes advantage of reactor pressure to press the sapphire windows against an annular surface on the main seal. The mating surfaces are ground optically flat and a 0.25-mm-thick gold washer is inserted between them. A threaded cap preloads the assembly for initial sealing.

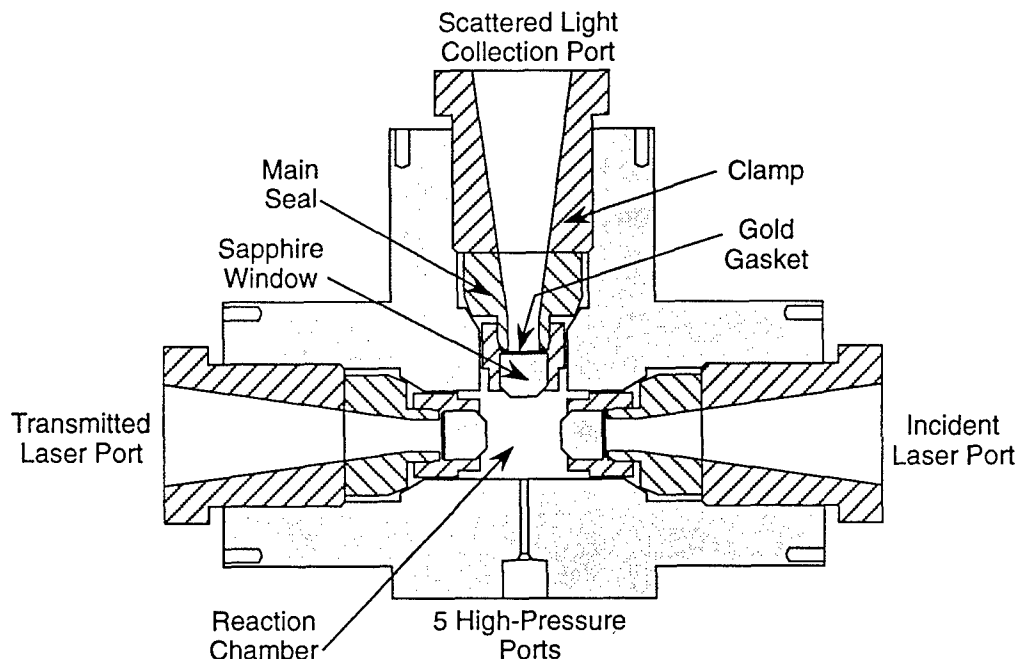


**Figure 2.1. Cutaway view of the supercritical water reaction cell as seen from the top.**

The three reactor windows are made of synthetic sapphire with a clear aperture of 7.6 mm. They are mounted in a seal assembly that provides a numerical aperture (sine of the half-angle) of 0.14. Normally, sapphire windows used for laser transmission are fabricated with their optical axes oriented parallel to the direction of propagation to eliminate birefringence effects. However, the optical axes of the sapphires obtained for these experiments weren't oriented accurately enough: as sapphire thickness varied due to drift in reactor temperature, the polarization of the transmitted laser beam changed significantly, affecting diagnostic outputs. To remedy the problem, the sapphires are carefully mounted in the seal assembly with their optical axes in the (vertical) plane of laser polarization so that birefringence effects are rendered insignificant.

The SCW reactor is mounted on translating stages with the window axes in the horizontal plane. The stages allow vertical movement and horizontal movement along the laser port axis. The whole assembly is isolated within a 1.9-



cm-thick steel barricade to protect operators in the case of window or tubing failure.

### 2.1.2. Fluid Handling System

Figure 2.2 presents a simplified schematic of the high-pressure fluid handling system. A high-pressure liquid chromatography (HPLC) pump (LDC Analytical ConstaMetric 3200 or Rainin Rabbit HP) is the main pressure-generating device. It delivers up to 10 mL/min of liquid water at pressures to 550 bar. Water from the pump can be directly injected into the reactor or it can be used to pressurize gases for injection. For this purpose, two stainless steel cylinders are fitted with pistons, with water on one side of the pistons and the gas to be compressed on the other side. One piston-cylinder is reserved for fuel gases and the other for oxygen. A 690-bar, manual piston-screw pressure generator (HiP Company) is also installed as an alternative pressurizing device; it is used to inject liquid fuels. During injection of fluids, a Tescom 690-bar back-pressure regulator can be used to maintain constant pressure in the cell.

Pressure in the reaction cell is monitored with Teledyne Taber pressure transducers—Model 2105 for pressures to 350 bar, and Model 2404 for pressures below 70 bar. Repeatability for both transducers is given as 0.1% of full-scale output, but resolution of the digitizing hardware is 3 bar for the high-pressure transducer. Fluid temperature is monitored with a 1.6-mm-diameter, Inconel-sheathed, type R thermocouple inserted 13 mm into the reaction chamber. Additional thermocouples monitor cell skin temperature to prevent overheating. A microcomputer continually records pressure and temperatures while controlling reactor heating, monitoring laser power, and ensuring safe operation of the experiment.

Stainless steel and Inconel 625 tubes connect the high-pressure components, with Inconel used for the high-temperature locations close to the reactor. High-temperature shut-off valves are used for the exhaust lines, although these components stay cool during venting due to the relatively small mass of the reactor contents. Tubing located between the reactor and the shut-off valves is small diameter (3.2-mm outside diameter, 0.48-mm inside diameter) in order to reduce unheated volume that is in communication with the reactor during experiments. The volume of this unheated tubing and associated fittings (including a burst disk assembly) is 3.0 mL.

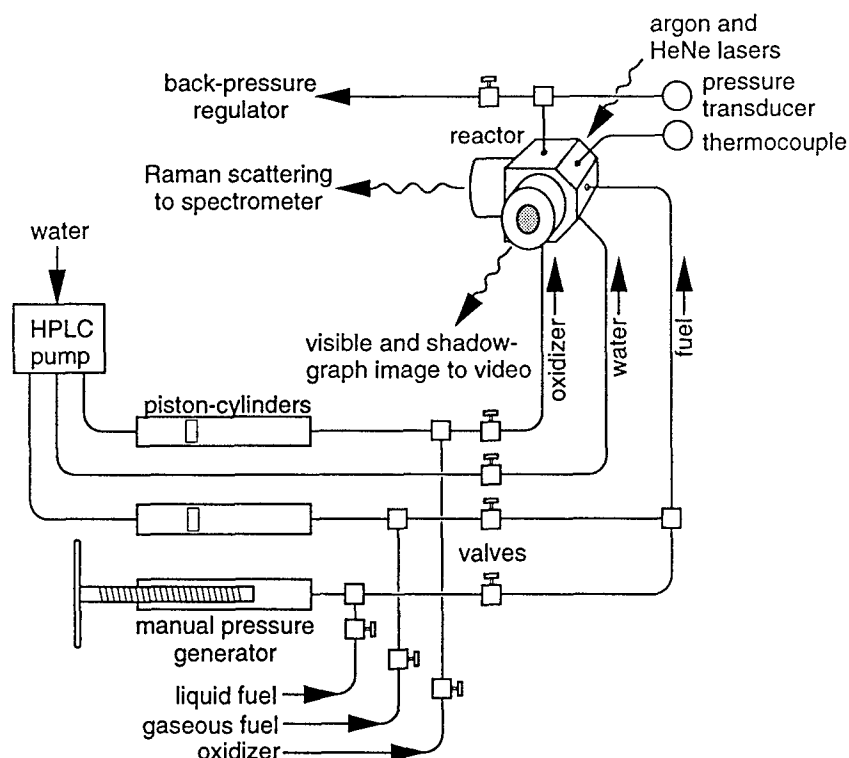


**Figure 2.2. Schematic diagram of the fluid handling system connected to the supercritical water reactor.**

### 2.1.3. Oxygen Safety

Extensive measures have been taken to reduce the risks associated with high-pressure combustion experiments, especially those involving the use of pure oxygen. The fluid handling system has been designed and assembled to minimize these risks. All components wetted by oxygen are constructed of compatible materials (ASTM, 1990; ASTM, 1987; ASTM, 1988a), and have been cleaned following ASTM recommendations (ASTM, 1988b). The oxygen injector assembly is a tube-within-a-tube design, with the inner capillary tube made of monel to reduce the likelihood of ignition, and the outer tube made of Inconel for strength. The reactor and all high-pressure oxygen tubing are enclosed within secondary shields, and operational procedures restrict the volume of high-pressure (340-bar) oxygen to 50 mL. Separate vent lines isolate the various gases to prevent possible reaction during venting.

## **2.2. Optical Diagnostic System**

### **2.2.1. Shadowgraphy**

The three sapphire windows permit monitoring of the reaction chamber with a variety of optical diagnostics. A video camera mounted at the transmitted laser port records visible emission during the flame experiments. Simultaneously, the camera records shadowgraph images created with a collimated, low-power HeNe laser beam that backlights the reaction chamber. At typical experimental densities, the shadowgraph images reveal details of injection jets, phase separation, mixing processes, and buoyant plumes. With a long-pass filter placed in front of the video camera to block the argon laser (used for Raman spectroscopy), shadowgraph and Raman diagnostics can be run simultaneously.

### **2.2.2. Raman Spectroscopy**

Spontaneous Raman spectroscopy is a convenient diagnostic for experiments in supercritical water. High fluid densities yield strong Raman signals that can be used to determine concentrations as well as temperatures (Brown and Steeper, 1991). For our flame experiments, this diagnostic was used to establish initial and final mixture composition, while for our kinetics experiments, concentrations as a function of time were determined for stable as well as intermediate species. A diagram of the Raman system is shown in Figure 2.3.

The Raman system used in the flame experiments incorporated a Spectra Physics Model 166 continuous wave argon ion laser producing 1.5 W at 514.5 nm. To increase signal strength and allow shorter exposures, a Spectra Physics Model 171 tuned to 488 nm was used in the kinetics experiments. With the probe beam focused to 230  $\mu\text{m}$ , the maximum usable power was about 5 W. At higher fluxes, localized heating caused formation of deposits on the inner window surfaces during experiments, provoking increased heating and accelerated damage to the window. In extreme cases, as during an abortive attempt to use a pulsed Nd:YAG laser, high fluxes led to window failure.

Raman-scattered light is collected using an f/3 lens and directed into a Spex 1404 0.85-m double monochromator with 1800-groove/mm holographic gratings. A Spex CD2A controller is used to position the gratings. To record

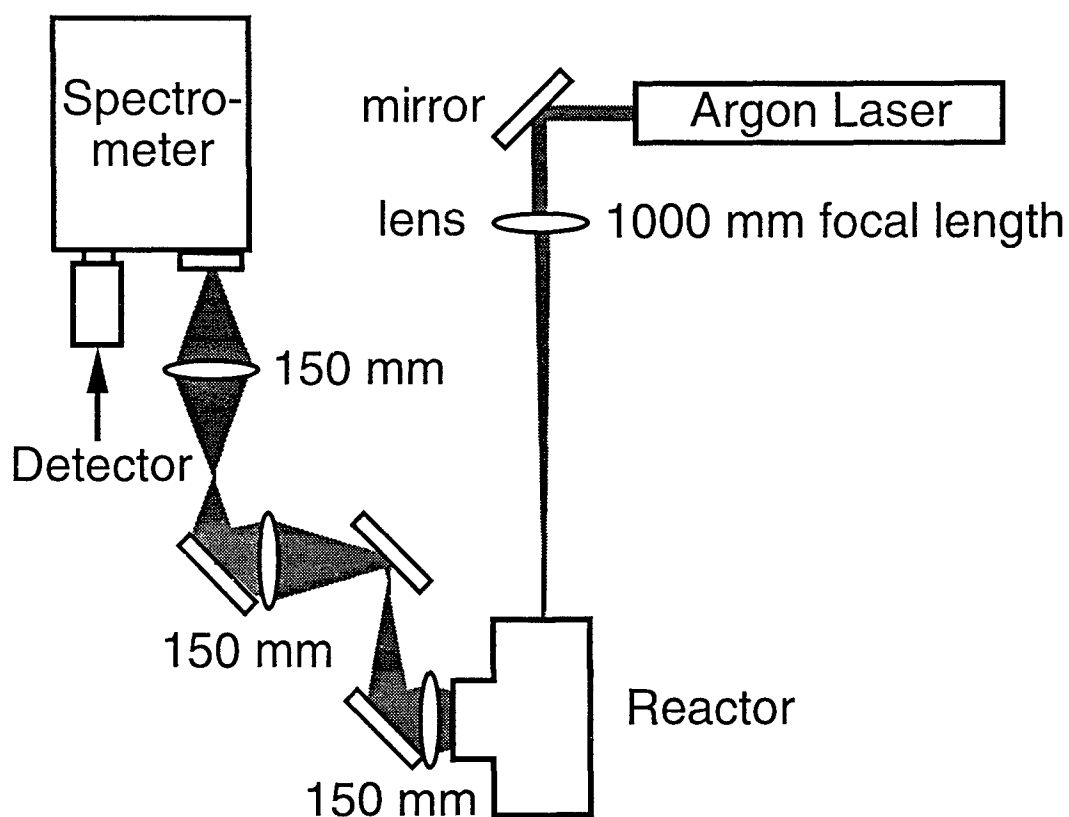


Figure 2.3. Schematic of Raman spectroscopy optics setup.

spectra, a Princeton Instruments IRY-1024 intensified diode array detector is mounted on the spectrometer's exit port. Spectrometer and detector settings for the various species of interest are shown in Table 2.1. The linear array detector with its 1024 diodes measures 25 mm, and the dispersion of the spectrometer is such that the detector covers 6.2 nm of the dispersed spectrum. The slit width settings chosen for the experiments correspond to spectral resolutions between 0.05 and 0.1 nm which are sufficient for the integral analysis technique used (described in Section 2.4). A microcomputer controls the spectrometer drive, reads the detector, and stores the Raman spectra for subsequent analysis.

### 2.2.3. Emission Spectroscopy

During certain flame experiments, a J-Y model CP 200, low-dispersion spectrograph was substituted for the larger spectrometer to record visible flame emission spectra. A 133-groove/mm grating mounted in this instrument disperses wavelengths from 300 to 1200 nm over the 25.4-mm width of the Princeton Instruments detector.

Species	Raman Shift (cm <sup>-1</sup> )	Exposure Time (s)
CH <sub>4</sub>	2915	5 - 20
CH <sub>3</sub> OH	2839	5 - 20
O <sub>2</sub>	1556	20
CO <sub>2</sub>	1388	20
N <sub>2</sub>	2331	20
CO	2145	20 - 30
CH <sub>2</sub> O	2778	30
H <sub>2</sub>	4160	30

Table 2.1. Typical spectrometer and detector settings for Raman diagnostic measurements.

## **2.3. Operating Procedures**

### **2.3.1. Flame Experiments**

The initial step in the flame experiments is calibration of the Raman system. The gas to be calibrated (CH<sub>4</sub>, O<sub>2</sub>-N<sub>2</sub> mixture, CO<sub>2</sub>, or CO) is loaded into the preheated reactor. Raman spectra are recorded at several pressures corresponding to the range of densities encountered during the experiments (from 2 - 50 bar). As discussed in Section 2.5.1, this data establishes the calibration relationship between concentration and Raman signal.

The next step in the flame experiments involves loading water into the hot reactor. Commercial distilled water is injected using the HPLC pump at a rate of about 3 standard mL/min. A back-pressure regulator is connected to the reactor vent line so that pressure rises and then is held at the preset pressure. Injection is continued for several minutes to purge any residual gases. Once water injection is complete, the reactor is closed and allowed to equilibrate for at least an hour.

When reactor temperature and pressure are stable, background Raman spectra are recorded for each of the species to be monitored. These spectra, recorded in pure water at the experimental density, are subsequently subtracted from spectra of the monitored species recorded later in the experiment.

The next step is to create a water-fuel mixture at the desired initial concentration. (As described later, oxidizer is injected into a fuel mixture in these experiments—rather than the other way around—to create an *inverse* diffusion flame.) The reactor vent is opened to the back-pressure regulator and an estimated amount of fuel is injected using the piston-cylinder or manual pressure generator. Following fuel addition, continual monitoring of the Raman signal indicates when mixing is complete: typically, this occurs in less than 5 minutes. A spectrum recorded at this time determines the initial fuel concentration.

The oxidizer used in the flame experiments is pure oxygen. Once the temperature, pressure, and fuel concentration are stable, oxygen pressure in the piston-cylinder is adjusted via the HPLC pump to match reactor pressure. At this point, oxygen injection can begin. Room temperature, high-pressure oxygen is injected at about 1 mL/min through a capillary tube located in the bottom port

Quantity	Symbol	Value	Unit
mass flow	$\dot{m}$	0.0059	gm/s
diameter	$d$	.05	cm
inlet temperature	$T_{in}$	303	K
exit temperature	$T_{out}$	673	K
reactor temperature ~ O <sub>2</sub> tube temp	$T_{reac}$	703	K
mean temperature = $(T_{out} + T_{in})/2$	$T_m$	487	K
log mean temperature = $(T_{out} - T_{in})/\ln[(T_{reac} - T_{in})/(T_{reac} - T_{out})]$	$T_{ln-mean}$	144	K
specific heat @ $T_{mean}$	$c_p$	3.73	J/g-K
thermal conductivity	$k$	0.0492	W/m-K
average Nusselt number	$Nu$	3.66	
average convection coefficient	$h$	0.0360	W/cm <sup>2</sup> -K
energy equation: $q = h\pi dL\Delta T_{ln-mean} = \dot{m}c_p(T_{out} - T_{in})$			
$T_{reac} - T_{out}$	$\Delta T$	30	K
predicted heating length	$L_{pred}$	10.1	cm
actual heating length	$L$	10	cm

Table 2.2. Heat transfer calculation for an experiment at 430 °C. The exit temperature for the O<sub>2</sub> flow ( $T_{out}$ ) is guessed and the required heating length is predicted using the energy equation.

of the reactor. The oxygen is preheated as it enters the reactor: the sample heat transfer calculation in Table 2.2 estimates an exit temperature within 30 °C of the fluid inside the reactor. The exit Reynolds number is about 350, indicating the jet is laminar. Depending on chosen initial conditions, a diffusion flame spontaneously ignites and burns for up to 15 minutes. If conditions are such that no ignition occurs, oxygen injection is halted after 30 seconds as a safety precaution.

### 2.3.2. Kinetics Experiments

Calibration of the Raman system for kinetics experiments is the same as described for the flame experiments. Loading the water and fuel is similar except that the process is carried out with all reactor vent valves closed, i. e., at constant volume. Filling and venting several times with water ensures that only water is present. Final filling is stopped 40 - 50 bar below the target pressure; the remainder of the total pressure comes from fuel and oxidizer added subsequently. Following a suitable delay for composition and temperature stabilization, background spectra are obtained.

Starting with a piston-cylinder loaded with fuel and compressed to reactor pressure, the valve is opened and the HPLC pump pushes in an approximate amount of fuel. Monitoring the Raman signal indicates when the water-fuel mixture is at the desired composition (typically 0.15 gmol/L fuel), mixing is complete, and temperature is stable. Pressure is adjusted as needed depending on the amount of oxygen to be added subsequently. A final spectrum is recorded to establish the initial water-fuel composition.

The oxidizer chosen for the kinetics experiments is a 49 - 51 mole% mix of oxygen and nitrogen. This mix is less likely to cause auto ignition of flames, is safer to work with, and provides an inert fiducial signal (N<sub>2</sub> spectrum) to monitor Raman system drift. To begin the experiment, the oxidizer is quickly injected into the reactor (20 - 60 seconds) until the desired total pressure is reached. Following injection, Raman spectra for each of the monitored species are recorded in a continuous series until either the fuel or oxidizer are depleted—from 5 minutes to several hours. Reactor temperature and pressure are recorded simultaneously with the spectra.

## 2.4. Data Reduction

Data reduction consists mainly of manipulating the experimental Raman spectra to extract species concentrations. As described in Section 2.3.1, a species-specific background spectrum is subtracted from each experimental spectrum. Subtraction of this pre-recorded background can't compensate for any broadband radiation generated during the experiment. To eliminate this noise, a baseline is determined by least squares fit to data on each side of the spectral peak of interest. Then the integrated area between the baseline and the Raman peak becomes the species' integrated intensity. Figure 2.4 presents a typical experimental Raman spectrum of methane along with the calculated baseline.

To determine the Raman calibration for a given experiment, the calibration spectra are first integrated. For these spectra, the corresponding concentrations are determined from temperature and pressure data using the ideal-gas equation of state (EOS). At the conditions of the calibration runs, the ideal-gas EOS is accurate within 1.5%. Then the concentrations and corresponding integrated areas are fit with a straight line as shown in Figure 2.5. These calibration fits can then be used to convert Raman measurements made during the experiments to concentrations.

Integrated Raman intensities from the experiments are first corrected for laser power variations (monitored at the laser head) and then converted to concentrations using the calibration fits. Conversion of concentrations to mole fractions is done with a hybrid technique based on the Christoforakos-Franck equation of state (CF-EOS) (Christoforakos and Franck, 1986) designed to accommodate supercritical fluid mixtures. Christoforakos and Franck present data confirming the accuracy (within 10%) of the CF-EOS in predicting excess volumes for mixtures of supercritical water and methane. On the other hand, empirical equations of state are published for specific volumes of both pure water (Haar, *et al.*, 1984) and pure methane (Sychev, *et al.*, 1987) that are more accurate than can be predicted by the CF-EOS. In the hybrid technique used for the flame data, the two empirical EOSs are used to calculate volumes of the pure components. Then the sum of these two volumes is corrected using excess volumes from the CF-EOS. This method can't be used for methanol-water mixtures since the literature does not contain an empirical EOS for methanol at elevated pressures. For those mixtures, the CF-EOS is used as published.



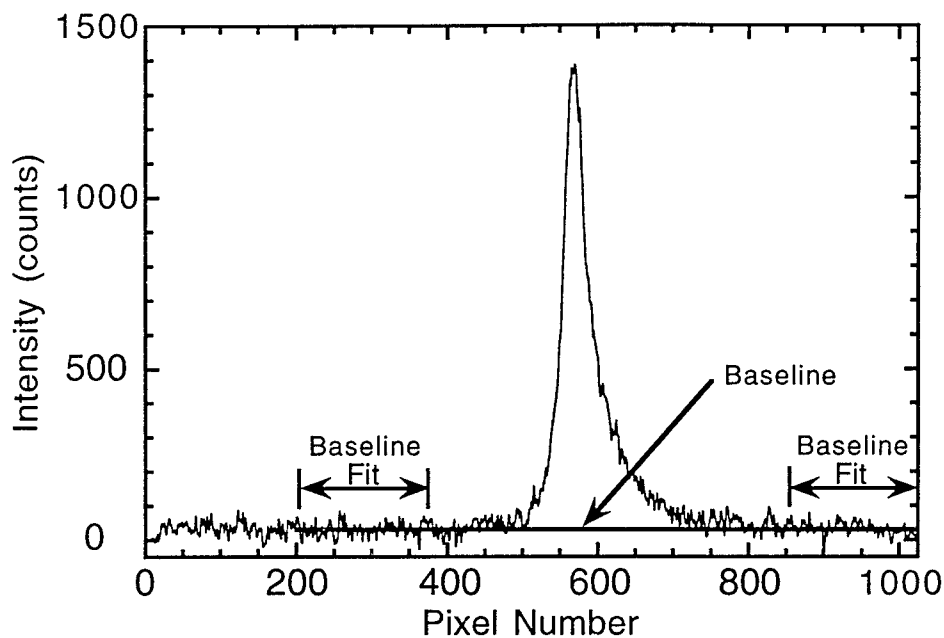


Figure 2.4 Raman spectrum of 0.04 gmol/L methane in a supercritical water-fuel-oxidizer mixture at 411 °C and 266 bar. A baseline has been fit for purposes of integration.

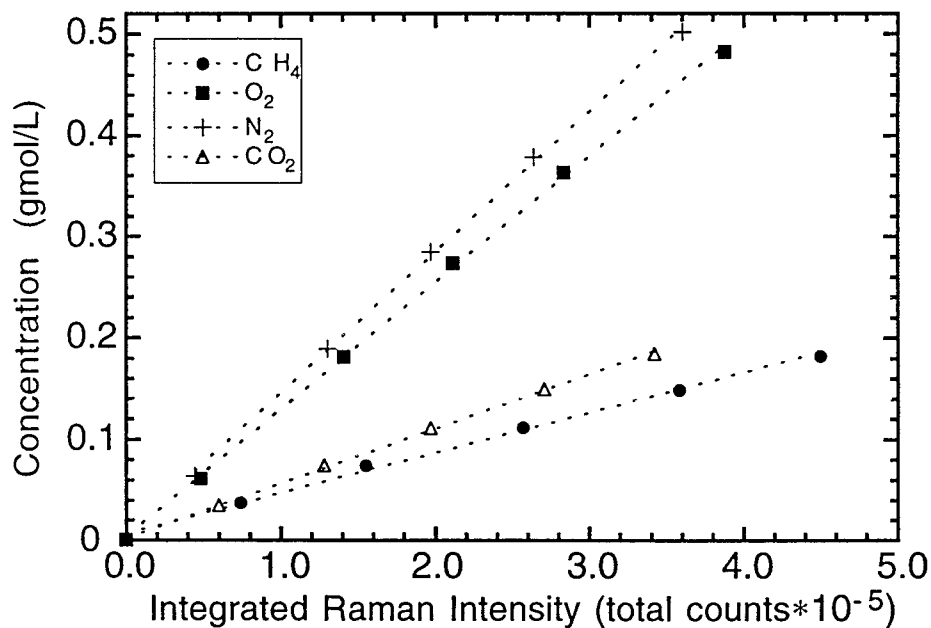


Figure 2.5. Typical Raman data for pure calibration gases. Exposure times (multiple exposures are averaged): CH<sub>4</sub> = 5 exposures @ 4 s; O<sub>2</sub> = 2 @ 10 s; N<sub>2</sub> = 2 @ 10 s; CO<sub>2</sub> = 1 @ 20 s. Symbols = experimental data; dashed lines = least squares fits.

## **2.5. Assumptions**

### **2.5.1. Raman Calibrations**

As described above, calibrations determined from pure gas spectra are used to determine concentrations in fluid mixtures. This method assumes that the Raman integrated intensities at a constant temperature are linearly dependent on concentration and independent of mixture water density. To verify this assumption, the following experiment was performed.

Pure methane was loaded into the reactor at 410 °C and 35.5 bar, and Raman spectra were recorded. The corresponding methane concentration was representative of values used in the flame experiments (~0.6 gmol/L). An incremental amount of water was then added at constant temperature, and new spectra were recorded. This procedure was repeated until total pressure exceeded 280 bar. Figure 2.6 shows the first and last spectra recorded during the experiment. There are obvious changes in the lineshape as pressure is increased: the peak broadens and its amplitude drops. Despite these changes, the integrated intensities remain constant. The integration results are shown in Figure 2.7—they are constant within  $\pm 5\%$  after an initial drop that is due to pure methane being pushed out of the reactor into attached tubes. The data thus justify the use of pure methane Raman spectra to calibrate measurements made in mixtures of methane plus water. CH<sub>3</sub>OH, O<sub>2</sub>, N<sub>2</sub>, and CO<sub>2</sub> were not checked independently—they are assumed to behave similarly.

Calibrations for CH<sub>4</sub>, CH<sub>3</sub>OH, O<sub>2</sub>, N<sub>2</sub>, and CO<sub>2</sub> were performed as necessary before each experiment. Carbon monoxide on the other hand was only calibrated during two experiments. From those experiments, a ratio relating carbon monoxide and nitrogen calibration constants (slopes) was established. This ratio was then used to calculate carbon monoxide concentrations for all the experiments that did not include carbon monoxide calibrations.

### **2.5.2. Settling Times For Kinetics**

An important source of uncertainty in the kinetics experimental data arises during system settling time following injection of the oxidizer. Since data analysis assumes mixture homogeneity, it is important to quantify deviations from this assumption. To isolate the temperature and composition deviations due to injection rather than chemistry, experiments were conducted with inerts

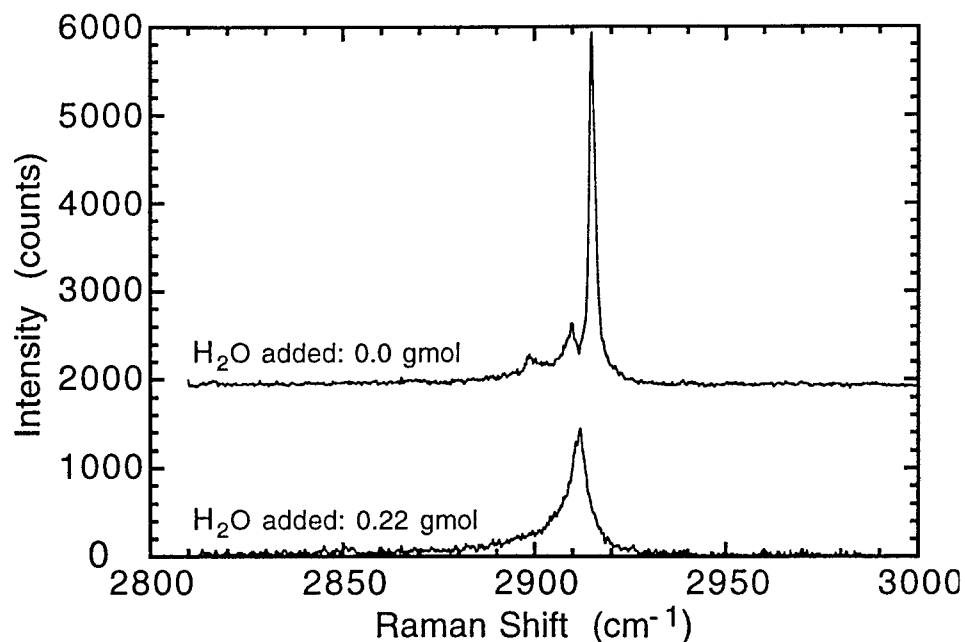


Figure 2.6. Raman spectra of the  $\nu_1$  mode (symmetric C-H stretch) of 0.62 gmol/L methane. Top curve (with artificial offset):  $P = 35.2$  bar,  $T = 409$  °C. Bottom data:  $P = 282$  bar,  $T = 412$  °C.

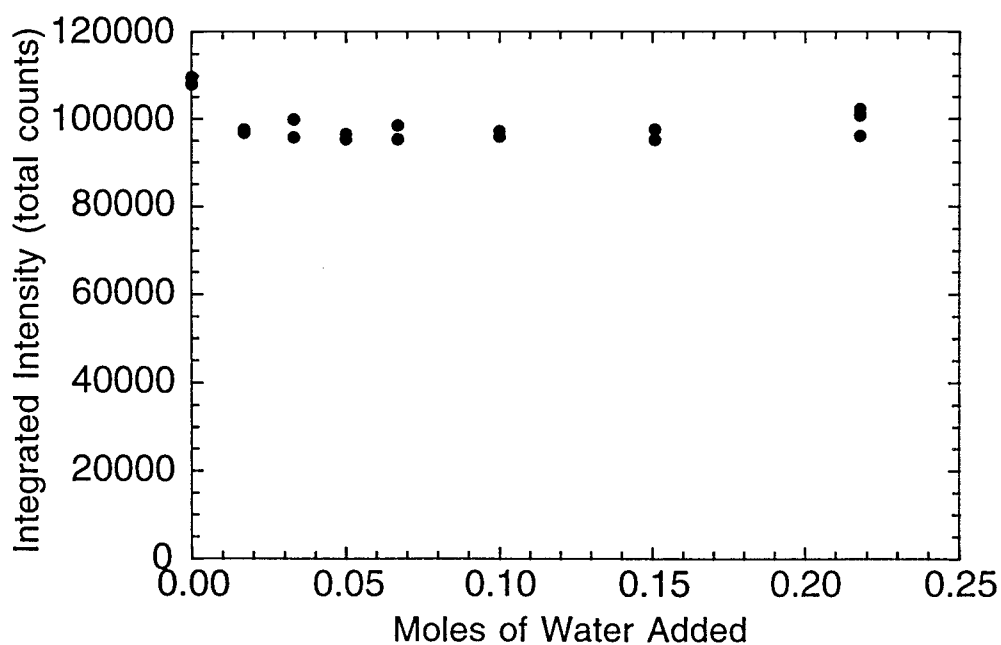


Figure 2.7. Integrated intensities of methane Raman spectra recorded as water was incrementally added to an initial load of pure methane. The first and last data points represent integrations of the spectra shown in Figure 2.6.

substituted for either oxygen or methane. Because the amount of oxidizer injected was small and preheating occurred in the injection tube, the resulting observed temperature fluctuations were less than 2 °C. Composition fluctuations on the other hand were significant in some cases.

Figure 2.8 presents results from an experiment that typify behavior at 270 bar. In this experiment, nitrogen, replacing the usual O<sub>2</sub>-N<sub>2</sub> mixture, was injected at constant volume into a mixture of methane and water. An initial depression of methane concentration is visible: this is due to higher local concentration of nitrogen along the injector axis. However, mixing is rapid, and methane concentration quickly returns to its initial value. A series of such experiments indicates that mixture composition is homogeneous within 3 minutes of the start of injection in experiments at  $T \geq 405$  °C. At temperatures around 390 °C, mixing time increases to 5 minutes.

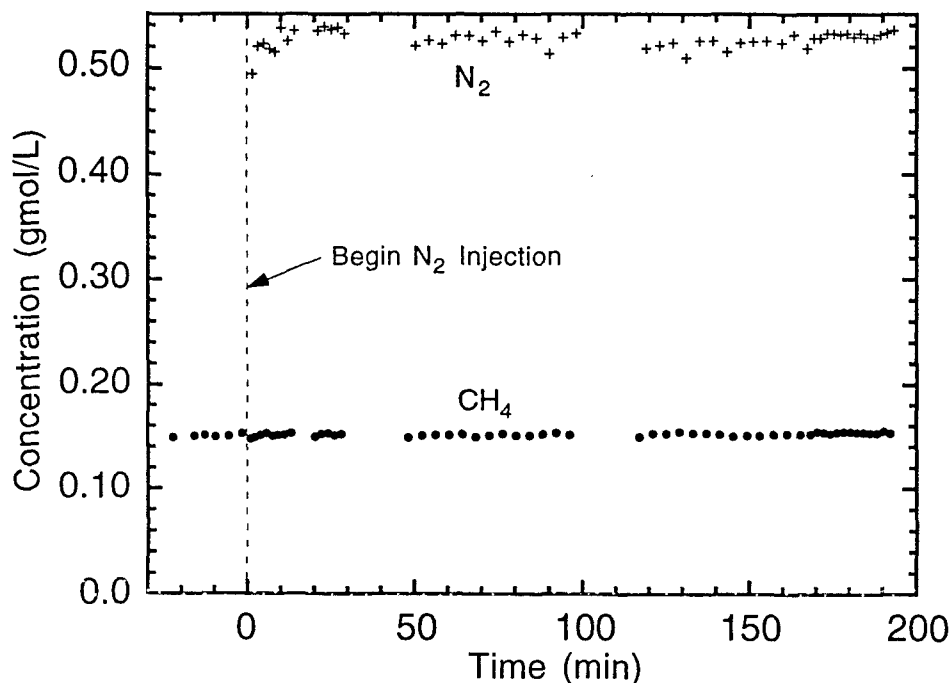


Figure 2.8.\* Nitrogen injected into a mixture of 0.15 gmol/L methane in water at 409 °C. Initial pressure = 241 bar, final pressure = 279 bar. Duration of injection = 22 s.

At lower pressures, the unheated volume of tubes and fittings attached to the reactor (*external volume*) affects the settling period. The major effect is a permanent loss of methane due to material being pushed out of the reactor

during injection. Figure 2.9 shows such a fuel deficit at  $P = 138$  bar: following injection, methane concentration never recovers to its original value. The fuel deficit problem is worse at lower pressures since fuel fraction increases as water density drops. Experiments were conducted at final pressures as low as 35 bar; the resulting data shows the same trends as Figure 2.9, with deficits of methane as high as 40% at the lowest pressure. Assessment of the magnitude of fuel deficits during oxidation experiments can be obtained from carbon balances (see Section 4.2.4).

The behavior of nitrogen concentration in Figure 2.9 suggests that there are in fact two settling time scales. The initial rapid drop of  $N_2$  in this experiment occurs at the same rate as the settling of  $CH_4$  concentration. But superimposed is a slower decline in  $N_2$  that persists throughout the experiment. Our hypothesis is that mass exchange occurs during the first few minutes with adjacent portions of the external volume (or even with crevice volume around the windows within the reactor). This is termed the settling period. The longer duration drift in injected gas concentrations is due to exchange with more distant portions of the external volume. This drift is not evident for methane since there is a much smaller concentration difference driving the exchange. (The fuel-water mixture has a long time to equilibrate at the start of the experiment.) The long time scale drift of  $N_2$  concentration is pronounced in Figure 2.9; typically the drift was less than shown here. The variation is due to varying amounts of condensed water in the tubing attached to the reactor. The liquid water affects the amount of external volume available, which in turn affects mass transport. Similar settling time experiments were conducted with oxygen (no fuel present) and carbon dioxide. These gases all had similar settling times, indicating dissolution in external condensed water is not a significant factor.

What is the impact of this settling time on the interpretation of kinetics experiment data? Calculated concentrations of methane could be artificially low and oxygen high during the settling period. At conditions that represent the main thrust of this work, i.e., at pressures near 270 bar, the impact on concentration histories is small. At these pressures, the first data point of each methane concentration history is accurate since no fuel is permanently lost to the external volume (i. e., no fuel deficit). The next 1 - 3 data points that follow could be low since they were recorded during the settling period. However, the 15 - 60 measurements made during the duration of the experiment should be accurate.

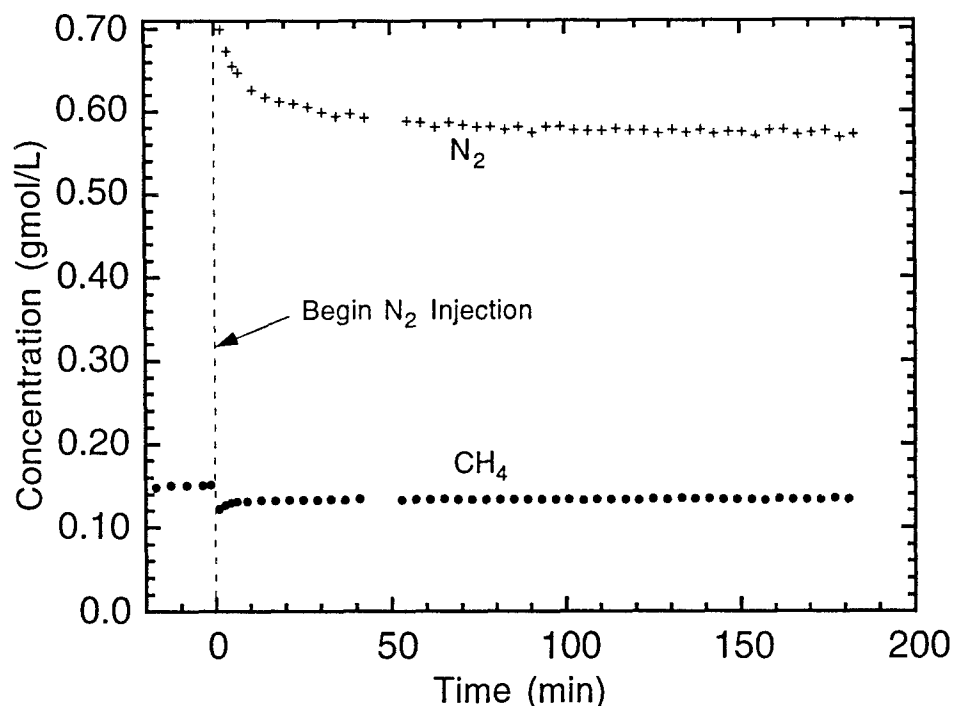


Figure 2.9. Nitrogen injected into a mixture of 0.15 gmol/L methane and water at 410 °C. Initial pressure = 101 bar, final pressure = 138 bar. Duration of injection = 63 s.

At pressures around 135 bar, the first methane concentration point is likely to be 10 - 20% high due to the fuel deficit that occurs at these conditions. The apparent initial oxygen concentration, taken as the first oxygen value following injection, will be incorrect as well, since oxygen will be lost by mass transport during the remainder of the experiment. To address the higher uncertainties of measurements made during the settling period, the first few data points of each experiment are discarded in the analyses performed in Chapter 4.

### 2.5.3. Isothermal Assumption

A constant temperature was assumed for each experiment in order to fit a global reaction rate expression to the kinetics data (see Sections 4.2.5 and 4.3.4). Actually, elevated temperatures were observed in the first few measurements following injection of the oxidizer. In the worst case 270-bar experiment, a value 11 °C above the mean was recorded one minute after injection; within 5 minutes, the temperature was stable at the value characterizing the remainder of the 3.5 hour experiment. Temperature fluctuations in the lower pressure experiments were greater due to the reduced water density, although recovery to a stable

temperature still occurred as rapidly. Thus, at all pressures, deviations from constant temperature occurred during the settling period causing an unknown, temporary increase in reaction rate. As described above, this problem was addressed in the global rate analyses by performing abridged fits in which settling time data was discarded.

In order to determine the spatial uniformity of temperature in the reactor, a second thermocouple was installed for several experiments. It was located in the bottom quarter of the reactor, while the original was situated a third of the way from the top. The second thermocouple consistently measured a 2.5 °C lower temperature.

#### **2.5.4. Isobaric Assumption**

For the flame experiments, the reactor was connected to a back-pressure regulator that was capable of holding pressure within 1 bar at 270 bar during steady injection of oxygen. However, the start of injection and the spontaneous ignition of flames were both unsteady processes that could cause 10-bar swings in pressure.

The kinetics experiments were conducted in a closed reactor, i.e., at constant volume rather than at constant pressure. Following oxidizer injection, pressure in the reactor declined steadily. The drop was typically 5 - 10 bar in the 270-bar experiments, and 2 - 5 bar for runs at 135 bar. For purposes of the global reaction rate analyses (see Sections 4.2.5 and 4.3.4), the variations of pressure were ignored since pressure is not an input parameter for those calculations. The cause of pressure variations is attributed to temperature fluctuations, non-ideal mixing of reactants and products in water, and deviations from the equimolar stoichiometric conversion of  $\text{CH}_4$  to  $\text{CO}_2$  and  $\text{H}_2\text{O}$  (See Section 4.2.4).





### 3. Hydrothermal Flame Experiments

#### 3.1. Introduction

The supercritical water oxidation process is normally designed to be flameless: wastes are destroyed through low-temperature oxidation reactions ( $< 650\text{ }^{\circ}\text{C}$ ) occurring in flow reactors with residence times on the order of 30 s. In contrast to these low-temperature reactions, it is possible to obtain stable, high-temperature diffusion flames in supercritical water-fuel mixtures as first demonstrated by Franck and coworkers (Schilling and Franck, 1988). Such flames occurring inadvertently in a reactor designed for low-temperature oxidation could upset process performance and threaten reactor integrity. Thus the study of these hydrothermal flames is important to the development of commercial SCWO processes. Further, it provides an opportunity to extend basic scientific understanding of diffusion flames by examining the effects of high density and an aqueous environment.

The literature on laminar diffusion flames at more conventional pressures is extensive (Burke and Schumann, 1928; Roper, 1977; Roper, *et al.*, 1977). Following the usual notation, a *normal* diffusion flame is created by injecting a jet of fuel into a co-flowing or quiescent background containing an oxidizer. *Inverse* diffusion flames (IDF) are those in which the primary jet is a flow of oxidizer, and the surroundings contain the fuel. In contrast with normal diffusion flames, the literature on inverse diffusion flames is limited (Sidebotham, 1988; Sidebotham and Glassman, 1992; Makel and Kennedy, 1994), due to the historical lack of practical applications. However, hazardous wastes often contain a mixture of oxidizable species (hydrocarbons) in water, and their treatment logically involves the injection of an oxidizer into the aqueous wastes, as in an inverse diffusion flame.

In *non-reacting* flows, the fluid mixing and material transport of normal and inverse jets are similar. The analysis of transport of momentum, thermal energy, and species between a nonreacting jet of fuel or oxidizer and the appropriate surroundings proceeds identically. Whether the inner jet is fuel or oxidizer is of no importance as long as the material identities of jet and surroundings (density, molecular weight, viscosity, etc.) are properly maintained in the analysis. When chemistry is added to the analysis, however, the resulting

flames differ substantially due to differing temperature and composition histories experienced by the reactants. In normal diffusion flames, the temperature of fuel molecules rises from inlet conditions to the flame temperature over a distance on the order of the flame height. This relatively gradual temperature gradient allows time for pyrolysis of fuel molecules to occur before they reach the flame. In inverse diffusion flames, however, the fuel molecules are outside the flame envelope and see a much narrower preheat region (higher temperature gradient) as they diffuse to the reaction zone. A well documented consequence of this difference is reduced soot formation (Sidebotham, 1988).

This chapter discusses a series of experiments undertaken to study inverse diffusion flames that spontaneously ignite when oxygen is injected into supercritical mixtures of water and methane or methanol. Inverse rather than normal diffusion flames were chosen since SCWO processes are often designed to inject an oxidizer stream into supercritical water-waste mixtures. Methane, being a relatively difficult compound to oxidize, was chosen to provide a conservative measure of flame ignition in supercritical water. Both methane and methanol offer the advantage of being well studied, with published elementary reaction mechanisms available for elevated pressures (Webley and Tester, 1989; Webley and Tester, 1991; Holgate, 1993). The goal of these tests is to provide a qualitative description of the structure of the hydrothermal flames and to quantify their spontaneous ignition limits.

## **3.2. Flame Phenomenology**

### **3.2.1 Experimental Procedure**

Aside from the difficulties of sealing our reactor at high-pressure, producing a hydrothermal flame is relatively simple. To prepare for a flame experiment, a mixture of fuel and water is loaded as described in Section 2.3.1. Normally, the mixture is given about 10 minutes to stabilize, with Raman measurements used to monitor the process. Over our experimental range, 390 - 510 °C, methane pyrolysis is not detectable; however, perceptible reaction of methanol in water occurs above 470 °C, requiring an accelerated procedure in those experiments.

Once the fuel-water mixture is homogeneous and initial concentrations have been recorded, injection of oxygen begins. While the back-pressure

regulator holds pressure constant, the HPLC pump pushes oxygen into the reactor at 0.5 - 1.0 mL/min. Given sufficient fuel and high enough temperature, a diffusion flame ignites spontaneously. The visible and shadowgraph images of the flame are recorded on video tape while internal temperature and pressure are tracked by computer. Flame size and duration can be controlled by oxygen injection rate, with flames typically lasting several minutes. Cutting off oxygen flow of course terminates the flame immediately; alternatively, continuing the oxygen flow eventually leads to extinction of the flame due to fuel depletion.

Figure 3.1 shows the temperature and pressure history of a typical hydrothermal flame that is allowed to burn until extinction. Since the thermocouple is located above the oxygen injector, the temperature trace clearly indicates ignition and extinction. During burning, the video tape captures the visible image of the flame, as well as a shadowgraph image revealing the buoyant plume associated with the flame. As described in the next section, this plume serves as an indicator, along with the temperature trace, of flames that are otherwise invisible.

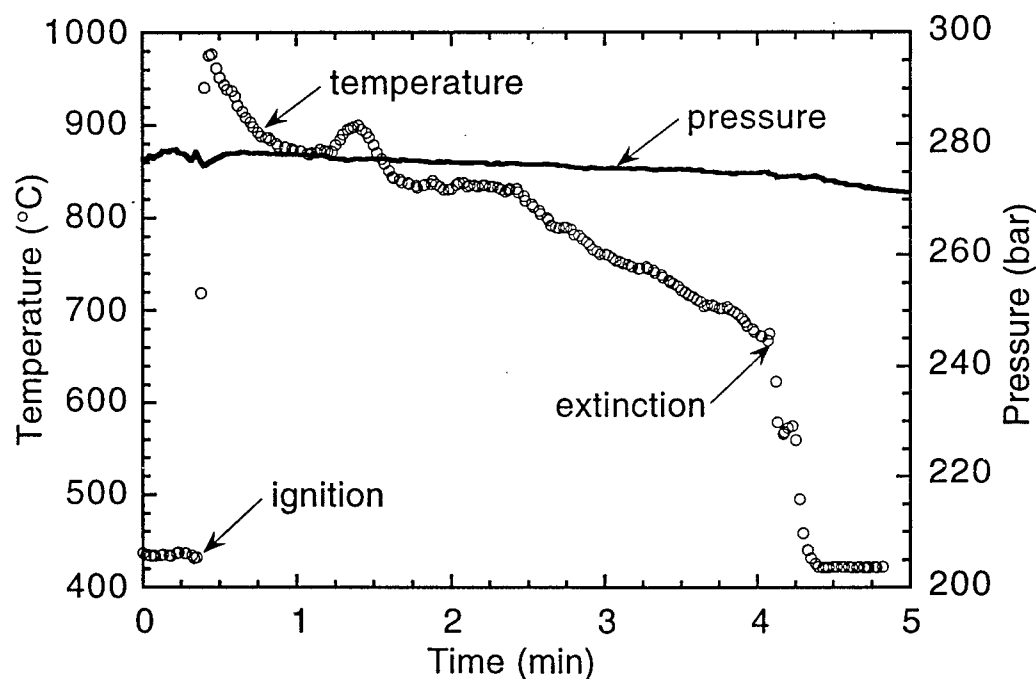


Figure 3.1. Temperature and pressure histories of a hydrothermal diffusion flame that spontaneously ignited upon injection of oxygen into a mixture of water and 12 mole% methane.

### 3.2.2. Flame Description

Figure 3.2 presents a sequence of photographs of a typical methane hydrothermal flame during its lifetime. The photographs combine both visual and shadowgraph images. Figure 3.2-a is representative of the flame early in its lifetime. Fuel concentration in this example is high ( $\sim 20$  mole%), and under such conditions, the flames appear white and intensely luminous. The slender, stable flames have diameters of about 1 mm and heights that are controlled by oxygen injection rate. The dark structure around and above the flame in Figure 3.2-a is a shadowgraph image of the buoyant plume of lower density fluid created by the flame. The dark object intercepting the plume at the top is the 1.6-mm sheathed thermocouple. The circular field of view in this photograph is defined by the 7.6-mm aperture of the sapphire windows; the actual ID of the reaction cell is about three times larger.

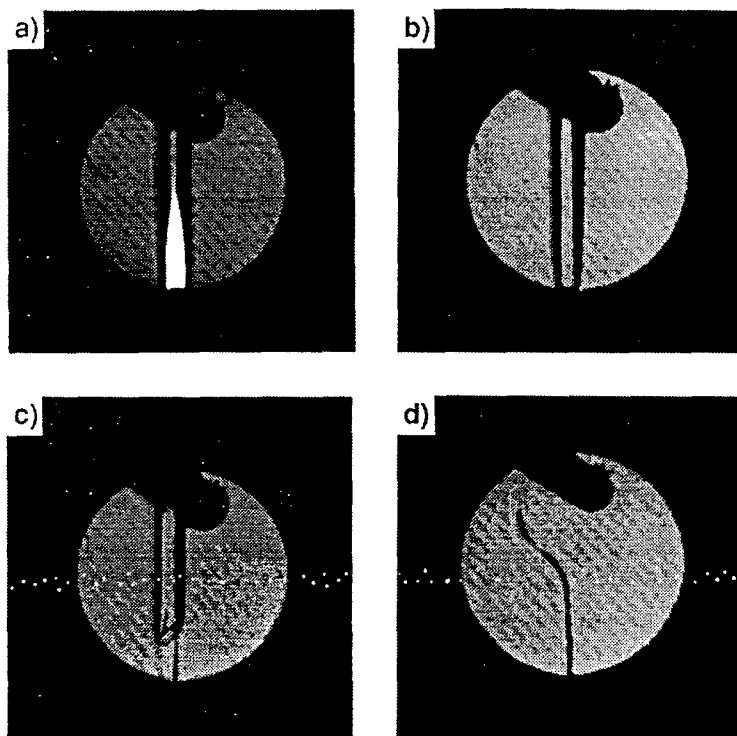


Figure 3.2. (a) Photograph of a typical luminous hydrothermal flame at high fuel concentration. (b) The same flame, but at lower fuel concentration. (c) The same flame at the moment the flame lifts off. (d) Nonreacting oxygen jet following flame extinction.

In a typical experiment, fuel is added prior to oxygen injection, and it is gradually consumed during flame combustion. Depending on initial fuel concentration and oxygen injection rate, the flames can burn for more than twenty minutes. Since chemical and transport time scales are short compared to that of fuel depletion, fuel concentration can be treated as quasi-steady. The exit port of the reactor is located directly above the oxygen injector and a steady fluid flow leaves via this port and the back-pressure regulator. Because of the orientation, a large portion of the exit flow is combustion products, but certainly some fuel leaves by this route as well. In addition, combustion products build up in the reactor as corroborated by post-flame Raman measurements. Velocity measurements were not performed in the reactor, but recirculation flow is assumed to develop in the initially quiescent water-fuel mixture.

As fuel is consumed during an experiment, flame luminosity continuously decreases, and eventually becomes invisible to the unaided eye. At this stage, shown in Figure 3.2-b, the continuing exothermic reaction is revealed by both the dark thermal plume in the shadowgraph and the continuing elevated temperatures recorded by the thermocouple probe. This stage of the combustion can continue for several minutes. When fuel concentration drops below a certain limit, the plume structure lifts off the injector as seen in Figure 3.2-c and rises out of view in less than a second. All evidence of the combustion reaction disappears—the thermocouple readings drop to the ambient temperature (which typically has risen less than 15 °C), and the shadowgraph no longer shows a buoyant plume. The oxygen jet is still visible in the shadowgraph (Figure 3.2-d), but is distinguished by a wavering that indicates a cooler stream (no longer heated by reaction) injected into the hotter supercritical water mixture.

In an effort to compare the behavior of high-pressure flames to more conventional flames, several experiments were performed at intermediate pressures. Attempts at spontaneously igniting flames at pressures near 100 bar ended with too-rapid reaction and a ruptured burst disk. To avoid this, flames were first ignited at 275 bar, and then pressure was gradually lowered using the back-pressure regulator. As reactor pressure fell, the oxygen injector valve was adjusted to hold flame height constant. Loss of fuel due to depressurization was compensated for by periodically adding fuel as needed to keep the flame visible. In this way, a flame ignited at supercritical pressures was kept burning down to pressures as low as 15 bar. The difficulties associated with this procedure precluded any quantitative comparisons with high-pressure flames. Changes in

appearance, however were obvious. As pressure dropped, the flames broadened distinctly. The long slender form of the high-pressure flames was gradually replaced with a much more circular shape at low pressure.

Several flames were also ignited in a mixture of fuel plus argon in place of water. Due to reactor limitations, these experiments were performed at the same 270-bar maximum pressure. This means number densities in the argon experiments were half that of the water experiments, due to differences in compressibilities. Despite these differences, the argon flames behaved the same as the hydrothermal flames in visual tests.

### 3.2.3. Flame Temperature

Temperatures of the hottest flames created were beyond the measurement range of the thermocouple probe (1000 °C). Calculations using the chemical equilibrium code STANJAN (Reynolds, 1986) with the high-pressure code, Chemkin Real-Gas (Schmitt, *et al.*, 1993) yield an adiabatic flame temperature of 2920 °C for a stoichiometric amount of oxygen added to 30 mole% methane in water initially at 500 °C and 270 bar. Schilling and Franck (1988) used OH-radical chemiluminescence to make a tentative flame

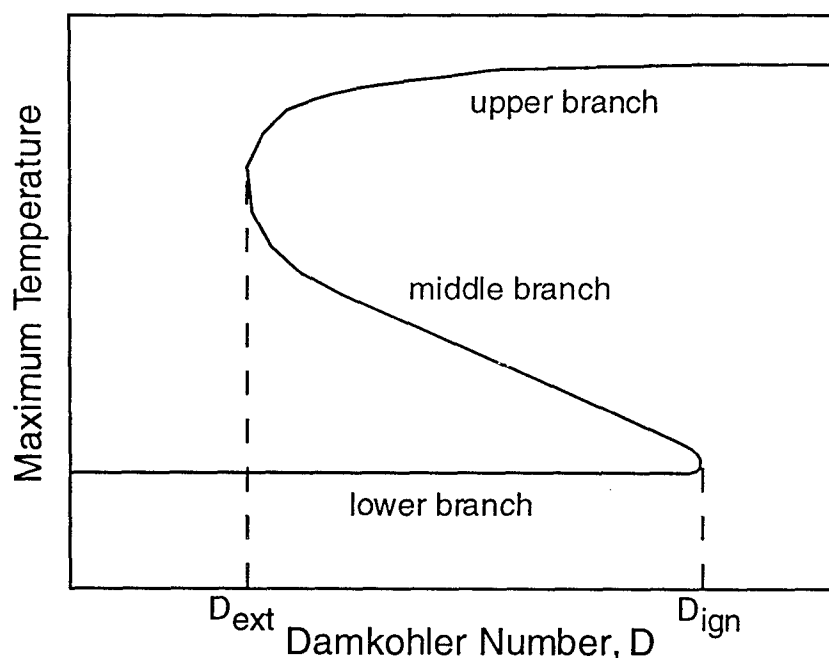


Figure 3.3. Diagram of the dependence of maximum temperature on Damköhler number for diffusion flames (Williams, 1985).

temperature measurement of 3130 °C for a 30 mole% methane-water-oxygen flame at 700 bar.

In our experiment, the thermocouple probe was located in the hot plume just above the flame, so that it tracked trends in flame temperature below 1000 °C. Observed temperatures decreased steadily with visible flame luminosity, even while flame height stayed constant; temperatures were recorded as low as 50 °C above ambient temperature at the time of flame extinction. These large variations in flame temperature and luminosity suggest a wider range in flame burning intensity than is observed for atmospheric methane flames. The familiar S-shaped Damköhler curve in Figure 3.3 describes the limited range of burning temperatures observed for diffusion flames at atmospheric pressure. Relatively minor decreases in flame temperature on the upper branch lead to extinction under those conditions. In contrast, our experiments in supercritical water indicate a continuous, extended range of possible flame temperatures.

A Raman spectroscopy method for measuring temperatures developed in the SCW reaction cell (Brown and Steeper, 1991) was tested on the hydrothermal flames. The method uses the Raman spectrum of CO<sub>2</sub> which, in our temperature range, exhibits several hot bands distinct from the fundamental vibrational feature, as shown in Figure 3.4. By integrating these peaks separately and taking their ratio, a calibration-free measurement of temperature is obtained. During development, the technique was successfully applied to homogeneous mixtures of carbon dioxide and supercritical water; the experiment described below was an attempt to make similar measurements in the presence of a hydrothermal flame.

During the experiment, the reactor was translated 6 mm along the laser axis to provide spatial Raman measurements in and around the ~1-mm diameter flame. Raman measurements of methane concentration were made prior to oxygen injection, and values were constant within  $\pm 3\%$  along the traverse. A flame was ignited as in earlier experiments and allowed to burn until its luminosity was low; Raman CO<sub>2</sub> spectra were then recorded at several locations. Figure 3.4 is a typical CO<sub>2</sub> spectrum recorded to one side of the flame. Broadband emission from the flame is visible as an elevated baseline, but the fundamental transition and two hot bands are evident and can be used to calculate temperature. Using the correlation established in Brown and Steeper (1991), temperatures from 390 to 460 °C were obtained for the six measurements

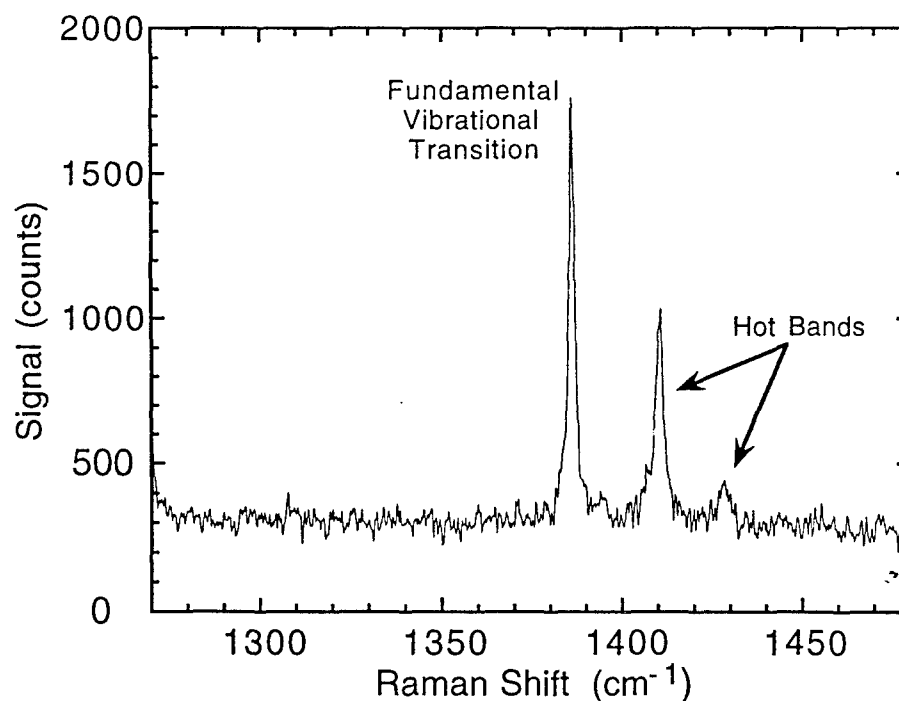


Figure 3.4. Raman spectrum of symmetric stretch of CO<sub>2</sub> in supercritical water. The measurement was made 2 mm to one side of a dim hydrothermal flame. Pressure = 276 bar; bulk temperature = 435 °C; plume temperature = 790 °C.

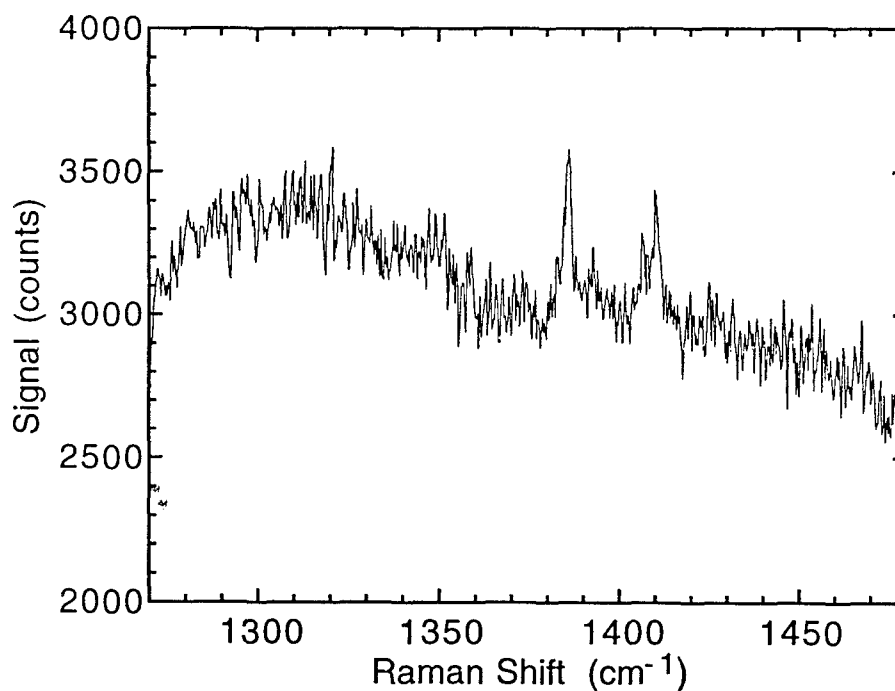


Figure 3.5. Raman spectrum of CO<sub>2</sub> recorded in the same experiment as Figure 3.4 but centered in the flame.



made outside of the flame. This range of temperatures agrees with the bulk fluid (thermocouple) temperature of 435 °C within the uncertainty reported for the optical technique (Brown and Steeper, 1991).

On the other hand, spectra recorded in the flame are not as easily interpreted, as illustrated in Figure 3.5. Beam steering by the flame reduced the carbon dioxide signal, and flame emission created a curved baseline. The resulting deterioration of signal-to-noise ratio made in-flame temperature measurement impossible, even in relatively dim flames. As a result of this test, further efforts to apply the Raman temperature diagnostic to hydrothermal flames were abandoned.

### 3.2.4. Flame Aspect Ratio

As fuel is consumed during an experiment, flame luminosity and plume temperature decrease continuously. Despite these significant changes, observed flame height and diameter do not change noticeably if the oxygen flow rate is held constant. This observation agrees with the simplified Burke-Schumann analysis of axisymmetric diffusion flames that predicts a height proportional to  $Q/D$ , where  $Q$  is the volumetric flow rate and  $D$  is an appropriate diffusion coefficient (Burke and Schumann, 1928). A more complete treatment, however, must include the effects of buoyancy and dilution (Roper, 1977). Sidebotham (1988) developed such an expression based on ideal-gas assumptions and valid for both normal and inverse diffusion flames:

$$H \sim \frac{1}{2\pi D_0} \left( T_0/T_f \right)^{0.67} (1+S) Q_t \quad 3.1$$

where  $H$  is the flame height,  $D_0$  is the fuel diffusivity at ambient conditions,  $T_0$  is the ambient temperature,  $T_f$  is an effective flame temperature, and  $Q_t$  is the volumetric flow rate of oxidizer (in the case of an IDF) plus any diluent. The parameter  $S$  includes the dilution effect:

$$S = \frac{X_{ox}}{(I')X_f} \quad (\text{for an IDF}) \quad 3.2$$

where  $X_{ox}$  and  $X_f$  are mole fractions of oxygen and fuel in their respective streams, and  $I'$  is the molar stoichiometric ratio of oxygen to fuel. The above expression for  $H$  predicts that diminishing fuel concentration and the associated drop in flame temperature should cause an increase in flame height. The

prediction disagrees with the observed insensitivity of flame height to fuel concentration.

We have considered several possible explanations for the disagreement between our observations and the above expression for flame height. First, as Sidebotham's experimental results for inverse diffusion flames indicate (Sidebotham, 1988), the sensitivity of flame height to dilution is less important at lower dilutions, i.e., at higher fuel concentrations. Thus, during the period that our flames are most visible (fuel concentrations above 20 mole%), changes in flame height due to consumption of fuel are less pronounced. Calculating the effect of a typical change in  $X_f$  on  $1+S$  (and therefore on flame height) using Equation 3.1, however, indicates that flame growth should be detectable. For example, as the fuel fraction drops from 0.4 to 0.2 for a methane flame,  $1+S$  increases by 50%; this should translate into a similar increase in flame height. The associated drop in flame temperature should increase flame height further.

Another consideration is that our conditions represent a large extrapolation from those used to generate Equation 3.1. As an example, diffusion coefficients at our experimental conditions are two orders of magnitude smaller than those for atmospheric flames (Reid, *et al.*, 1987). Additionally, suggested correlations (Lamb, *et al.*, 1981) for diffusion coefficients at supercritical densities show a different (i.e., Arrhenius) dependence on temperature than is used to derive Equation 3.1 ( $D \sim T^{1.67}$ ). Models that employ Arrhenius-type diffusion coefficients predict significant changes in flame structure (Bechtold and Margolis, 1992).

A final consideration in the contrast between predictions and our experimental results is the question of buoyancy-controlled flame heights. Buoyancy is included in the derivation of Equation 3.1, but, as first pointed out by Roper (1977), the effects of buoyancy on flame height theoretically cancel in an axisymmetric geometry. Along with an increase in velocity due to buoyancy, there is a simultaneous reduction in flame diameter which means a shorter diffusion time. While one factor tends to increase flame height, the other decreases it. In practice, though, the cancellation is not exact (Roper, 1977).

To measure the relative importance of buoyancy in our experiment, the Froude number can be examined:

$$Fr = v^2/dg \quad 3.3$$

where  $v$  is the oxygen jet inlet velocity,  $d$  is the flame base diameter, and  $g$  is the acceleration of gravity. If  $Fr$  is much smaller than a normalized density difference (between the jet at flame temperature and the bulk supercritical water), then the flame height is likely to be buoyancy controlled (Williams, 1985). Table 3.1 presents buoyancy calculations at a reactor temperature of 400 °C and at two different oxygen delivery rates. For the low flow rate case, the normalized density difference is about 3 times larger than the Froude number, and buoyancy indeed may dominate the flame geometry. However, using the more typical oxygen delivery rate of 1.0 mL/min, the calculation indicates that buoyancy does not dominate. For experiments at higher reactor temperatures or with lower average flame temperatures, the density difference shrinks with respect to the Froude number.

This analysis neglects fluid recirculation that likely occurs in the reactor during the flame experiments. The driving force for such recirculation comes from the jet's momentum, resulting in a lower jet velocity. It is possible that the Froude number is thereby reduced enough to create buoyancy-controlled conditions in more experiments than implied by the arguments of the last paragraph. The final conclusion is that buoyancy may indeed mask predicted flame height trends in some, but probably not all of our experiments.

Quantity	Symbol	1.0 mL/min O <sub>2</sub> delivery	0.5 mL/min O <sub>2</sub> delivery
jet inlet velocity	$v$	19. cm/s	9.5 m/s
flame base diameter	$d$	0.1 cm	0.1 cm
mean flame density @ 2000 °C	$\bar{\rho}$	0.053 g/cm <sup>3</sup>	0.053 g/cm <sup>3</sup>
water density @ 400 °C	$\rho_w$	0.22 g/cm <sup>3</sup>	0.22 g/cm <sup>3</sup>
density difference	$\Delta\rho$	0.17 g/cm <sup>3</sup>	0.17 g/cm <sup>3</sup>
normalized density difference	$(\Delta\rho)/\bar{\rho}$	3.2	3.2
Froude number	$Fr$	3.7	0.92

**Table 3.1.** Froude number calculations for hydrothermal flames at  $P = 275$  bar. A flame temperature of 2000 °C is used as a conservative (high) estimate.

### 3.2.5. Flame Emission Spectra

At high methane and methanol concentrations, the hydrothermal flames burn with intense luminosity that appears bluish white. At lower fuel concentrations, the flames are less intense and appear more red-yellow. To characterize the emission from hydrothermal flames as it evolves during an experiment, the light was analyzed with a low-dispersion spectrograph.

Figure 3.6-a is a sample raw flame emission spectrum. To interpret the spectrum, two corrections must be applied: a second-order dispersion correction and a detector response correction. First-order peaks appearing at short wavelengths reappear in second-order dispersion at double the wavelength and at reduced intensity. The ratio of first- and second-order intensities was determined using an Ar laser line, permitting correction for second-order contributions. A correction curve for detector response as a function of wavelength was determined using a tungsten calibration lamp. Figure 3.6-b is a graph of the resulting intensity correction factor.

Figure 3.7 presents 6 corrected spectra taken from one methane-oxygen flame over a period of ten minutes, as the flame evolved through the stages presented earlier in Figure 3.2. The sequence in Figure 3.7 illustrates several characteristics representative of all the emission experiments conducted. One obvious characterization is that the white emission of the early, hot flame is not simple blackbody radiation. Figure 3.7-a indicates that over most of the visible range (400 - 700 nm), the emission intensity is flat, with broad peaks appearing at both ends of this range. The strong peak at 400 nm is responsible for the bluish tint of the early flame, but has not been identified. Franck's team has reported (Schilling and Franck, 1988) a peak appearing in a hydrothermal flame emission spectrum between 300 and 330 nm attributed to OH radicals. This feature was not detected in our experiments due to bandpass limits of our optics.

There is a characteristic evolution of the emission spectra during a flame's lifetime represented in Figure 3.7-a through f. The 400-nm peak steadily diminishes and disappears as several near-IR features grow. There is an associated small increase in visible light above 600 nm that explains the reddish cast late in the flame's lifetime. A small peak appearing at 590 nm is likely due to sodium contamination. An experiment at lower pressure (70 bar), and an experiment in which argon was substituted for water both produced spectra with the same characteristic features and evolution.

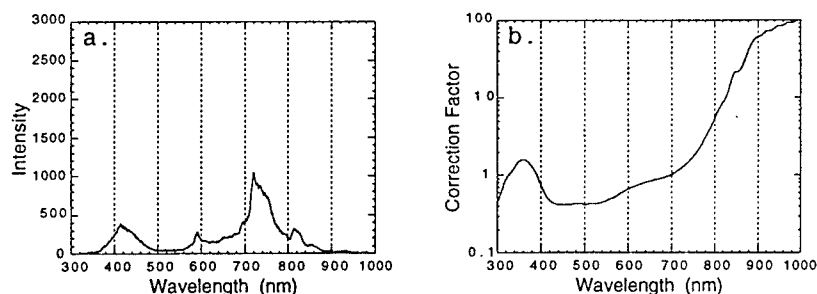


Figure 3.6. (a) Uncorrected methane-oxygen hydrothermal flame emission spectrum. (Shown corrected in Figure 3.7-d.) (b) Correction factor for diode array detector on J-Y spectrograph.

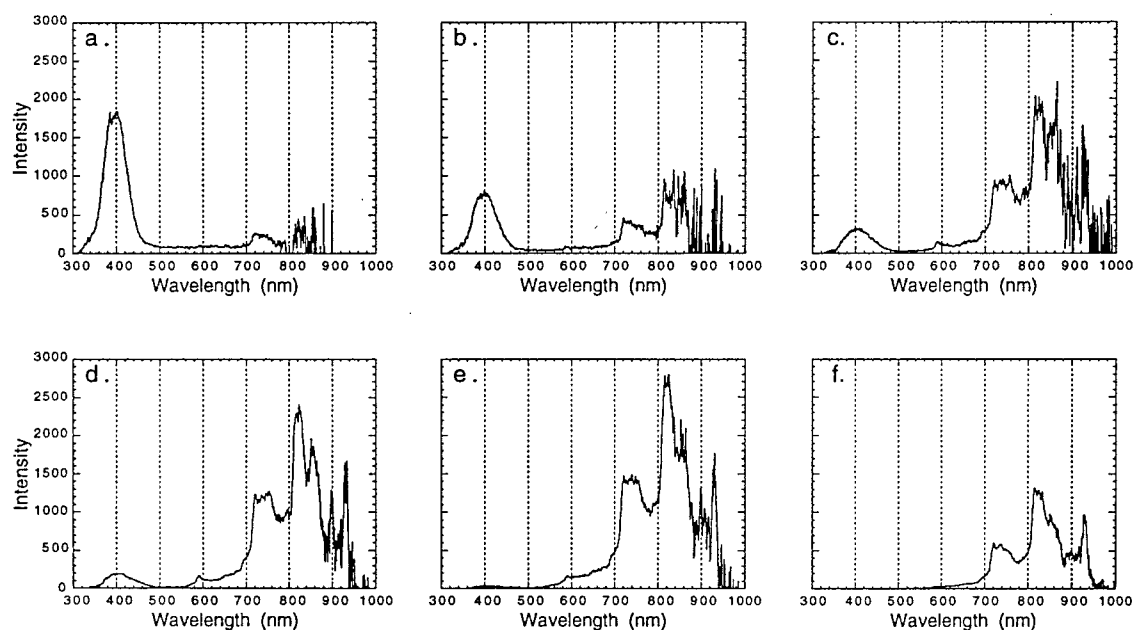


Figure 3.7. Series of corrected flame emission spectra taken during the lifetime of a methane-oxygen hydrothermal flame at 278 bar. Intensities are normalized to account for varying exposure times from 0.033 to 0.33 s. (a) Flame time = 2 min, bright flame. (b) Time = 3 min. (c) Time = 5 min, dim flame. (d) Time = 6 min, flame barely visible. (e) Time = 8 min, flame no longer visible. (f) Time = 10 min; extinction occurs at time = 12 min.

### **3.3. Spontaneous Ignition Limits**

#### **3.3.1. Experimental Procedure**

In order to better understand the spontaneous ignition of hydrothermal flames, a series of experiments was performed to map the minimum fuel concentrations and temperatures required for auto ignition of methane and methanol flames in the HFR. Five parameters affecting the ignition of these flames were controlled: choice of fuel and oxidizer, concentration of fuel and oxidizer, pressure, temperature, and oxidizer injection rate. The chosen fuels were methane and methanol with pure oxygen as the oxidizer. Pressure was set at a value of approximately 275 bar for each experiment and a temperature between 380 and 510 °C was chosen.

The experiment consisted of loading and testing decreasing fuel concentrations to find the minimum ignitable concentration. While testing for auto ignition in a given fuel-water mixture, the oxygen delivery rate was adjusted in the range of 0.5 to 1.0 mL/min (at reactor pressure and room temperature). Ignition was indicated by an abrupt and sustained temperature rise accompanied by the appearance of a buoyant plume structure in the shadowgraph video.

The main source of error in the concentration measurements originates from irreproducibilities in the Raman scattering integrated intensities. Fluctuations in the laser beam image dimensions within the HFR due to thermal lensing resulted in a concentration measurement error of  $\pm 6\%$ . This value is estimated from the magnitude of fluctuations in repeated Raman measurements made in water at fixed fuel density. The equation of state method used to convert concentrations to mole fractions (see Section 2.4) introduces only a small additional error since the species being measured in most cases constitute only a small fraction of the mixture. An exception is the low temperature methanol results (see next section) for which the minimum fuel fraction for auto ignition is about 35 mole%. The resulting accuracy in reported minimum ignition concentrations remains  $\pm 6\%$  (95% confidence) for all but the methanol data below 400 °C.

#### **3.3.2. Experimental Results**

Over seventy ignition trials were performed to map the minimum fuel fractions required for spontaneous ignition of methane and methanol flames as a

function of reactor temperature. The ignition experiments are listed in Section 7.2 and presented graphically in Figure 3.8 (methane) and Figure 3.9 (methanol). In the figures, solid symbols represent experiments in which flames spontaneously ignited. The interpolated dashed lines on the graphs indicate the lowest fuel concentrations at which hydrothermal flames ignited. At conditions below these lines, flames did not ignite, although fluid agitation was observed in the shadowgraphs during some of these experiments—caused by abortive reactions not leading to ignition. Note that there are a few non-ignition points above the dashed lines—these data indicate that ignition is sensitive to variation in oxygen injection rates. As a final clarification, note that the methanol data at 510 °C are incomplete. Difficulties caused by pyrolysis made it impossible to complete experiments at the lowest fuel concentrations. Raman measurements made at temperatures above 470 °C showed that the concentration of methanol in water dropped significantly in the few minutes prior to oxygen injection. Simultaneously, concentrations of CH<sub>4</sub>, CO<sub>2</sub>, CO, and H<sub>2</sub> appeared. STANJAN/Chemkin Real-Gas (Reynolds, 1986; Schmitt, *et al.*, 1993) equilibrium calculations confirm that a mixture of methanol and water is driven toward the products detected. Because of these difficulties, the interpolated line in Figure 3.9 is stopped short of the data at this temperature.

Following each ignition test, Raman measurements revealed the combustion products and any remaining reactants. For both methane and methanol, significant amounts of CO<sub>2</sub> were formed whether a flame ignited or not. When flames were allowed to proceed to extinction (i.e., injection of oxygen was halted at extinction), residual fuel concentrations measured from 1 to 5 mole% depending on temperature. Following methanol flames, we detected measurable quantities of CO and H<sub>2</sub>. Additionally, methane was detected following methanol experiments in which flames never ignited. Some chemical reaction models of methanol oxidation in supercritical water (Webley and Tester, 1989) predict formation of formaldehyde in small amounts; no formaldehyde was detected following our flame experiments, although it was detected during the kinetics experiments reported in the next chapter.

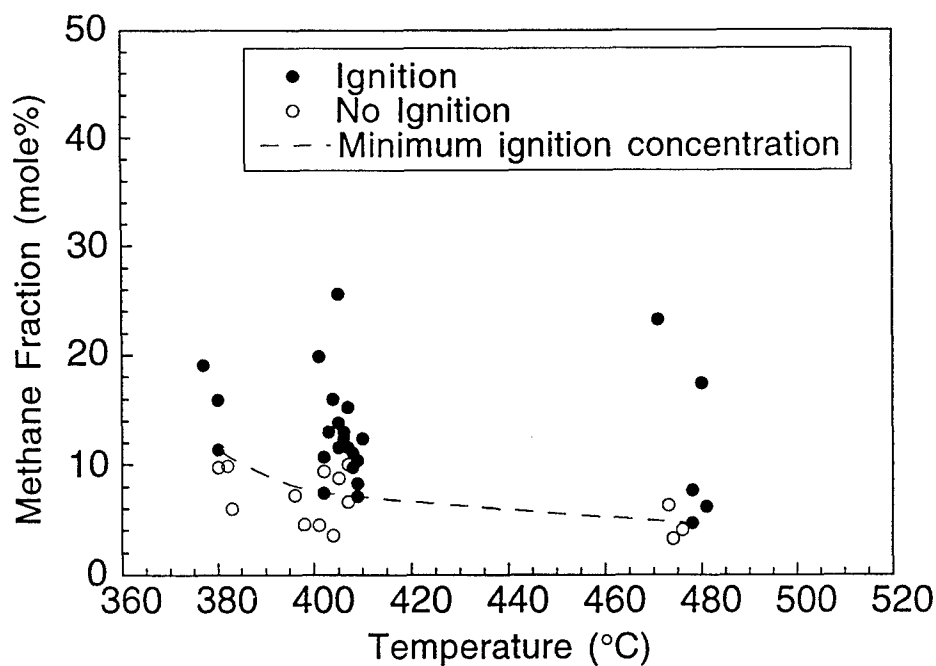


Figure 3.8. Limits of the spontaneous ignition of methane in supercritical water upon injection of pure oxygen. Pressure is  $275 \pm 5$  bar and oxygen injection rate at reactor conditions is 1 - 3 mL/min.

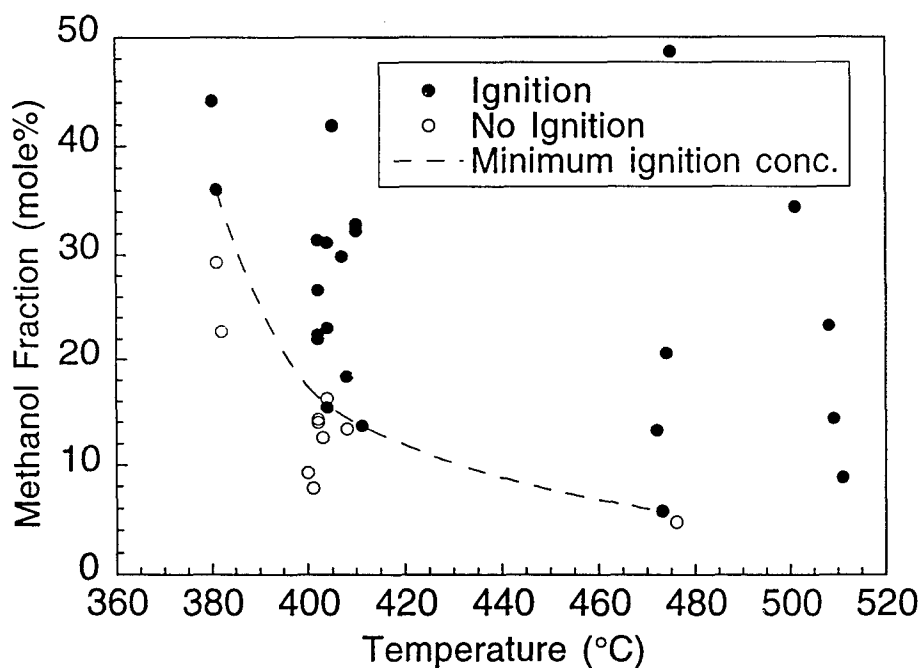


Figure 3.9. Limits of the spontaneous ignition of methanol in supercritical water upon injection of pure oxygen under similar conditions as Figure 3.8.



### 3.3.3. Conclusions

Diffusion flames spontaneously ignite and burn steadily in mixtures of supercritical water and methane or methanol. The intensity of these flames measured both by visible emission and temperature varies widely with fuel concentration. Flame aspect ratios are little affected by decreasing fuel concentration.

The flame ignition trials indicate that, at temperatures above 470 °C, diffusion flames readily ignite in supercritical mixtures with only 6 mole% methane or methanol in water. At these temperatures, the flames ignite immediately upon injection of oxygen (i.e., hypergolic ignition), even in the case where fuel concentration is so low that the ignited flame produces no visible light. In such cases, flame presence is confirmed by thermometric and shadowgraphic evidence. Since this range of fuel concentration, temperature, and pressure is typical of operating conditions in SCWO reactors, designers and operators must be aware of the possibility of flame formation. The data suggest that reactors in which an oxygen stream is injected into a supercritical mixture of fuel and water are susceptible to flame auto ignition—an event that could upset reactor performance and even threaten reactor integrity.

At lower temperatures, the data indicate that methanol is more difficult to ignite than methane, a trend indicated also in the global kinetics studies of Webley and Tester (1989, 1991). At the highest temperatures, pyrolysis of methanol made ignition studies difficult.



## 4. Methane Kinetics Experiments

### 4.1. Introduction

The development of supercritical water oxidation technology depends on understanding the reaction kinetics of a wide variety of compounds at SCWO conditions. Predictive chemistry models, as they become available, will play an important role in finding answers to design problems including: (1) predicting reaction rate dependency on temperature, pressure, and species concentrations; (2) calculating heat release rates and temperature histories during reaction; (3) predicting reaction completeness and byproduct profiles; (4) estimating catalysis effects; and (5) scaling laboratory- and bench-scale experimental results to commercial scale reactors. A long-term goal of SCWO kinetics research is establishing detailed elementary mechanisms for the oxidation of rate-limiting compounds such as carbon monoxide and methane. For the nearer term, simplified global reaction expressions are needed as engineering tools for the current design of commercial SCWO processes. The pursuit of these goals requires experimental measurements of the destruction rates of principal components, as well as production and consumption rates of key intermediates.

This chapter describes methane oxidation experiments designed to complement previously published studies. By conducting batch experiments in our optically accessible reaction cell, some limitations of earlier experiments were overcome. One such limitation has been low initial fuel concentrations. A common experiment design uses saturators to prepare initial oxidizer and fuel solutions. In this technique, the gaseous oxidizer or fuel is pressurized over room-temperature water for sufficient time to create an equilibrium aqueous solution. Advantages of this technique include accurate determination of fuel and oxidizer feed stream concentrations. An associated disadvantage is that concentrations are limited by room-temperature solubility behavior. Even for water-soluble fuels, low fuel concentrations are dictated by the limitations on available oxygen concentrations.

In the current study, a gaseous oxidizer is injected directly into the supercritical water-fuel mixtures, removing the restriction on reactant concentrations. As a result, fuel concentrations representative of commercial SCWO processes,

on the order of 1 gmol/L, are possible. Of course, higher fuel concentrations mean greater heat release, making isothermal operation more difficult.

The use of an *in situ* optical diagnostic for concentration measurements in the current study offers several advantages. The data rate is high: each experiment produces an entire concentration-versus-residence-time history rather than a single concentration value produced by other techniques. In addition, the method avoids potential problems associated with extracting, quenching, and analyzing samples off line. Finally, the *in situ* technique permits the measurement of some intermediate species that may not be measurable in a sample-and-analyze procedure.

Optical methods have been previously applied in supercritical water environments. Franck *et al.* made tentative temperature measurements based on hydrothermal flame chemiluminescence in their optical cell (Schilling and Franck, 1988). Raman spectroscopy has been used at the University of Delaware to measure concentrations of aqueous solutions at supercritical conditions (Spohn and Brill, 1989). At Sandia, measurements of both concentrations and temperatures have been made using Raman spectroscopy (Brown and Steeper, 1991; Steeper, *et al.*, 1992a; Steeper, *et al.*, 1992b; Steeper and Rice, 1994). At Los Alamos Raman spectroscopy was used in an optically accessible flow reactor to follow the decomposition of hydrazine in supercritical water (Masten, *et al.*, 1993).

Methane was the chosen fuel for our kinetics experiments. It is a well-studied, simple organic that serves as a model compound both because it is relatively difficult to destroy, and because its reaction mechanism includes pathways shared by many complex organics. The following sections describe experiments that were conducted in supercritical water at pressures around 270 bar, experiments in subcritical water (pressures as low as 35 bar), and experiments in which argon was substituted for water. The latter two types of experiments were included to clarify the role of water density on reaction rates in supercritical water.

## **4.2. Kinetics Measurements In Supercritical Water**

### **4.2.1. Experimental Conditions**

Table 4.1 lists the 15 methane kinetics experiments performed at a nominal pressure of 270 bar. The temperature range of these experiments, 390 - 442 °C, was limited by mixture critical temperatures at the lower end. Below its critical temperature, a mixture can support multiple phases, a condition that makes

interpretation of rate measurements intractable. Critical curves of many mixtures of common combustion gases and water have been experimentally measured, some of which are reproduced in Figure 4.1. The critical curves for nitrogen, carbon dioxide, oxygen, methane, and hydrogen at pressures up to a kilobar or more do not exceed water's critical temperature of 374 °C. This means that binary mixtures of any of these molecules with water at temperatures above 390 °C (our minimum experimental temperature) are guaranteed to be single phase. Experiments examining ternary and quaternary mixtures, and the predictions of phase equilibria models (Heilig and Franck, 1990), indicate that multiple component mixtures of these compounds in water are single phase above 390 °C as well. For our kinetics experiments, single phase operation is assumed, and our shadowgraph observations support this assumption.

The upper temperature limit of the experiments was dictated by the need for reaction time to be long in comparison with settling time (see Section 2.5.2). In experiments conducted at 442 °C, 95% of the initial methane was destroyed in

Exper. #	Avg. Temp (°C)	Avg. Press (bar)	Temp. Range (°C)	Press. Range (bar)	Initial [O <sub>2</sub> ] (gmol/L)	Initial [CH <sub>4</sub> ] (gmol/L)	Initial Equiv. Ratio	Run Time (min)	# of CH <sub>4</sub> Points
06284	403	270	403-404	267-277	0.30	0.171	1.14	360	47
06294	403	273	402-404	271-277	0.44	0.151	0.69	200	60
07014	419	267	419-420	266-276	0.38	0.131	0.69	150	50
07084	421	266	421-424	265-276	0.34	0.141	0.83	150	45
07124	397	276	395-397	275-282	0.41	0.117	0.57	200	56
07214	391	268	388-392	265-276	0.38	0.187	0.99	180	46
07224	392	276	390-392	273-283	0.40	0.153	0.77	230	59
07294	442	268	441-448	269-276	0.35	0.171	0.98	45	17
08024	442	268	442-452	269-279	0.36	0.175	0.97	40	17
08044	402	270	401-403	269-279	0.40	0.163	0.82	130	35
08244	412	268	412-415	267-278	0.31	0.165	1.06	75	17
08254	411	266	411-412	265-276	0.31	0.172	1.11	80	18
08264	410	271	410-411	271-277	0.42	0.113	0.54	90	28
08314	412	265	411-419	265-279	0.39	0.176	0.90	60	15
09014	413	265	412-418	265-277	0.38	0.146	0.77	170	42

Table 4.1. Summary of 270-bar methane kinetics experiments in supercritical water.

about 13 minutes; settling time was less than 3 minutes at this temperature. As a result, no experiments were attempted at any higher temperatures.

The target initial methane concentration in the experiments was 0.15 gmol/L. A high initial fuel concentration extends the range over which rates are measurable. On the other hand, low concentrations of fuel and oxidizer compared to water means that simplifying assumptions made during analysis are more accurate. At the highest temperature examined in the 270-bar experiments, i.e. at the lowest water density, the target initial fuel concentration represents a maximum mole fraction of 2%. Our choice of initial fuel concentration is high enough to measure two orders of magnitude of fuel destruction, yet low enough

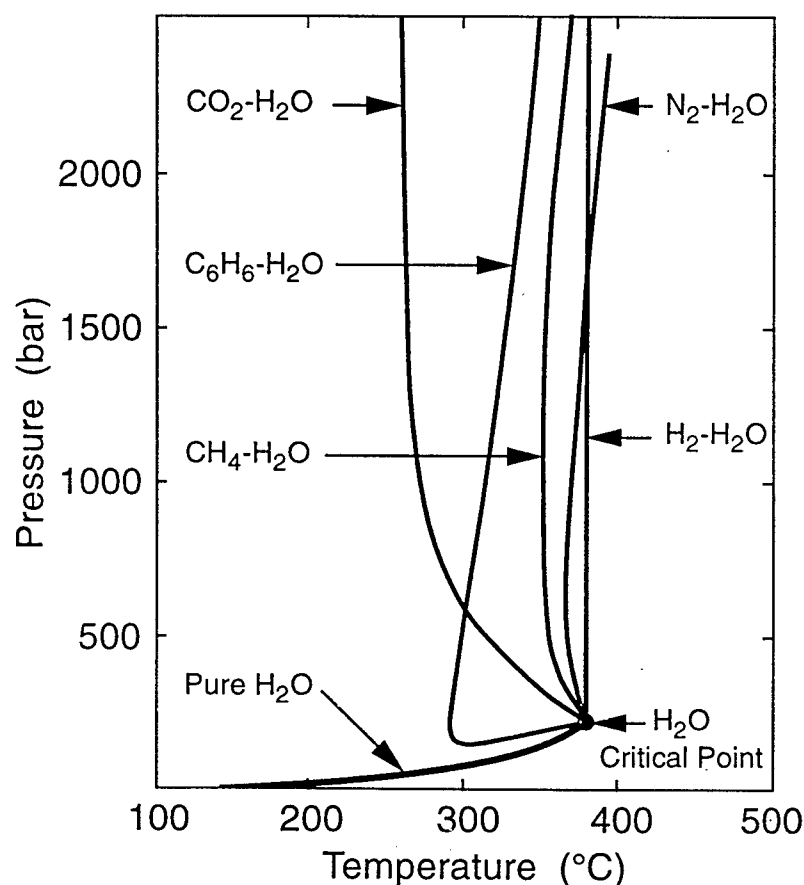


Figure 4.1. Critical curves for binary aqueous mixtures taken from Franck (1979). Each curve is the locus of mixture critical points for the various mixture compositions. Operating to the right of the curves (i.e., at higher temperatures) avoids the possibility of multiple phases. Oxygen's curve is similar to nitrogen's (Franck, 1987).

that composition changes do not affect water concentration significantly. Note that initial methane concentrations vary from the target value since the loading process involved trial and error. An estimate of concentration (based on peak height rather than integrated area) was used to guide methane addition, and a final, accurate calculation of initial concentration was not made until after each experiment.

A variety of equivalence ratios were desired to provide information concerning the global reaction order with respect to oxygen. The oxidizer injection process was such that it was difficult to predetermine the equivalence ratio. First, the amount of oxygen to be injected was estimated based on an approximate methane concentration. Second, the oxygen injection line had an uncertain amount of water in it prior to injection, so that gauging oxygen quantities by pressure rise was inaccurate. However, these difficulties only affected our ability to preselect an equivalence ratio accurately. They did not affect the accuracy of our concentration measurements.

#### 4.2.2. Experimental Procedure

Procedures for the supercritical water, subcritical water, and argon kinetics experiments were similar. Preparation included measuring Raman calibration curves and loading the heated reaction cell with water or argon (see Section 2.3.2). At least an hour delay preceded methane addition in the water experiments since the reactor temperature required about 30 minutes to recover following the addition of a full load of water. An approximate amount of methane was then added, gauged by pressure rise. Estimates of concentration based on the Raman signal guided the further addition of methane to produce an approximate 0.15 gmol/L mixture at the appropriate pressure.

The amount of oxidizer (49 mole% O<sub>2</sub>, 51 mole% N<sub>2</sub>) to be added was regulated by adjusting the pre-injection reactor pressure a calculated amount below the target experimental pressure. When temperature, pressure, and concentration of the water-methane mixture were stable, the oxidizer was injected rapidly (20 - 60 s), bringing pressure to the target value. The start of oxidizer injection marked the experiment's time zero, and Raman measurements were begun as soon as the oxidizer valve was closed.

Early in the experiment, Raman measurements were made as quickly as possible for the species being monitored (methane, oxygen, carbon dioxide, carbon monoxide, and nitrogen). With exposure times of 20 - 30 seconds plus the

time required to scan the spectrometer, one species was measured every 45 - 60 s. Later in the experiment as the reaction rate decreased, the sampling rate was lowered as well. The experiment was normally terminated when either fuel or oxidizer was depleted.

#### 4.2.3. Data Reduction

Data from each experiment comprise a binary file for each spectrum and one text file with a complete history of times, spectrum labels, temperatures, pressures, and laser power measurements. The spectrum files are read by a FORTRAN program which calculates and subtracts a baseline, and then integrates the Raman peak using the proper algorithm for each species (see Section 2.4). The program produces a text file with integrated intensities for the entire experiment, including the calibrations. A spreadsheet consolidates the integrated intensities and the temperature-pressure data, and is used to reduce the data as described in Section 2.4.

Data reduction performed by the spreadsheet includes the following operations. (1) Temperatures are corrected for laser heating of the thermocouple. When using high laser power (5W), the thermocouple temperature abruptly rises from 1 to 4 °C whenever the laser beam is propagated through the reactor. Although the beam doesn't directly hit the thermocouple, there is enough reflected light to raise its temperature by a few degrees; the temperature returns to its previous level within 5 seconds of shuttering the laser. Several times during each experiment, the difference between laser-on and laser-off temperatures is noted and used for the spreadsheet correction. (2) Integrated intensities are normalized based on laser output power. (3) Calibration concentrations are calculated based on measured temperatures and pressures using the ideal gas equation of state. Since calibrations are conducted at elevated temperatures (~400 °C) and relatively low pressures (< 60 bar), the ideal gas equation of state is accurate within 1.5% (compressibilities are within 1.5% of 1). (4) The slope of the concentration vs. integrated intensity calibration data is calculated for each gas; these values are used in turn to calculate concentrations from spectra recorded during the kinetics experiments. (5) Finally, clock times are shifted so that the experiment time zero coincides with the start of oxidizer injection. In addition, the Raman measurement of initial methane concentration is shifted to time zero although it is actually recorded earlier and assumed to remain constant until oxygen is injected.



#### 4.2.4. Experimental Results

The final form of the data included in the spreadsheet is a list of concentrations versus time for each of the monitored species (see Appendix, Section 7.3). Figure 4.2 presents this data in graphical form for a typical 270-bar experiment. The steady consumption of  $\text{CH}_4$  and  $\text{O}_2$  is evident along with the production of  $\text{CO}_2$ . The minor species  $\text{CO}$  has a much weaker signal-to-noise ratio due to its lower concentration, but its production and depletion can still be monitored early in the experiment. A long time scale decline of nitrogen concentration is visible as discussed in Section 2.5.2. If no reaction occurred, the first oxygen and nitrogen points would nearly coincide on the graph since the oxidizer is composed of a 49:51 mix of oxygen and nitrogen. The difference seen in the actual data represents both the early consumption of oxygen as well as increased concentration fluctuations in the earliest data points due to the mixing process. For purposes of the global fit analysis (see Section 4.2.5), initial  $\text{O}_2$  concentration is established by extrapolating the  $\text{N}_2$  concentration backwards to time zero (ignoring the data during the short settling time).

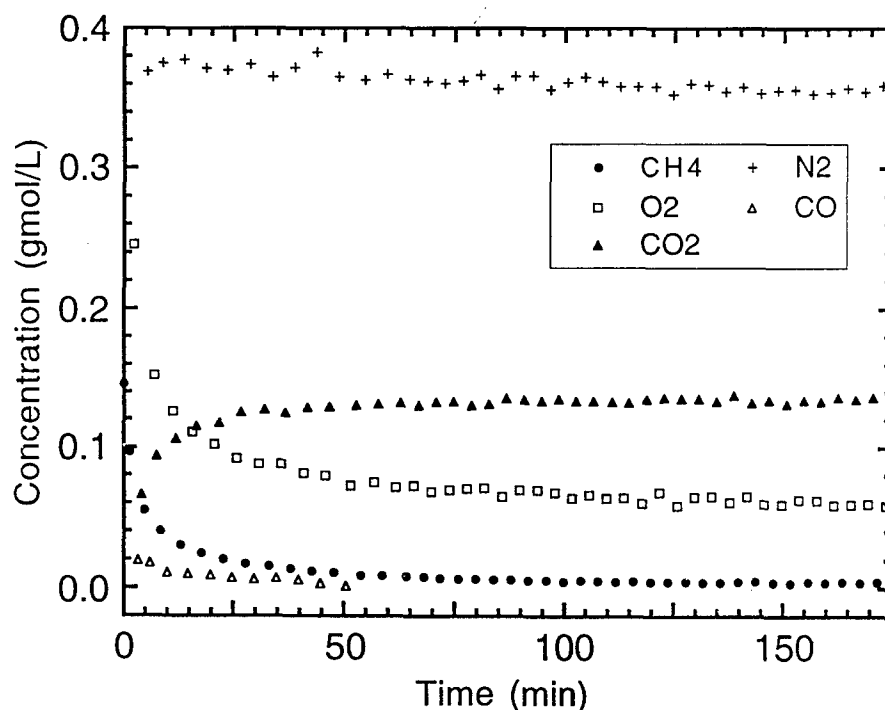


Figure 4.2. Results from the constant volume reaction of methane with oxygen in supercritical water at  $T = 413^\circ\text{C}$  and  $P = 265$  bar. Experiment #09014. (Zero is offset on the vertical axis.)

Carbon monoxide data are not as complete as the other species. Not all of the experiments included CO measurements. In addition, CO was the last species in the sequence of Raman measurements for a given experiment, meaning that the first CO data point occurred relatively late. As a result, the initial rise of CO concentration, and its true maximum value, were captured in only some of the experiments. The CO concentration history in Figure 4.2 is typical of the 270-bar experiments. An initial rapid rise of CO to a concentration about 10% of the initial methane concentration in the first minutes is immediately followed by a decline of CO that parallels the disappearance of methane. In experiments with excess oxygen, the observed drop in concentration continues to the CO detection limit, about 0.001 gmol/L.

With the current apparatus, the possibility exists to measure other species as well. In the tests reported here, only occasional attempts to identify reaction intermediates were made. During one methane experiment, formaldehyde was included in the list of Raman spectra recorded. Figure 4.3 shows a formaldehyde spectrum recorded 200 seconds into a methane run at 403 °C, 138 bar, and fuel-lean conditions. No calibration is available to determine an accurate concentration, but if a Raman response no stronger than methane is assumed, a lower limit of 0.002 gmol/L is obtained for formaldehyde concentration.

Various balances can be used to test the consistency of our experimental data. For example, Figure 4.4 presents carbon and oxygen balances for the experiment of Figure 4.2. To perform the balances, the discrete concentration measurements for each species are fit with a smoothed approximating curve that permits concentrations to be summed at all times. The line marked *C balance* represents the sum of CH<sub>4</sub>, CO<sub>2</sub>, and CO smoothed concentrations. Theoretically this line should equal the initial methane concentration—indicated on the graph as a dashed line. The balance agrees with the theoretical value within 5%. The early time excess of carbon is due to uncertainty in the carbon monoxide concentrations: CO concentrations are based on calibrations performed a different day from the experiments (see Section 2.5.1).

The oxygen balance in Figure 4.4 is calculated by summing O<sub>2</sub> and CO<sub>2</sub> concentrations, half the CO concentration, plus the change in CH<sub>4</sub> concentration (to account for H<sub>2</sub>O formed). Based on the 49:51 number ratio of O<sub>2</sub> to N<sub>2</sub>, this balance should theoretically lie 4% below the observed N<sub>2</sub> concentrations. In this example, it falls about 6% below, putting it within 2% of the theoretical value.

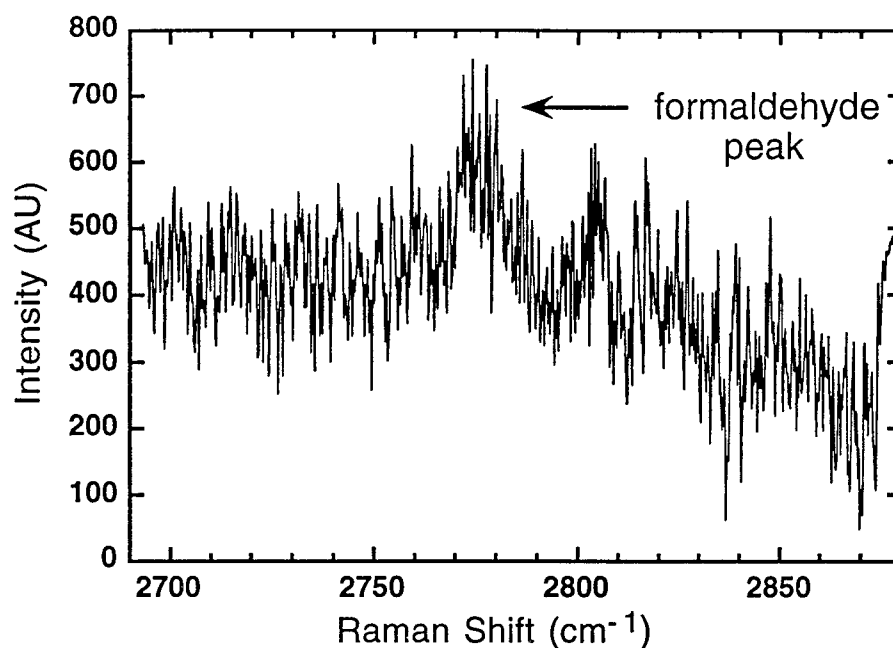


Figure 4.3. Raman spectrum of formaldehyde recorded during the reaction of methane and oxygen in water at 138 bar and 403 °C (experiment #08054). The weak signal centered at a Raman shift of 2778 cm<sup>-1</sup> is in good agreement with the literature value of 2780 cm<sup>-1</sup> (Herzberg, 1945).

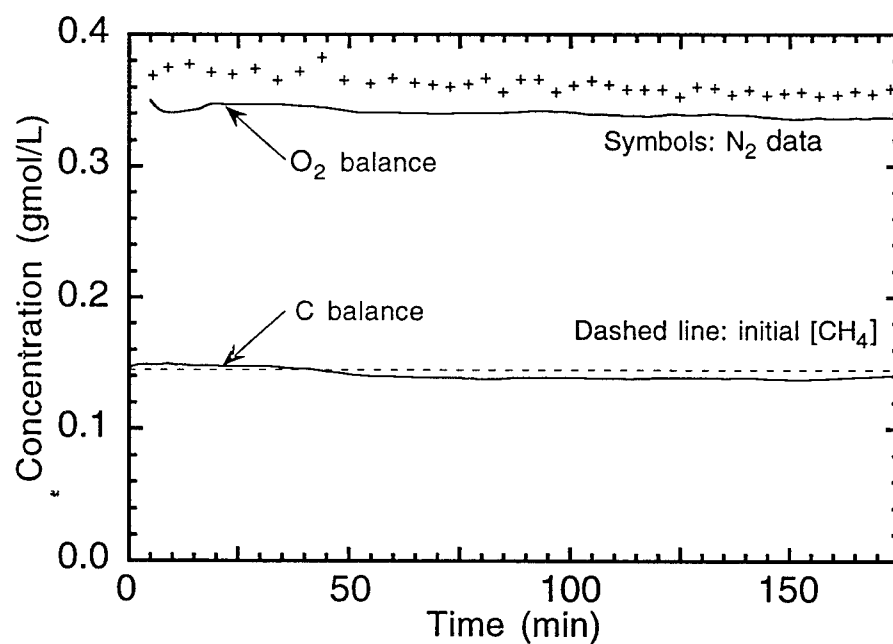


Figure 4.4. Carbon and oxygen balances performed on the experiment of Figure 4.2.

Mass transport of  $\text{CO}_2$  and  $\text{CO}$  out of the reactor into the external volume could contribute to this discrepancy. Transport of  $\text{O}_2$  and  $\text{N}_2$  is not the likely cause since diffusion of the two should occur at similar rates. Nor is  $\text{CH}_4$  transport responsible: methane's concentration gradient would cause it to *enter* the reactor, *increasing* the value of the oxygen balance. Thus, only diffusion of  $\text{CO}_2$  and  $\text{CO}$  contributes to the oxygen deficit in Figure 4.4.

The pressure and temperature histories for the experiment of Figure 4.2 are shown in Figure 4.5. Note that the data points for both pressure and temperature at time zero are low because they are actually recorded prior to oxidizer injection, i.e., at the time initial fuel concentration is measured. In this experiment, there is a temperature rise associated with oxygen injection of about  $7^\circ\text{C}$ . In general, this early temperature rise ranged from  $2 - 10^\circ\text{C}$  for the 270-bar experiments (see Table 4.1) and was of short duration (see Section 2.5.3). In some of the least-squares fits of the next section, the first few data points of each experiment are discarded to eliminate the effects of temperature excursions.

During each 270-bar experiment, the pressure fell 2 - 5%. In the example of Figure 4.5, the decrease is 12 bar. Part of the pressure drop is due to falling

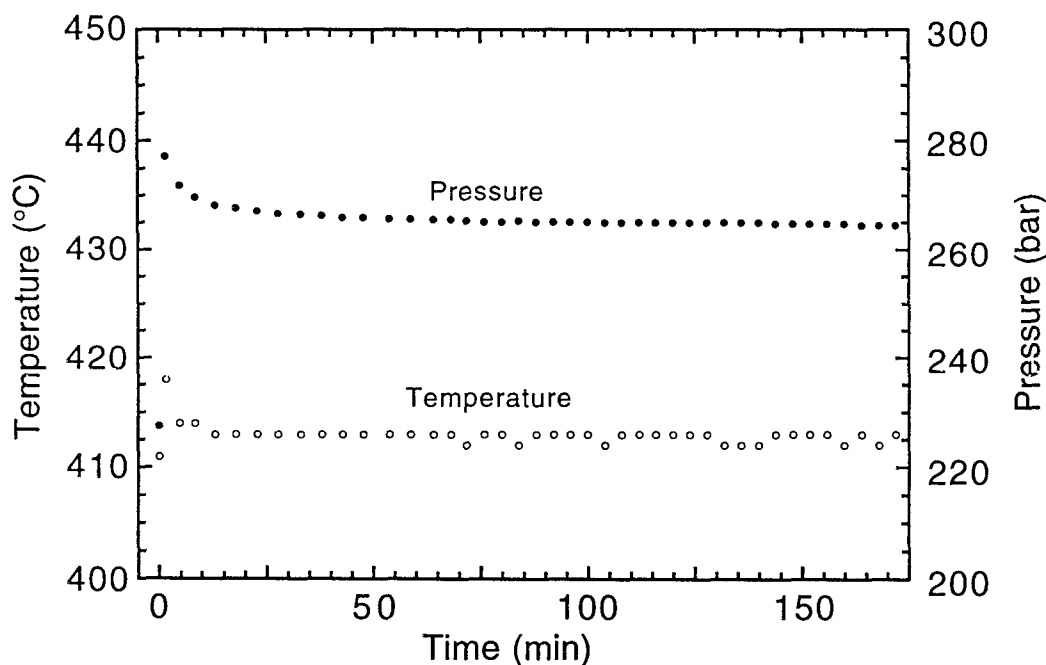
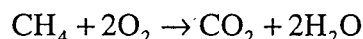


Figure 4.5. Pressure and temperature history for the experiment of Figure 4.2. (Zero is offset on the time axis.)

temperature after the initial increase. In the current example, there is a temperature drop of about 5 °C that would cause a pressure drop of 7 bar in pure water at these conditions. An unknown amount of pressure drop is due to equilibration processes in the unheated external volume, e.g., condensation of water. The remainder of the observed pressure variation is attributed to non-ideal behavior of the combustion gases in aqueous solution, combined with deviations from one-step (equimolar) methane stoichiometry. Pressure leaks were assumed negligible since non-reacting experiments (e.g., the settling time experiments in Section 2.5.2) showed less than 1 bar pressure variations.

#### 4.2.5. Global Fit

The data from the 15 high-pressure experiments represent over 550 separate rate measurements covering a range of temperatures, methane concentrations, and equivalence ratios. To facilitate comparison of these data with other rate measurements—e. g., the low pressure data from the same reactor, as well as data from other studies—we fit our data using a one-step, or global, reaction mechanism:



The corresponding reaction rate expression is:

$$d[\text{CH}_4]/dt = -k[\text{CH}_4]^a[\text{O}_2]^b \quad 4.1$$

where the rate coefficient  $k = A \exp(E_a/RT)$ ,  $A$  is the preexponential factor,  $E_a$  is the activation energy,  $R$  is the gas constant,  $a$  is the reaction order with respect to methane, and  $b$  is the reaction order with respect to oxygen. Units are in terms of kcal, gmol, L, s, and K.

To perform the fit, a non-linear, least-squares routine (Marquardt, 1963) was used with time as the independent variable and methane concentration as the predicted variable. The four fit parameters were  $A$ ,  $E_a$ ,  $a$ , and  $b$ . Within each experiment, initial methane concentration, initial oxygen concentration, and temperature were fixed parameters. For simplicity, instantaneous oxygen concentration was approximated in Equation 4.1 using one-step stoichiometry, i.e., each mole of reacted methane was assumed to consume two moles of oxygen. Using our experimental oxygen concentrations would have required fitting each experiment's  $\text{O}_2$  measurements as a function of time and including

them all in the fitting routine. This approach was rejected as unwarranted in the simplified global rate analysis, especially since reaction orders with respect to oxygen were expected to be small (Webley and Tester, 1991).

Substituting for the oxygen concentration, Equation 4.1 becomes:

$$[\text{CH}_4]_{\text{predicted}} = [\text{CH}_4]_{\text{initial}} - \int_0^{t_{\text{observed}}} k[\text{CH}_4]^a ([\text{O}_2]_{\text{initial}} - 2([\text{CH}_4]_{\text{initial}} - [\text{CH}_4]))^b dt \quad 4.2$$

The fitting program called an ordinary differential equation solver to numerically integrate Equation 4.2 once for each observed data point, resulting in a set of predicted methane concentrations. The quality of the fit was measured by its *variance*, calculated using the predicted and observed data. The variance was calculated using different algorithms in the several fits performed. For the first fit, Fit 1, variance was based on a simple difference of methane concentrations:

$$\text{variance} = \frac{\sum \left( \frac{[\text{CH}_4]_{\text{predicted}} - [\text{CH}_4]_{\text{observed}}}{\text{std. deviation}} \right)^2}{\text{num. data pts.} - \text{num. fit params.}} \quad 4.3$$

where the input standard deviations were all set to 1. However, since methane concentration decreases by more than an order of magnitude, this method produces errors in predictions at long times (low concentrations) that are proportionately much larger than those at short times (high concentrations). If the fit parameters  $a$  and  $b$  obtained from Fit 1 (listed in Table 4.2) are approximated as  $a = 2$  and  $b = 0$ , the rate equation (Equation 4.1) becomes

$$d[\text{CH}_4]/dt = -k[\text{CH}_4]^2,$$

or, when integrated,

$$1/[\text{CH}_4] = 1/[\text{CH}_4]_{\text{initial}} + kt.$$

Since this equation is linear in *inverse* methane concentration, a corrected variance can be written to weight the data evenly for the case of  $a = 2$  and  $b = 0$ :

$$\text{variance} = \frac{\sum \left( \frac{1/[\text{CH}_4]_{\text{predicted}} - 1/[\text{CH}_4]_{\text{observed}}}{1/\text{std. deviation}} \right)^2}{\text{num. data pts.} - \text{num. fit params.}} \quad 4.4$$

Using Equation 4.4 in Fit 2 resulted in a set of parameters that agree with the assumed values of  $a \sim 2$  and  $b \sim 0$ , as seen in Table 4.2.

Table 4.2 presents the results of several fits. Comparing the first two fits, note that the variance of Fit 2 is worse than that of Fit 1. (For purposes of comparison, all variances reported in Table 4.2 are recalculated using Equation 4.3.) Thus the price of correctly weighting the data is an increase in variance. The improvement in the fit gained by using a corrected variance can be seen in a graphical comparison of Fits 1 and 2. Figure 4.6 shows that the asymmetric offset of low concentration points in Fit 1 is corrected in Fit 2. The Fit 2 variance translates into an average error of 0.011 gmol/L in predicted methane concentrations. With the exception perhaps of 3 runs out of 15, the fit closely predicts the observed data: this is most easily visualized by examining the graphs of observed and predicted concentration histories which are reproduced in Figure 4.7.

One final fit, Fit 3, was performed for the 270-bar data. It uses the same variance algorithm as Fit 2, but the first 2 or 3 concentration measurements of each experiment were discarded to eliminate data taken during the settling period. Using an abridged data set removes any possible effects due to fuel

Parameter	Fit 1	Fit 2	Fit 3	Webley Fit
Preexponential Factor, $\log A$ (units of gmol, L, and s)	27.1 ( $\pm 0.99$ )	21.3 ( $\pm 0.60$ )	17.1 ( $\pm 0.49$ )	11.4 ( $\pm 1.1$ )
Activation Energy, $E_a$ (kcal/gmol)	86.9 ( $\pm 3.1$ )	71.8 ( $\pm 1.8$ )	60. ( $\pm 1.4$ )	42.8 ( $\pm 4.3$ )
Reaction Order w.r.t. $\text{CH}_4$ , $a$	2.44 ( $\pm 0.10$ )	2.17 ( $\pm 0.088$ )	1.8 ( $\pm 0.084$ )	0.99 ( $\pm 0.08$ )
Reaction Order w.r.t. $\text{O}_2$ , $b$	0.68 ( $\pm 0.10$ )	-0.061 ( $\pm 0.062$ )	-0.06 ( $\pm 0.065$ )	0.66 ( $\pm 0.14$ )
Variance	$6.5 \times 10^{-5}$	$1.1 \times 10^{-4}$	$5.4 \times 10^{-5}$	$1.8 \times 10^{-9}$

Table 4.2. Least-squares fit parameters for high-pressure methane kinetics experiments. For Fits 1, 2, & 3,  $P \sim 270$  bar,  $T = 390 - 442$  °C. For the Webley Fit,  $P = 245.8$  bar,  $T = 560 - 652$  °C (Webley and Tester, 1991). Uncertainties are at the 95% confidence level.

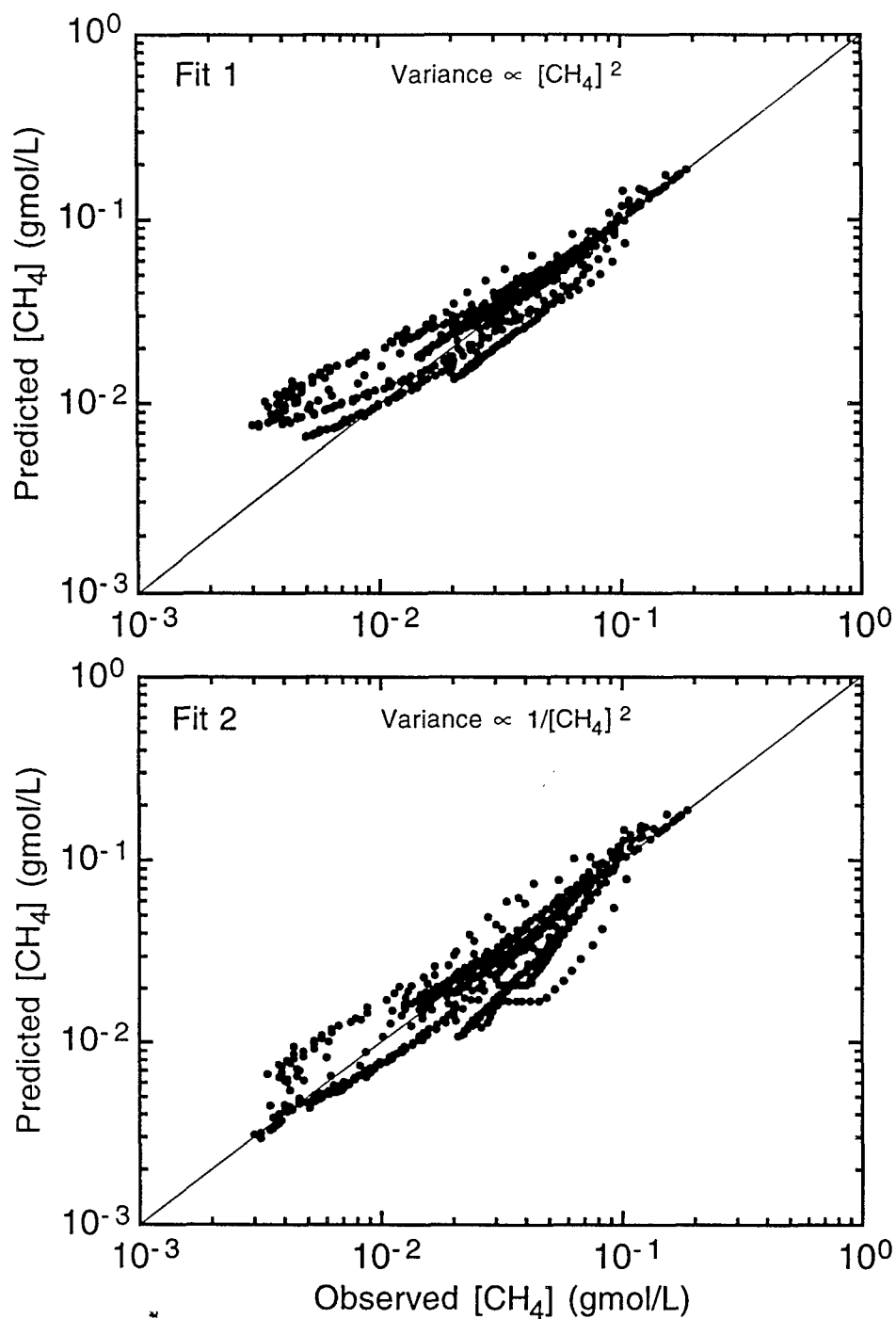


Figure 4.6. Comparison of one-step reaction mechanism predictions and observed methane concentrations for the high-pressure experiments in two different fits. Perfect agreement occurs along the diagonal line.



deficit, temperature excursions, incorrectly estimated initial oxygen concentrations, and incomplete mixing. The first methane measurement retained in each experiment becomes the initial fuel concentration at time zero, and the initial oxygen concentration is obtained for the same moment in time by interpolating the measured data. Of course, this abridged fit discards any information from the reaction's induction period. For several reasons, this was deemed acceptable. First, the simple reaction rate expression being used, Equation 4.1, is not appropriate for modeling the induction period. Second, the fit is to be used in the comparison of overall reaction rates at varying pressures and temperatures—a function not requiring such details. Finally, information on reaction rates for the extended period that follows induction is valuable for use in engineering models of SCWO.

Table 4.2 includes the results of Fit 3. Not surprisingly, it has the best variance of the three fits. Comparing the two fits performed using a corrected variance expression (Fits 2 and 3), the abridged data set is seen to reduce all fit parameters 10 to 20% but reinforce a conclusion that reaction order with respect to methane is significantly higher than unity, and reaction order with respect to oxygen is effectively zero. To put these results in perspective, the published fit parameters from Webley's methane oxidation experiments (Webley and Tester, 1991) are included in Table 4.2. Webley's experimental apparatus dictated initial methane concentrations in the range 0.001 - 0.004 gmol/L, about 2 orders of magnitude lower than our initial concentrations, and about equal to our lowest measured values. They chose a temperature range (560 - 652 °C) well above ours since their residence times (~ 10 s) were several orders of magnitude shorter. Their higher temperature range means that their water densities were 2 - 5 times lower than in the current experiments.

Table 4.2 reveals that our Fit-3 parameters differ significantly from those of Webley. First, our activation energy is significantly higher than their value, indicating a much stronger temperature dependence. Second, at our elevated concentrations, reaction order with respect to methane concentration is nearly double their number. This means that estimates of reaction rates based on low-concentration experiments would severely underpredict rates at higher concentrations, e.g., at concentrations typical of commercial SCWO processes. Previous SCWO kinetic studies of several fuels mostly report (or assume) a first-order rate dependence on fuel concentration. Values of fuel reaction order close

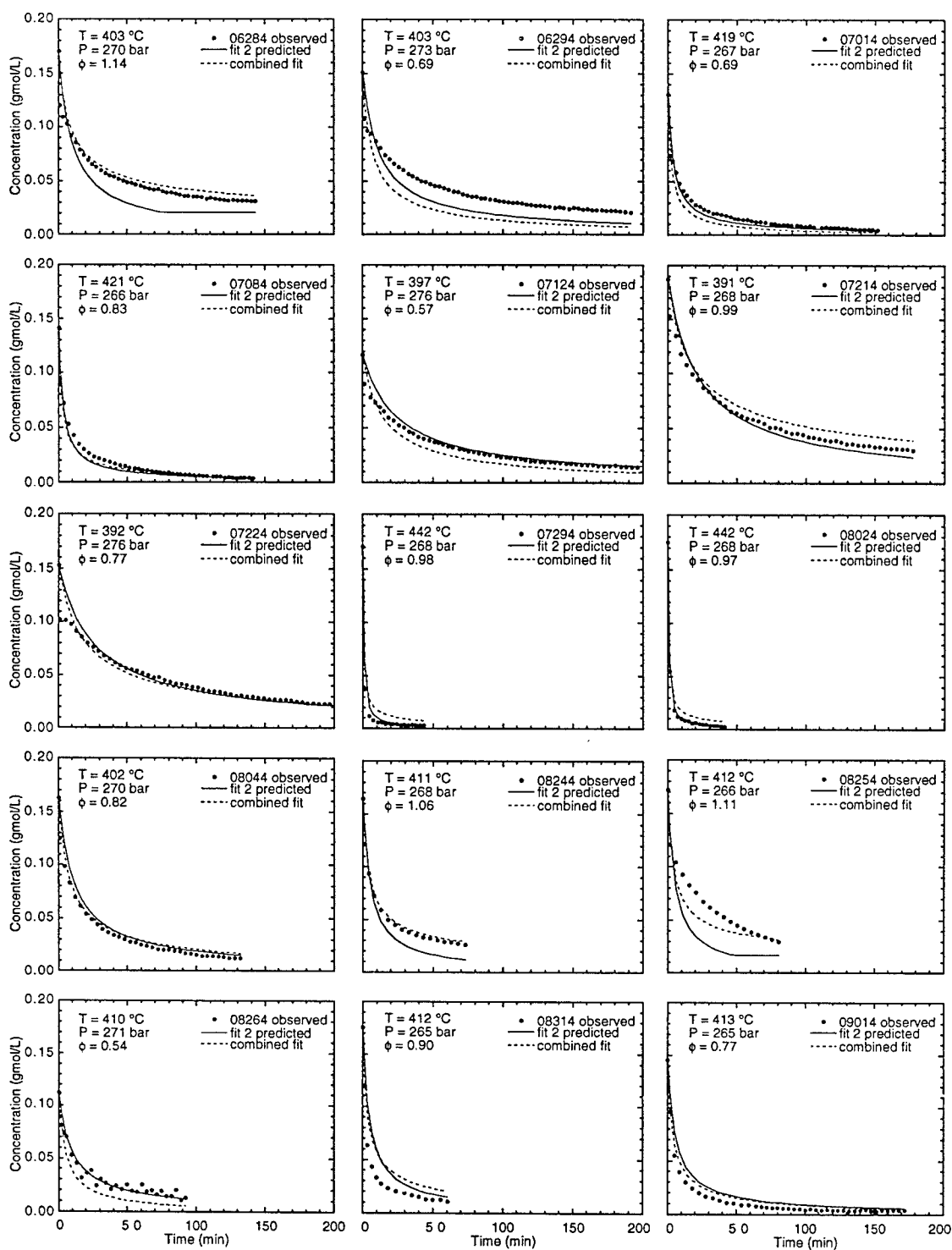


Figure 4.7. Comparison of global reaction mechanism predictions and observed methane concentration histories for the 270-bar experiments.

to unity have been determined for methane, carbon monoxide, methanol, and hydrogen (Webley and Tester, 1991; Holgate and Tester, 1994a; Tester, *et al.*, 1993b; Holgate and Tester, 1993). The same was found for phenol (Thornton and Savage, 1990), acetamide, and acetic acid (Lee and Gloyna, 1990). In light of our results, it is interesting to note that Yang and Eckert (1988) found a reaction order for p-chlorophenol that increased from 1 to 2 as concentration was increased.

A third difference seen in comparing parameters of Table 4.2 involves reaction order with respect to oxygen. The oxygen order is the same in Fit 1 as in Webley's fit, but when the low-concentration bias is removed in Fit 2 and Fit 3, the oxygen order becomes effectively zero for our experiments. Zero-order oxygen dependence in SCWO chemistry has been observed in prior studies of methanol and carbon monoxide (Tester, *et al.*, 1993b; Helling and Tester, 1987). Finally, the variances of the fits in Table 4.2 can be compared. Since the variances are a measure of average squared errors, the square roots of these numbers represent average errors in the predicted concentrations. Dividing the square roots of the variances by average initial fuel concentrations produces a relative average error of 9% in Fit 3 and 1% in the Webley Fit.

There are several uncertainties inherent in the global fits. First, empirical fits to global reaction mechanisms cannot be safely extrapolated beyond their range of experimental conditions. Second, the preexponential factor and activation energy are highly correlated (correlation coefficient = 0.98) in each of these fits, meaning that a change in  $A$  can be compensated by a change in  $E_a$ . Thus similar variances can result in two fits with significantly different fit parameters. Finally, it should be emphasized that empirically derived parameters are not strongly tied to actual physical parameters since the actual chemistry is far more complex than the one-step mechanism used in the fits.

Because of these uncertainties, the differences between Webley's and the current fit's parameters in Table 4.2 do not necessarily mean that the data sets are inconsistent. In fact, the data from both experiments can be fit simultaneously without a large increase in variance over Fit 3. Table 4.3 shows the results of such a combined fit. In order to give the data sets equal weighting, the Webley set was duplicated as necessary to yield the same number of points as in our set. To compensate for the difference in concentration range, the input standard deviations were set to 1 for our data, and 0.01 for the Webley data. Since the Webley data doesn't follow a second-order methane dependence, variance for all data was calculated using Equation 4.3. The resulting variance of the

combination fit, listed in Table 4.3, does not increase greatly over Fit 3, indicating a comparable overall fit. The error on the Webley points increases so that the average relative error on that set (based on initial concentrations) is about 10%—the same as on the Sandia set. The increase in reaction order with respect to oxygen is an unfortunate artifact of the fit since it implies a sensitivity to oxygen higher than in either the current or Webley fits.

Parameter	Combined Fit
Preexponential Factor, $\log A$ (units of $\text{gmol/L and s}$ )	24.67 ( $\pm 0.088$ )
Activation Energy, $E_a$ ( $\text{kcal/gmol}$ )	80.9 ( $\pm 0.20$ )
Reaction Order w.r.t. $\text{CH}_4$ , $a$	1.74 (0.048)
Reaction Order w.r.t. $\text{O}_2$ , $b$	1.24 ( $\pm 0.040$ )
Variance	$8.8 \times 10^{-5}$

**Table 4.3 One-step reaction mechanism parameters for the combined fit.**

The relative success of the combined fit in matching the current data can be seen in Figure 4.7 which includes concentration profile predictions of the fit for each of the current experiments. The combined fit also matches the Webley data well, as indicated in Figure 4.8. Thus in spite of significant differences in operating conditions of the two experimental studies, the combined fit provides an estimate of methane oxidation rates in supercritical water for the full range of temperatures from 390 - 630 °C and concentrations from  $10^{-4}$  to  $10^{-1}$   $\text{gmol/L}$ . This fit is appropriate for use in engineering models of SCWO. The results underline the danger of using models based on experiments conducted at concentrations well below the intended application. A model based on such data alone would significantly underpredict reaction rates at typical SCWO initial concentrations, leading to designs with overly long residence times or unnecessarily high operating temperatures.

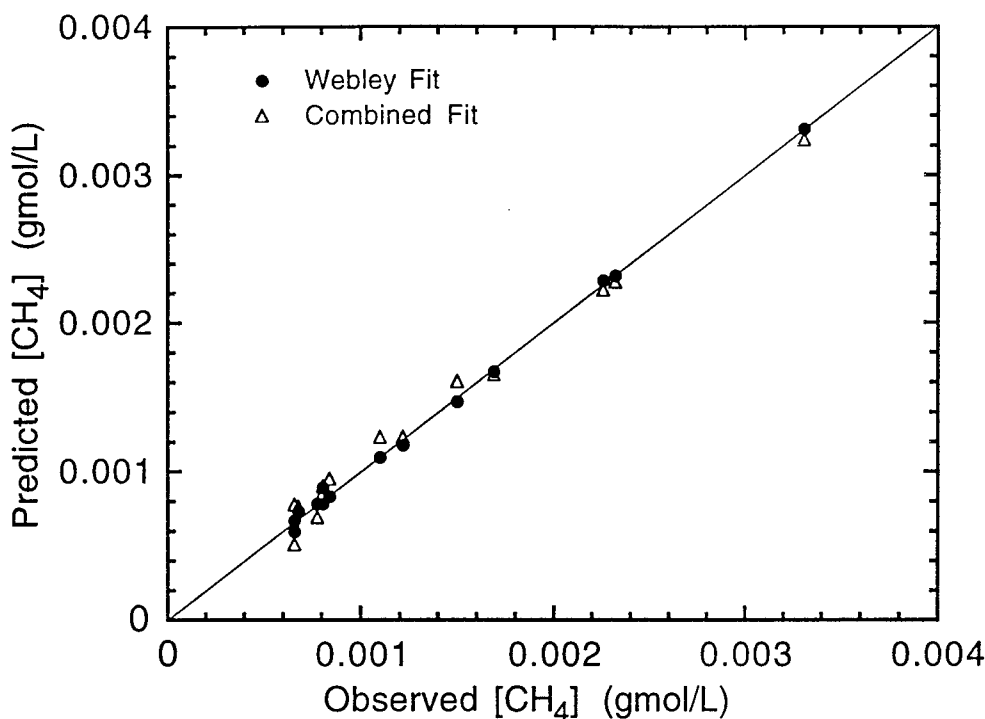


Figure 4.8. Performance of the combined fit in predicting the Webley data (Webley and Tester, 1991). Performance of Webley's fit to Webley's own data is shown for comparison.

### 4.3. Kinetics Measurements In Subcritical Water

An important variable in the design of SCWO processes is the choice of operating pressure; existing commercial processes cover a wide range of pressures from sub- to supercritical. However, few experiments have been performed to reveal the effect of pressure on oxidation kinetics in this environment. Holgate and Tester (1994a) studied the effects of operating pressure on the kinetics of H<sub>2</sub> and CO. Their experiments were performed at constant initial fuel concentrations of 10<sup>-6</sup> gmol/L while pressure was varied between 120 and 260 bar by adjusting the water fraction. Their results showed a several-fold increase in apparent first-order rate constant ( $k^*$ , from the expression,  $\text{rate} = k^*[\text{CH}_4]$ ) with increasing pressure over this range. This section describes current experiments conducted to measure the effects of water density on the rate of methane oxidation. These experiments comprise the first two groups listed in Table 4.4. The third group of experiments listed in Table 4.4, experiments performed in argon, is discussed in Section 4.4.

### 4.3.1. Experimental Conditions

The first two categories in Table 4.4 contain all the experiments conducted in *subcritical* water. The first group was performed at a constant pressure of 135 bar over a range of temperatures. The second group covers a wide range of subcritical pressures at a constant temperature of about 412 °C. For all these experiments, initial methane concentrations were held approximately constant, while pressure was controlled by adjusting the initial fraction of water.

Exper. #	Avg. Temp (°C)	Avg. Press (bar)	Temp. Range (°C)	Press. Range (bar)	Initial [O <sub>2</sub> ] (gmol/L)	Initial [CH <sub>4</sub> ] (gmol/L)	Initial Equiv. Ratio	Run Time (min)	# of CH <sub>4</sub> Points
<b>Experiments in H<sub>2</sub>O at 135 bar:</b>									
06174	404	139	404-405	139	0.40	0.016	0.08	40	15
06274	404	144	404-406	143-146	0.43	0.111	0.52	115	33
07064	415	136	414-424	135-137	0.32	0.128	0.80	65	25
07074	419	138	419-426	137-140	0.38	0.133	0.70	45	18
07134	398	137	396-398	136-138	0.42	0.109	0.52	150	42
07144	391	136	388-392	135-139	0.34	0.103	0.61	180	56
08054	402	135	401-407	134-139	0.38	0.143	0.75	175	44
09164	412	136	411-439	136-139	0.33	0.160	0.97	60	15
09284	411	134	410-417	134-138	0.26	0.119	0.92	125	29
10034	410	134	410-418	133-138	0.24	0.142	1.18	120	26
10074a	412	136	410-417	135-139	0.18	0.121	1.35	40	6
10074b	412	139	411-413	138-142	0.22	0.102	0.92	50	11
<b>Experiments in H<sub>2</sub>O at other pressures:</b>									
10114	411	69	410-414	68-70	0.22	0.115	1.05	120	27
10124	410	35	410-411	35	0.28	0.114	0.82	170	36
10134	412	50	411-414	49-50	0.25	0.102	0.82	140	29
10144	412	62	410-414	62-63	0.25	0.104	0.83	150	32
10184	412	202	411-412	201-209	0.27	0.106	0.78	115	25
<b>Experiments in argon:</b>									
08174	412	277	411-424	276-280	0.47	0.146	0.62	90	25
08184	412	138	411-414	138-139	0.38	0.139	0.73	120	32
08234	411	171	409-415	171-172	0.40	0.129	0.64	140	36

Table 4.4. Summary of kinetics experiments in subcritical water and in argon.

Temperatures for all the experiments in Table 4.4 are above the assumed mixture critical temperatures as discussed in Section 4.2.1. As pressure drops below the critical pressure ( $P_{\text{crit}} = 221$  bar for pure water), the mixtures are no longer considered supercritical. The temperatures are high enough, however, that the mixtures are still single phase, existing as mixtures of dense gas and superheated steam.

The first group of experiments were performed at a constant pressure to permit the same global fit analysis as in Section 4.2.5. The temperature range, 391 - 419 °C, was similar to the 270-bar experiments, although the range was reduced at the high end: reaction rates were faster at these pressures, making experiments at temperatures as high as 440 °C impossible in our apparatus. At these conditions, water density varies from 0.051 - 0.058 gm/cc. Fuel equivalence ratios covered a comparable range to the earlier experiments.

In the second group of experiments in Table 4.4, initial water fraction was varied extensively while initial methane concentration was held approximately constant at 0.1 - 0.15 gmol/L. Pressures ranged from 35 - 200 bar. At the lowest pressure, the water fraction was 0, so that the initial load was entirely methane. Temperatures for these experiments were held constant at ~410 °C to facilitate a comparison of rates. Controlling fuel equivalence ratios was difficult, and constant equivalence ratios were not achieved. However, the small oxygen reaction orders determined in both the 135-bar (see below) and the 270-bar global fits suggest an insensitivity to initial oxidizer concentration.

#### 4.3.2. Experimental Procedure and Data Reduction

The procedure and data reduction for the subcritical experiments is the same as detailed in Section 4.2.2 and 4.2.3.

#### 4.3.3. Experimental Results

##### *Experiments at 135 bar*

Figure 4.9 shows the concentration histories for an experiment at 139 bar and 412 °C. Other than the lower water density, conditions for this experiment are similar to those of experiment 09014 of Figure 4.2. Comparing the fuel disappearance rate in the two figures is complicated by the lower initial methane concentration in the 139-bar experiment. However, by looking at the time required for fuel concentration to drop from a value of 0.1 gmol/L down to zero,

it is clear that rates are faster in the lower pressure experiment. This surprising result, which is not anticipated by detailed kinetics models nor by previous experiments, is examined further in Section 4.5.

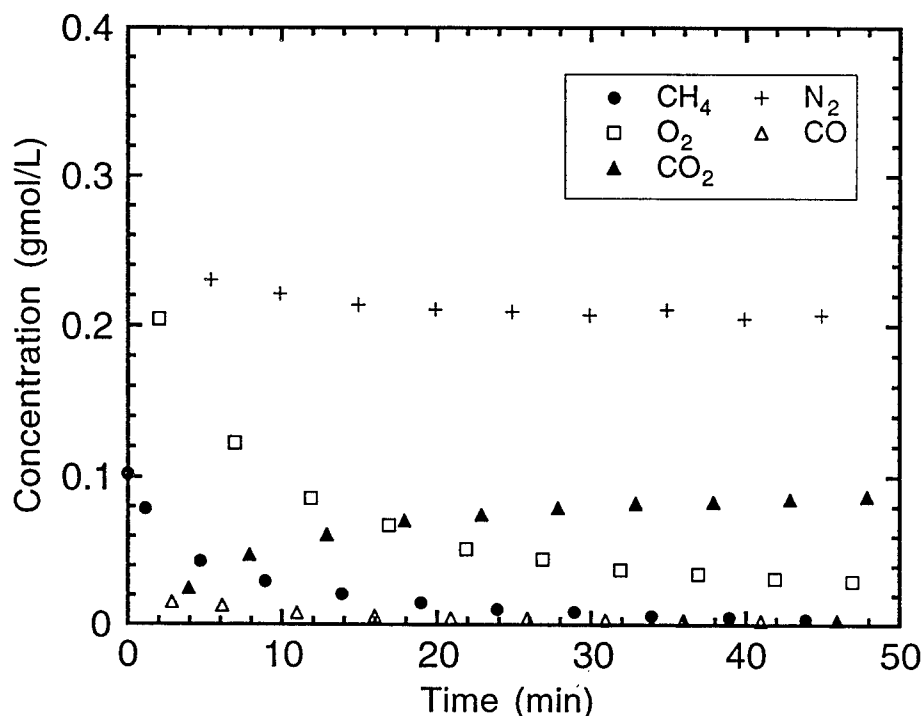


Figure 4.9. Concentration histories from the constant volume oxidation of methane in water at  $T = 412\text{ }^{\circ}\text{C}$  and  $P = 139\text{ bar}$ . Experiment #10074b.

Carbon and oxygen balances (performed as in Section 4.2.4) for the experiment in Figure 4.9 are displayed in Figure 4.10. The carbon balance reveals a fuel deficit developed during the oxidizer injection. Following a settling time of 3 minutes, the balance remains constant. Fuel deficits, not significant in the high-pressure experiments, show up at lower pressures both because initial fuel mole fractions are higher, and because the quantity of oxidizer injected constitutes a larger fraction of the final reacting mixture. The early deficit of carbon in the balance, and its relative stability thereafter, led to our decision to discard early data points in the global fit analysis of the 135-bar data.

The oxygen balance in Figure 4.10 is several percent high, due in part to the carbon deficit. Missing carbon and reacted carbon are indistinguishable in this balance, and both are counted as having consumed oxygen, leading to a surplus in the balance.



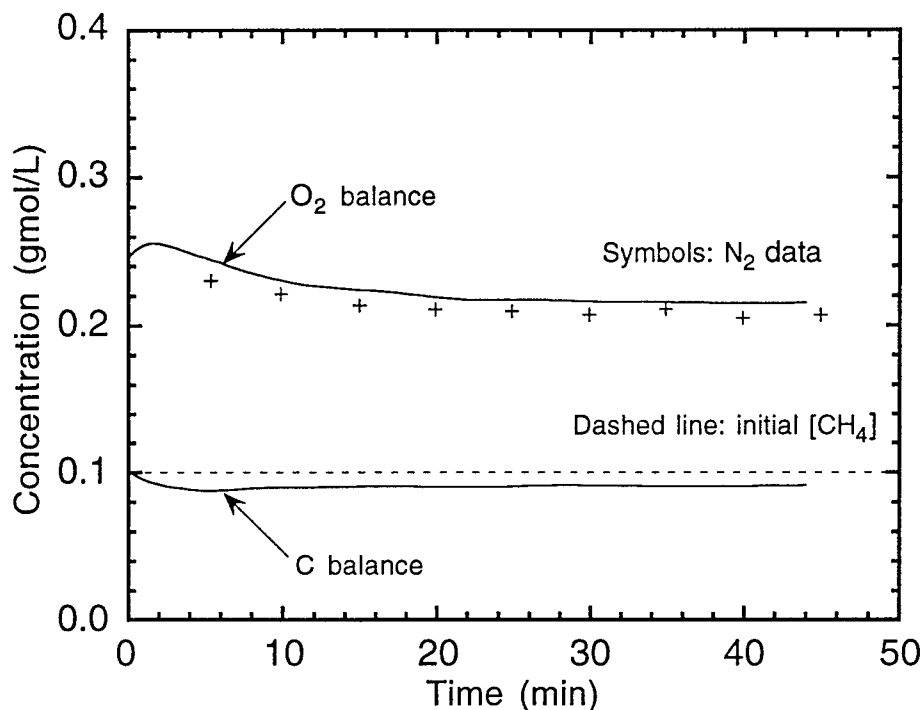


Figure 4.10. Carbon and oxygen balances performed on the experiment of Figure 4.9.

As in the 270-bar experiments, total pressure in the 135-bar experiments drops steadily following oxidizer injection. At the lower densities, however, the decline is slower—about half the rate of the high-pressure runs. Temperature rises occur during oxidizer injection as in the high-pressure runs (Section 4.2.4), with similar settling times. The observed carbon monoxide concentration profiles appear as in the earlier experiments.

#### *Experiments at other pressures*

The second group of experiments listed in Table 4.4 covers a range of subcritical pressures from 35 - 200 bar at an approximately constant temperature and initial fuel concentration. Concentration histories of three of the experiments are plotted in Figure 4.11 to illustrate differences in the settling period with changing pressure. The drop and subsequent rebound of methane concentration is conspicuous in Figure 4.11-a, which shows results of the lowest pressure experiment. This experiment started with an initial load of 100% methane (no water) at 6.8 bar, with pressure settling at 35 bar following oxidizer injection. In this experiment, the ratio of the moles of oxidizer injected to the moles initially

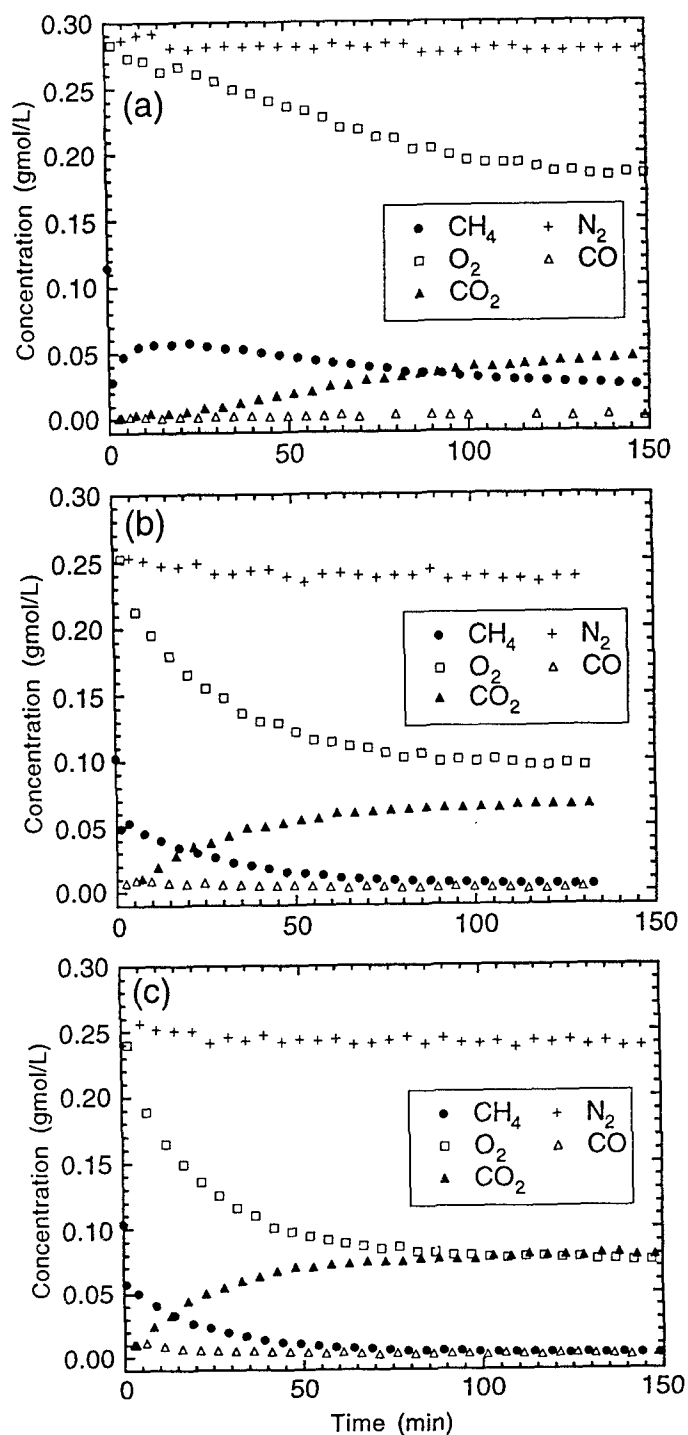


Figure 4.11. Concentration histories from the constant volume oxidation of methane in water at  $T \sim 411^\circ\text{C}$ . (a)  $P = 35$  bar, experiment #10124; (b)  $P = 50$  bar, experiment #10134; (c)  $P = 62$  bar, experiment #10144. (Zero is offset on the vertical axes.)

loaded in the reactor was at a maximum. As a result, the fuel deficit provoked by oxygen injection is the highest of all experiments. A carbon balance similar to Figure 4.10, but at the conditions of Figure 4.11-a, indicates a constant fuel deficit of about 40% following the settling period. These same conditions also maximize the driving potential for back-diffusion of methane into the reactor following injection. The observed rebound of methane concentration can be attributed to both mixing and the back-diffusion. To quantify the settling time at 35 bar, a non-reacting, settling time experiment was performed (see Section 2.5.2); the results show that fuel concentration stabilizes to within 5% of its final value (40% below the initial concentration) in 14 minutes.

The experiments plotted in Figure 4.11-b and 4.11-c were performed at increasing pressures, i.e., at increasing initial water fractions. Inspection of the concentration histories shows that fuel-concentration rebound diminishes with pressure. The steady-state fuel deficits as measured by carbon balances decrease as well.

The settling time effects described above complicate the comparison of experimental data at the different pressures. The strategy adopted is to discard data points during the settling period. The next section discusses using this strategy in a global fit of the 135-bar experiments, and Section 4.5 returns to this topic in a comparison of rates at pressures from 35 - 270 bar.

#### 4.3.4. Global Fit

The data from the 135-bar experiments represent 320 separate rate measurements covering a range of temperatures, methane concentrations, and equivalence ratios. To facilitate comparison with the 270-bar experiments, the data were fit to the same one-step reaction rate expression, Equation 4.1. Several algorithms were used in separate fits, with results as shown in Figure 4.12.

As for the 270-bar experiments, a bias at low concentrations occurs when using a variance based on simple methane concentrations (Figure 4.12-a). As previously discussed, this artifact is corrected by computing variances based on inverse concentrations (Figure 4.12-b). This procedure doesn't eliminate several conspicuous outlier points, however. Some of these are simply artificially low data points recorded early, during the settling period. In contrast, the horizontal alignment of several outlier points conspicuous in Figure 4.12-b is caused by the fuel deficit in the following way. When methane concentration drops due to

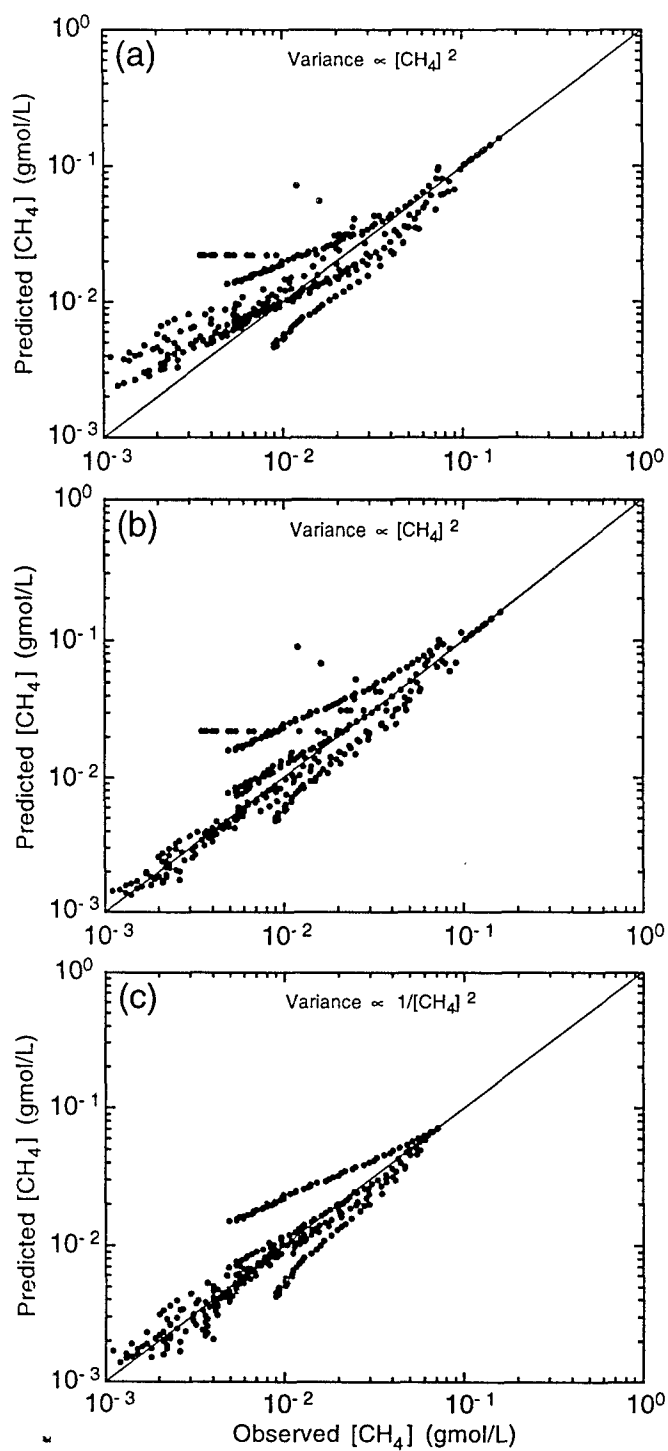


Figure 4.12. Comparison of observed and predicted methane concentrations using 3 fitting algorithms. (a) normal variance (Equation 4.3); (b) inverse  $[\text{CH}_4]$  variance (Equation 4.4); (c) inverse  $[\text{CH}_4]$  variance, abridged data set, Fit 4.

oxidizer injection (not oxidation), the fitting model assumes that the fuel has reacted with oxygen. This leads to over-consumption, and in some cases, depletion of oxygen in the model predictions. Premature depletion of  $O_2$  leads to a model prediction of constant fuel concentration, i. e., a horizontal alignment of some of the data in Figure 4.12-b. The final fit, labeled Fit 4 and shown in Figure 4.12-c, was performed after discarding the first 2 data points of each experiment. This strategy removes a few of the data points from the graph, but also brings many others in better agreement by correcting the oxygen over-consumption problem.

Parameters derived from Fit 4 are presented in Table 4.5. Using these 4 parameters in the one-step reaction mechanism yields the predictions of methane concentration histories shown in Figure 4.13. The empirical rate expression does a good job representing the observed data over most of the range of operating conditions. Data from one experiment stands out as containing most of the error of the fit. This is the lowest temperature experiment of the 135-bar data set, and Fit 4 is unable to accommodate these data well. A more even distribution of experimental temperatures would provide a better estimate of the reaction rate's temperature dependence.

Comparing the 135-bar fit parameters in Table 4.5 with the high-pressure fits in Table 4.2 indicates much higher values for preexponential factor and activation energy at lower pressure. As with the high-pressure fits however, the

Parameter	Fit 4
Preexponential Factor, $\log A$ (units of $\text{gmol}, L$ and $s$ )	35. ( $\pm 3.6$ )
Activation Energy, $E_a$ ( $\text{kcal/gmol}$ )	115. ( $\pm 11.6$ )
Reaction Order w.r.t. $CH_4$ , $a$	1.8 ( $\pm 0.14$ )
Reaction Order w.r.t. $O_2$ , $b$	0.15 ( $\pm 0.075$ )
Variance	$3 \times 10^{-5}$

**Table 4.5 One-step reaction mechanism fit parameters for the abridged set of 135-bar data. The variance used in Fit 4 is based on Equation 4.3, but the reported value for variance is based on Equation 4.4 for comparison purposes.**

correlation coefficient for these two parameters is high: when one parameter is varied, the other can compensate. (Compensation in this case means that the preexponential factor and activation energy move in the same direction.) Thus, the simultaneous increase in the two parameters may not be as significant as the numbers imply. The reaction orders with respect to methane and oxygen are close to those of Fits 2 and 3 in Table 4.2.

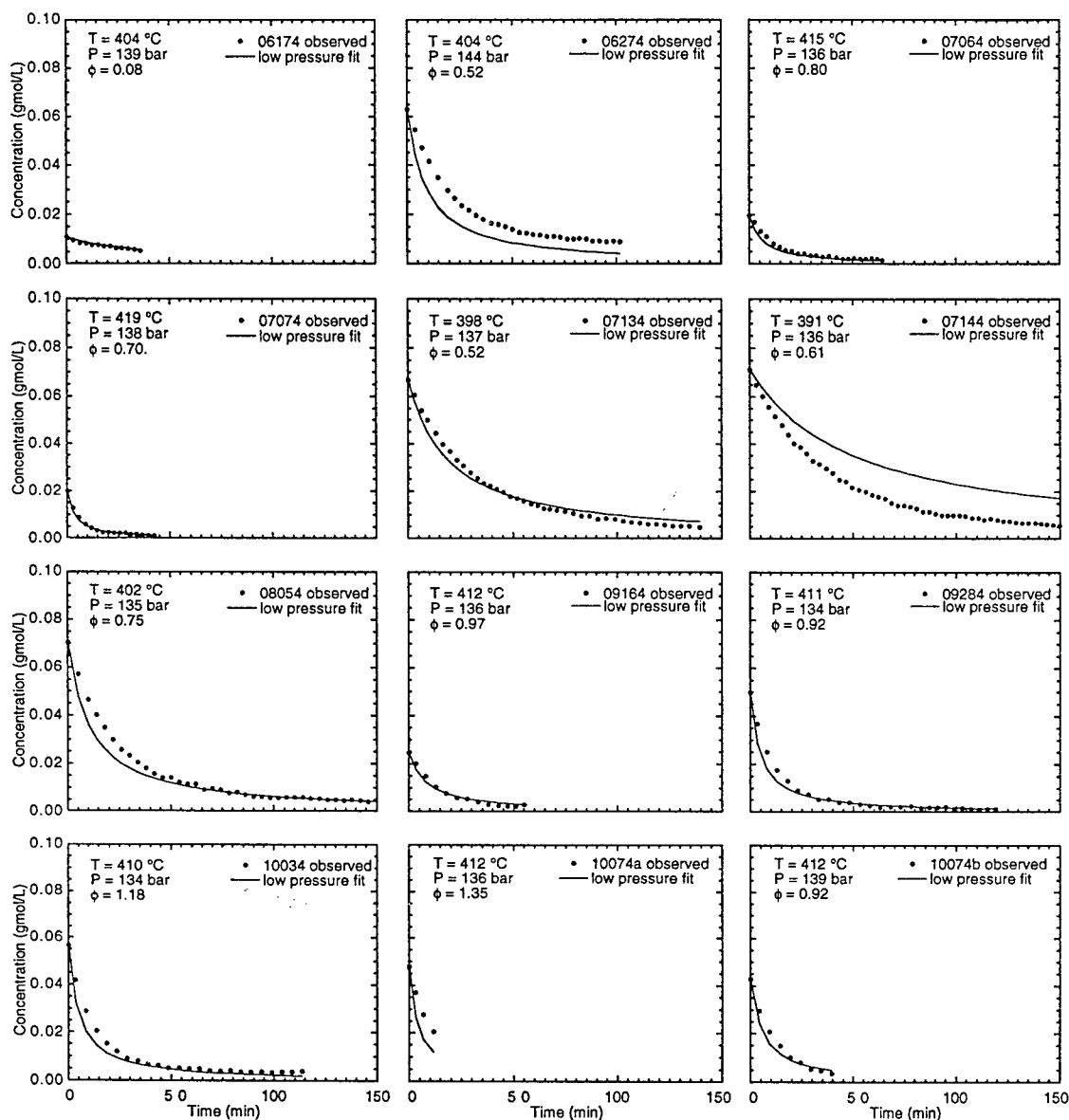


Figure 4.13. Comparison of the Fit 4 predictions and observed methane concentration histories for the abridged, 135-bar experiments.

#### 4.4. Kinetics Measurements In Argon

In order to complement the experimental examination of the effect of water density on oxidation kinetics, argon was substituted for water in three experiments listed in Table 4.4. Temperatures, initial fuel concentrations, and initial equivalence ratios were held approximately constant at values matching the earlier sequence of subcritical water experiments. Three pressures (argon densities) were selected: 138, 171, and 277 bar. The maximum pressure of these experiments matches the highest pressure of the water experiments. Experiments to match argon *number density* to the highest water number density would be desirable, but would require argon pressures over 500 bar. Such experiments were not possible due to reactor pressure limits.

Figure 4.14 shows results of the argon experiment performed at 138 bar and 412 °C. The results are qualitatively similar to the water experiments. A settling time experiment using nitrogen in place of oxygen-nitrogen showed that the fuel deficit was 7% at these conditions, with a settling time of 1 minute—an improvement over the water experiments. Reaction rates differ from the water experiments as well, and are discussed in Section 4.5. Concentration profiles of carbon monoxide are similar in shape and magnitude to the water experiments.

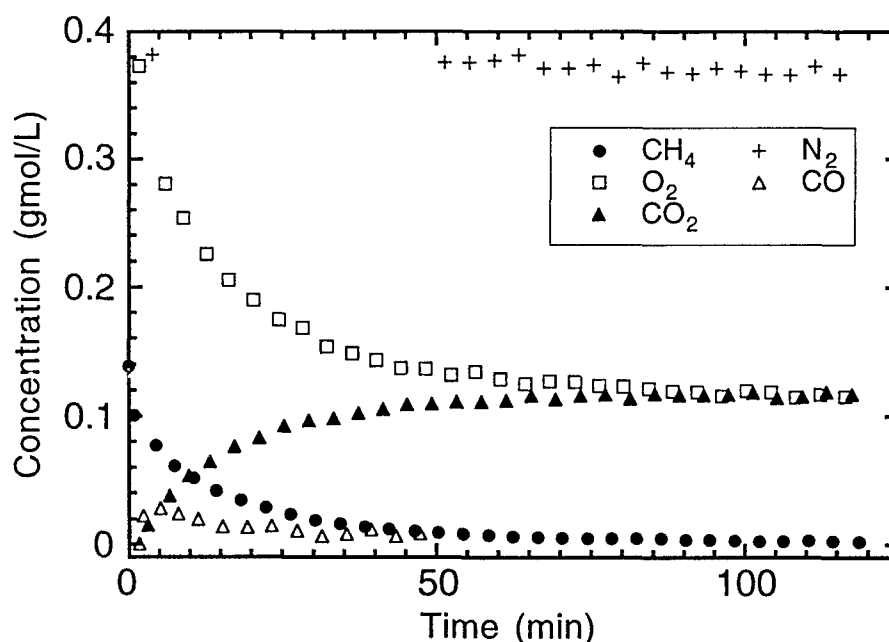


Figure 4.14. Concentration histories from the constant volume oxidation of methane in argon at  $T = 412\text{ }^{\circ}\text{C}$  and  $P = 138\text{ bar}$ . Experiment #08184. (Zero is offset on the vertical axis.)

#### 4.5. Density Dependence of Kinetics

There are several ways that varying water density can affect reaction rates in supercritical water oxidation experiments. First, varying water density by changing pressure (alone) affects *reactant* concentrations. That is, if the feedstream composition is held constant, then varying pressure results in changes in both water and reactant number densities. It is difficult to separate the effects of each on the observed reaction rates. The current experiments were performed at approximately constant initial fuel concentration to eliminate this difficulty. A second effect of water on reaction rates derives from its role as the most important collision partner in unimolecular reactions. Rates for such reactions, as long as they are not at their high-pressure limits, depend on water concentration. Third, water can be a direct participant in elementary reactions: an important example is the chain-branching step,  $\text{H}_2\text{O} + \text{HO}_2 \rightarrow \text{H}_2\text{O}_2 + \text{OH}$  (Holgate and Tester, 1994b). Finally, there is the thermodynamic effect of pressure on reaction rate coefficients. Transition state theory indicates that the change in rate coefficient with pressure is proportional to the activation volume, i.e., the difference between partial molar volumes of reactants and the transition state complex. In supercritical water, this effect can be significant since activation volumes can be large (Brennecke, 1993).

Experimental comparisons of rates at varying pressures are facilitated in the case of overall reactions that follow first order kinetics. In that case, the time required to destroy a certain fraction of fuel (i. e., the first-order time constant) is the same regardless of the starting fuel concentration. The first-order time constants or their inverses, rate constants, are used to compare experiments performed at varying concentrations, pressures, and temperatures. The results of our global fits indicate that methane reaction orders are well above unity at our experimental conditions, making such comparisons more difficult. To eliminate this difficulty, comparisons in this section are performed at constant initial fuel concentrations.

Figure 4.15 compares one experiment from the 270-bar group and one from the 135-bar group with approximately the same initial equivalence ratio ( $\Phi$ ) and temperature. Time zero has been shifted to an initial fuel concentration of 0.05 gmol/L for each experiment. The graph shows that methane is consumed noticeably faster in the *lower* pressure experiment. The same result is observed for every pair of experiments from the two groups that is similar enough in



operating conditions to compare. An even clearer comparison can be obtained by approximating the experimental concentration profiles using the global fits of Sections 4.2.5 and 4.3.4. With this strategy, exactly the same initial methane concentration, fuel equivalence ratio, and temperature can be specified at both pressures. Figure 4.15 includes predicted profiles of Fits 3 and 4 with initial conditions chosen to match the experimental conditions. Once again, the results indicate that consumption of methane proceeds far more rapidly at the lower pressure.

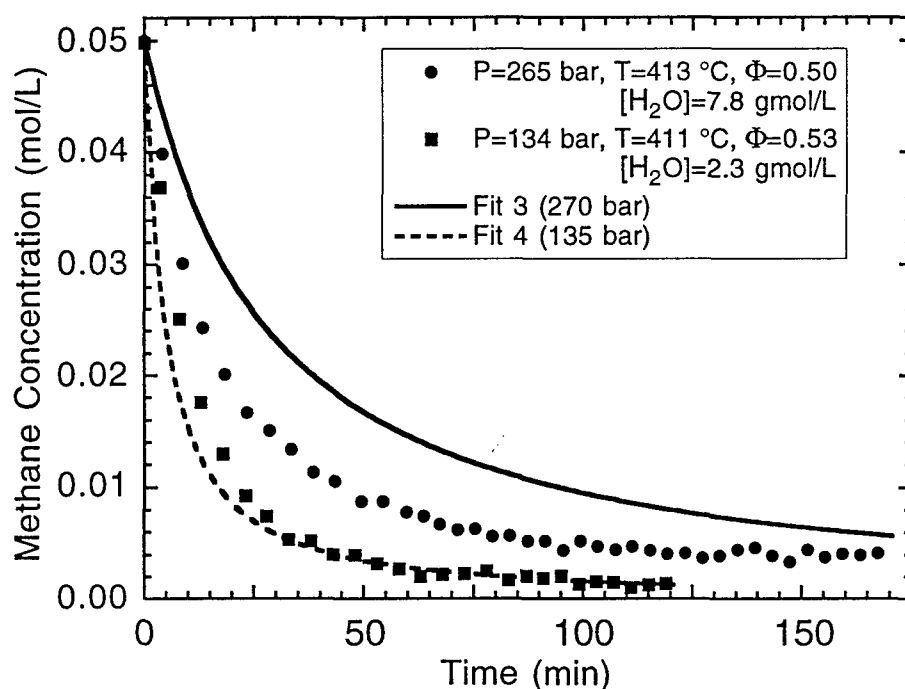


Figure 4.15. Comparison of observed and predicted methane concentrations at two pressures and similar initial conditions. Experiments #09014 and #09284.

The second group of experiments listed in Table 4.4 extends the pressure range of measurements made at  $T \sim 412^\circ\text{C}$  and permits the comparison of reaction rates over a wide range of water densities. To compare all the experimental data at this temperature, a characteristic time is defined as the time required for an initial concentration of 0.05 gmol/L of methane to be reduced to  $1/e$  of the original amount. All data at concentrations greater than 0.05 gmol/L are ignored, eliminating all points from the settling period of each experiment. The remaining points are fit with an interpolating curve, and the  $1/e$  time is

determined for each experiment. Inverting the characteristic times yields apparent first-order rate constants, plotted in Figure 4.16 as a function of water number density. Density of the buffer (water or argon) is calculated using the NBS/NRC empirical equation of state for water (Haar, *et al.*, 1984), with the Peng-Robinson equation of state (Peng and Robinson, 1976) used for the combustion gases; mixing is assumed to be ideal.

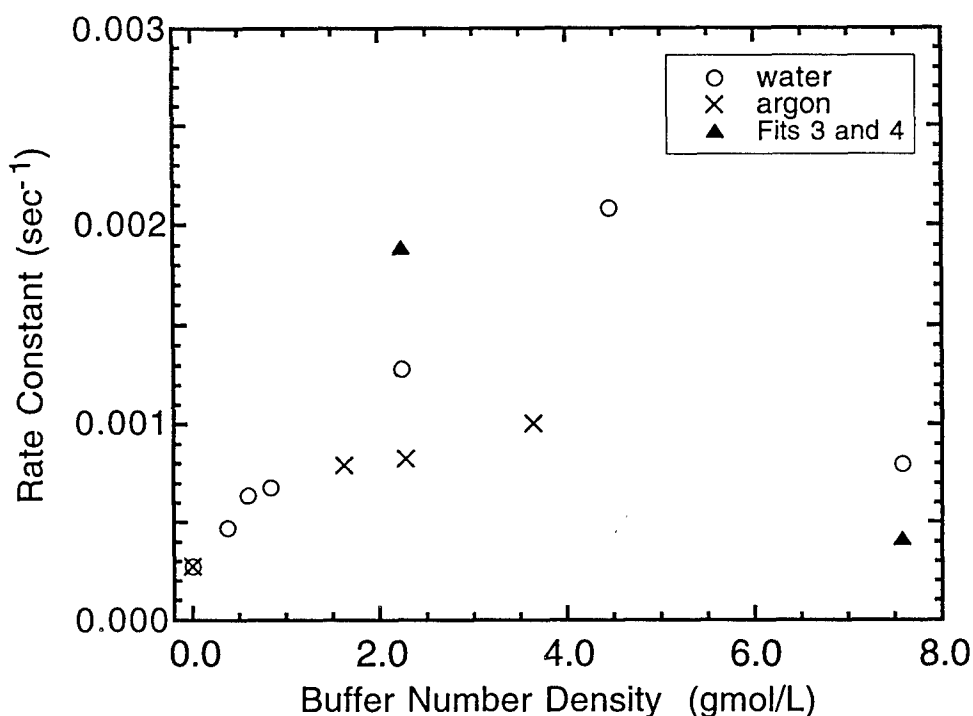


Figure 4.16. Comparison of methane oxidation rate constants as a function of buffer number density. Results are shown for both water and argon as buffer. Initial  $[\text{CH}_4] = 0.05 \text{ gmol/L}$ ,  $T \sim 412^\circ\text{C}$ , lean mixtures.

The circles in Figure 4.16 indicate the trend of rate constants as water density is increased from zero to values typical of SCWO. Initially, rates rise with pressure as water content is increased. However, at a pressure over 200 bar ( $[\text{H}_2\text{O}] \sim 4.5 \text{ gmol/L}$ ), the trend is reversed and the rate drops significantly as pressure is increased to 270 bar ( $[\text{H}_2\text{O}] \sim 7.5 \text{ gmol/L}$ ). In future work, this graph will be filled in with additional experimental data. However, it should be emphasized that the trends indicated in Figure 4.16 are supported by the ensemble of all the experiments performed at 135 and 270 bar. The two solid symbols in Figure 4.16 represent apparent first order rate constants predicted

using Fit 4 for the low density point, and Fit 3 for the high density point. These fits represent more than 800 concentration versus time measurements, each of which constitutes a separate rate measurement. The two are thus potent data points, and they agree with the trend of the rest of the data in Figure 4.16.

Also included in Figure 4.16 are rates for the argon experiments. At zero water density, the argon and water points coincide since the reacting mixture at these conditions contains fuel and oxidizer only, with no buffer present. Note that the highest density point for argon and the highest density point for water represent the same experimental pressure; densities are higher in water due to its low compressibility (at 200 bar and 410 °C,  $Z_{\text{water}} \sim 0.67$  while  $Z_{\text{argon}} \sim 1.06$ ). The graph shows that argon rate constants rise steadily with density over the range examined. Examining the data below 2 gmol/L, the increase in rates with density appears similar for water and argon. At densities of 4 gmol/L, however, the increase in water's rate is significantly greater than argon's. Future argon experiments in a reactor with a higher pressure rating are required to determine if there is an eventual density-dependent downturn in rates.

The downturn in rates with increasing water density was unexpected, based on the few previous studies of pressure dependence in supercritical water that have been published. Although no previous variable pressure studies of methane exist, the rate of conversion of phenol was found to increase steadily over a wide range of water densities from 6 to 28.6 gmol/L (Thornton and Savage, 1992). To correlate their data, they included a concentration term and reaction order for water ( $[\text{H}_2\text{O}]^{0.7}$ ) in their global reaction expression. Including such a term in the global fit of our data is not feasible since it would be unable to correlate our non-monotonic results. In another study, constant fuel concentration experiments were conducted using hydrogen and carbon monoxide (Holgate and Tester, 1994a). Rate constants for both fuels steadily increased over the density range of 1.8 - 4.6 gmol/L. Note however that this range does not include densities where our rate constants reverse in trend.

In addition, the literature contains studies of the effect of pressure on rates in *non-aqueous* supercritical fluids that offer some insights. Brennecke (1993) reviews such studies, outlining the factors that affect reaction rates in supercritical fluids, including pressure, diffusion, and local concentration. In the discussion of pressure effects, the influence of potentially large activation volumes is emphasized. From transition state theory, activation volumes

determine the pressure dependence of reaction rate coefficients through the expression:

$$RT \frac{\partial \ln k}{\partial P} = -\Delta V^\ddagger - RTk_T$$

where  $k$  is the concentration-based rate coefficient,  $\Delta V^\ddagger$  is the activation volume, and  $k_T$  is the isothermal compressibility. Calculation of the activation volume requires knowledge of the partial molar volume of the transition state, a quantity seldom known. Brennecke notes that activation volumes for supercritical fluids are often negative, which implies *increasing* rates with pressure. Of course, an elementary reaction could accelerate by this mechanism and still contribute to our observed drop in global rate if it were a back-reaction that slowed the consumption of fuel.

The many influences of supercritical water on oxidation reactions suggest explanations for our pressure-dependent rates. However, such theories are best discussed in terms of detailed reaction mechanisms rather than global mechanisms, as presented in the next chapter.

#### **4.6. Conclusions**

Our kinetics experiments produced data that characterize the oxidation rate of methane in water at conditions close to those of commercially designed SCWO processes. The experiments performed in an optically accessible reaction cell demonstrated the utility of Raman spectroscopic methods of determining *in situ* concentrations of major combustion gases in supercritical water environments. These experiments at relatively high fuel concentrations and long residence times complement prior measurements made in flow reactors with low concentrations and short residence times. Our measurements were subject to uncertainties due to reactor communication with external, unheated volume and due to finite mixing times.

The fit of our 270-bar data to a global reaction rate expression indicates significant deviation from prior published results. At our conditions, the derived activation energy is nearly twice the previously published value for low-concentration data. The reaction order with respect to methane for our data is close to 2, while earlier results have mostly found values of unity for methane

and other simple fuels. These differences are attributed to the higher range of fuel and water concentrations examined in the present experiments.

Experiments conducted over a wide range of water densities at constant initial fuel concentration, equivalence ratio, and temperature revealed an unexpected reversal in the influence of pressure on reaction rate. At pressures above the water's critical pressure, the reaction rate constant for methane decreased with increasing pressure. Experiments with argon substituted for water showed no such trend although results covered a reduced range of densities.

## 5. Model Assessments

This chapter compares our experimental data with predictions from models of supercritical water oxidation chemistry. Several computational tools are currently under development that have been specifically designed to handle the high-density, aqueous environment of SCWO. Coming from various research institutions, these tools include elementary reaction mechanisms, equations of state, and computer subroutine packages. In this chapter, a current selection of tools are used to model both our kinetics and flame ignition data. The objective is to report on the predictive capabilities of existing models. The modification of these tools to improve their performance is beyond the scope of this study, although information is highlighted that will guide the further development of SCWO models.

### 5.1. Kinetics Models

Several elementary reaction mechanisms designed for SCWO have been published. The starting point chosen for these efforts has been the validated mechanisms that exist for gas-phase oxidation of simple hydrocarbons (Warnatz, 1984; Norton and Dryer, 1989; Wilk, *et al.*, 1989; Yetter and Dryer, 1991). In applying these mechanisms to supercritical water environments, a hypothesis is made that reactions are dominated by gas-phase, free radical chemistry rather than the ionic chemistry of liquids (Holgate and Tester, 1993). This hypothesis is supported by examining several properties of supercritical water at typical process conditions: the ionic dissociation constant of water is about  $10^{-20}$ , or six orders of magnitude lower than liquid water (Marshall and Franck, 1981); the dielectric constant, a measure of molecular association, is an order of magnitude lower than liquid water (Uematsu and Franck, 1980); and SCWO transport coefficients resemble gas-phase more than liquid-phase properties (Lamb, *et al.*, 1981). Further support of the hypothesis comes from experimental evidence of free-radical reactions in SCWO reactions (Antal, *et al.*, 1987), as well as from past successes in applying models based on the hypothesis (Holgate, 1993).

Efforts to adapt elementary reaction models to SCWO were begun by researchers at MIT. They began by testing an atmospheric-pressure  $H_2$ -CO mechanism, using non-unity compressibilities to modify rates via the equilibrium constants (Helling and Tester, 1987). This was followed with a

model for methane and methanol in which rate coefficients of some unimolecular reactions were adjusted to their high-pressure limits and the collisional efficiency of water was included (Webley, 1989). This model predicted their experimental oxidation data well in the case of methanol, but underpredicted conversion of methane by a factor of four. Butler and colleagues (Butler, *et al.*, 1991; Schmitt, *et al.*, 1991) performed a similar analysis using data from experiments performed at Sandia (Bramlette, *et al.*, 1990). More recently, Holgate has reformulated Helling's carbon monoxide and hydrogen mechanism and demonstrated success in predicting experimental data (Holgate and Tester, 1994a; Holgate and Tester, 1994b). This work has been recently incorporated into a new mechanism for methane and methanol oxidation developed by Pitz and collaborators (Alkam, *et al.*, 1995).

The Pitz mechanism is tested in this chapter against our experimental results. Most experimental data available to date for comparison with reaction models are based on hydrocarbon concentrations well below typical SCWO feed concentrations. As a result, comparison to our data provides a first opportunity to assess the models at elevated, process-like fuel concentrations.

## **5.2. Methane Model**

The Pitz mechanism combines Holgate's H<sub>2</sub>-CO mechanism (Holgate and Tester, 1994b) with the Norton-Dryer ethanol mechanism (Norton and Dryer, 1992) and the Pitz-Westbrook C<sub>2</sub> mechanism (Pitz, *et al.*, 1991). Pitz made minor changes when assembling these sub-mechanisms (Alkam, *et al.*, 1995). In his kinetics study, Holgate chose a low value of heat of formation for HO<sub>2</sub> (within the range of published values) in order to best match his experimental data (Holgate, 1993). Pitz specified a higher value for the HO<sub>2</sub> heat of formation, but then altered the rates of two reactions in Holgate's mechanism within their uncertainties (Reactions 12 and 13 in Section 7.1) in order to maintain good agreement with the Holgate experimental data (Pitz, 1995). In addition, the rates of several decomposition reactions from the Norton-Dryer and Pitz-Westbrook mechanisms were modified to their high-pressure limits (Alkam, *et al.*, 1995). The authors chose to write explicitly, as forward and reverse pairs, all reactions not in the H<sub>2</sub>-CO sub-mechanism. To determine reverse rate parameters, they used the Chemkin thermodynamic data base (Kee, *et al.*, 1990) with a single exception noted in their report (Alkam, *et al.*, 1995). The Pitz mechanism

predicted reasonably well the data from Webley's methanol and Holgate's hydrogen experiments, although in extrapolations to longer times, the Pitz model deviated strongly from Holgate's global rate expression for hydrogen.

For the current modeling effort, the Pitz mechanism with all C<sub>2</sub> species removed has been adopted (referred to below as the Pitz-C1 mechanism). Our initial tests showed that inclusion of C<sub>2</sub> chemistry has no noticeable effect on major species profiles—evidence that a low concentration of methyl radicals and an abundance of water molecules in our environment inhibits formation of C<sub>2</sub> species. The 21 species and 147 reactions used in the Pitz-C1 mechanism are listed in the Appendix, Section 7.1.

To simulate our kinetics experiments, an isobaric, isothermal, plug-flow reactor model was chosen. Although the experiments were actually performed in a constant volume reactor, this model approximates the experimental conditions and is more convenient. The experimental data indicate that pressure and temperature varied over only a small range, especially in the case of the abridged data sets discussed in Chapter 4. The driver program for our model uses Chemkin (Kee, *et al.*, 1991) and Chemkin Real Gas (Schmitt, *et al.*, 1993) subroutine packages to solve the single (mass) conservation equation. Thermodynamic information is taken from the data bases associated with both packages. Because of our interest in the effects of water density, subroutines have been added to the driver program to more accurately calculate water concentration. The Peng-Robinson equation of state (Peng and Robinson, 1976) available in Chemkin Real Gas does a poor job of estimating water concentration at the lowest experimental temperatures, so it is used only for non-aqueous species. Water densities are handled with the empirical NBS/NRC equation of state (Haar, *et al.*, 1984).

The principle of mass action for the reaction  $aA + bB \rightarrow cC + dD$ ,

$$\text{rate} = k_f [A]^a [B]^b, \quad 5.1$$

is often applied in non-ideal systems, but several difficulties must be addressed. The proper form of the equation derived from transition state theory for reactions in solution is (Levine, 1995):

$$\text{rate} = k_f^\infty \frac{\gamma_A^a \gamma_B^b}{\gamma_*} [A]^a [B]^b, \quad 5.2$$



where  $k_f^\infty$  is the rate coefficient at infinite dilution,  $\gamma_A$  and  $\gamma_B$  are the concentration-scale activity coefficients of the reactants, and  $\gamma_*$  is the activity coefficient of the transition state complex. Thus the correct apparent rate coefficient  $k_f$  for Equation 5.1,

$$k_f = k_f^\infty \frac{\gamma_A^a \gamma_B^b}{\gamma_*}, \quad 5.3$$

is a function of temperature as well as composition and pressure (through the activity coefficients). In practice, particularly in dilute systems, the effect of changing composition on rates is minor, and the quotient in Equation 5.3 is approximated as a constant. The term  $k_f^\infty$  is the rate coefficient that applies in the limit as  $[A]$  and  $[B]$  go to zero, and is dependent on the identity of the solvent as well as temperature. This derivation for liquid solutions is also valid for nonideal-gas reactions, with fugacity coefficients replacing activity coefficients.

Prior SCWO modeling efforts have addressed some of these issues. For example, the Chemkin Real Gas package (Schmitt, *et al.*, 1993) provides subroutines to calculate equilibrium constants for real-gas mixtures. In these subroutines, the equation describing chemical equilibrium contains both fugacity coefficients and compressibilities:

$$K_{eq} = K_c K_\phi (ZRT/P_0)^{\sum v} \quad 5.4$$

where  $K_{eq}$  is the equilibrium constant,  $K_c$  is the product of concentrations raised to the power  $v$ ,  $K_\phi$  is the product of fugacity coefficients raised to the power  $v$ ,  $Z$  is the mixture compressibility, and  $v$  are the stoichiometric coefficients ( $a$ ,  $b$ ,  $-c$ , and  $-d$ ). If the forward rate coefficients,  $k_f$ , provided by the elementary reaction mechanism are correct, reverse rate coefficients can be calculated using the corrected equilibrium constant:

$$k_r = \frac{k_f}{K_{eq}}. \quad 5.5$$

Unfortunately, the  $k_f$  available to use in Equation 5.5 normally don't include the corrections of Equation 5.3 which could become significant in dense supercritical water. In the past, forward rate coefficients used in SCWO models have been gas-phase values. Select unimolecular reaction rate coefficients have been adjusted to their high-pressure limits, but they have not been adjusted to

account for any water-reactant interactions (i. e., they are not  $k_f^\infty$ ), nor do they account for non-unity fugacity coefficients. As a simplification in previous studies, fugacity coefficients have been assumed equal to 1, justified by the relatively high temperatures and low densities involved (Webley and Tester, 1991; Holgate and Tester, 1993; Alkam, *et al.*, 1995). This assumption conveniently eliminates all of the real-gas correction factors except for  $k_f^\infty$  in Equation 5.2 and  $Z$  in Equation 5.4. Although our kinetics experiments were conducted at higher densities than previous work, fugacity coefficients are assumed equal to 1 for the current modeling as well. The decision is based on (1) a current inability to accurately calculate fugacity coefficients, particularly for radical species and transition state complexes; (2) relatively large uncertainties that exist in forward rate coefficient data for SCWO; and (3) the fact that this assumption has already been incorporated in all the reverse reactions that are written in explicit form in the Pitz mechanism.

### **5.3. Rate Prediction**

The performance of the current model at conditions of one of the methane experiments is assessed in Figures 5.1 and 5.2. Comparing the time scales of the two figures, it is evident that the elementary mechanism dramatically overpredicts reaction rates at these conditions. The time required to consume the methane in the experiment is approximately six times longer than in the model. Comparing concentration profiles is of limited value given the disparity in rates, but if time were non-dimensionalized by a characteristic destruction time, the profiles of  $\text{CH}_4$ ,  $\text{O}_2$ , and  $\text{CO}_2$  would be similar. In contrast, the profiles of  $\text{CO}$  concentration appear different. The difference can be seen if one compares the  $\text{CO}$  profiles at the time that  $\text{CH}_4$  concentration is equal to  $\text{CO}_2$  concentration on the two graphs. At this time in Figure 5.2, predicted  $\text{CO}$  concentration is at its maximum of 0.5 gmol/L. At this time in Figure 5.1, however, either the maximum  $\text{CO}$  concentration is smaller than the predicted value, or the concentration is already falling and the maximum occurred earlier in time.

Figure 5.3 presents a second comparison of model predictions with methane oxidation data from the Webley experiments (Webley and Tester, 1991) and from the current experiments. In the upper left of Figure 5.3, the solid symbols are Webley's data reduced assuming first-order kinetics (the term *first-order* here

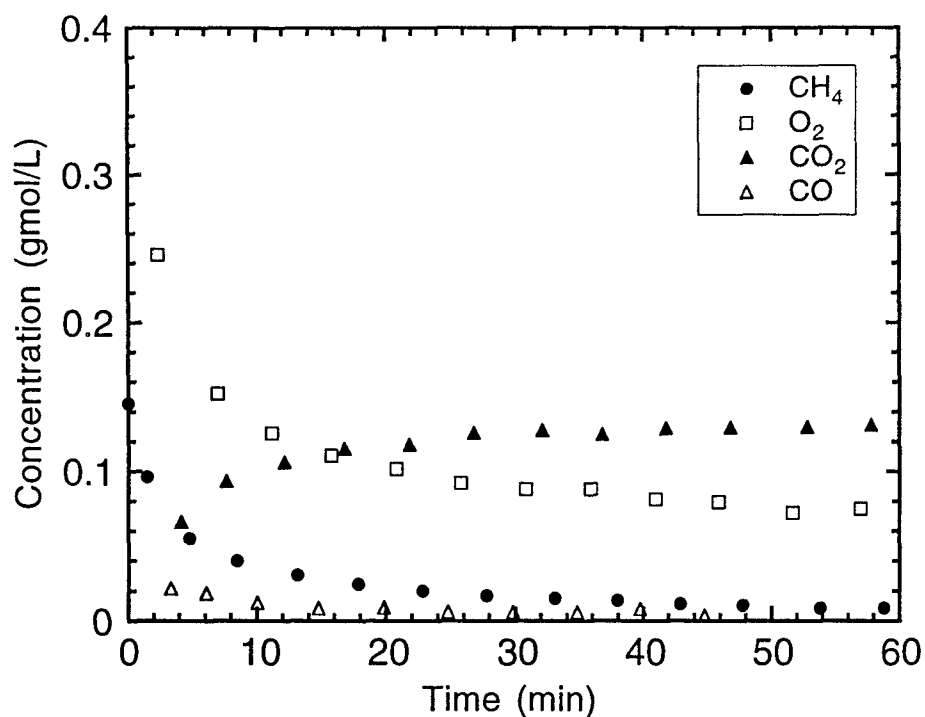


Figure 5.1. Experimental measurements of the oxidation of methane at  $T = 413\text{ }^{\circ}\text{C}$  and  $P = 265\text{ bar}$ . Experiment #09014.

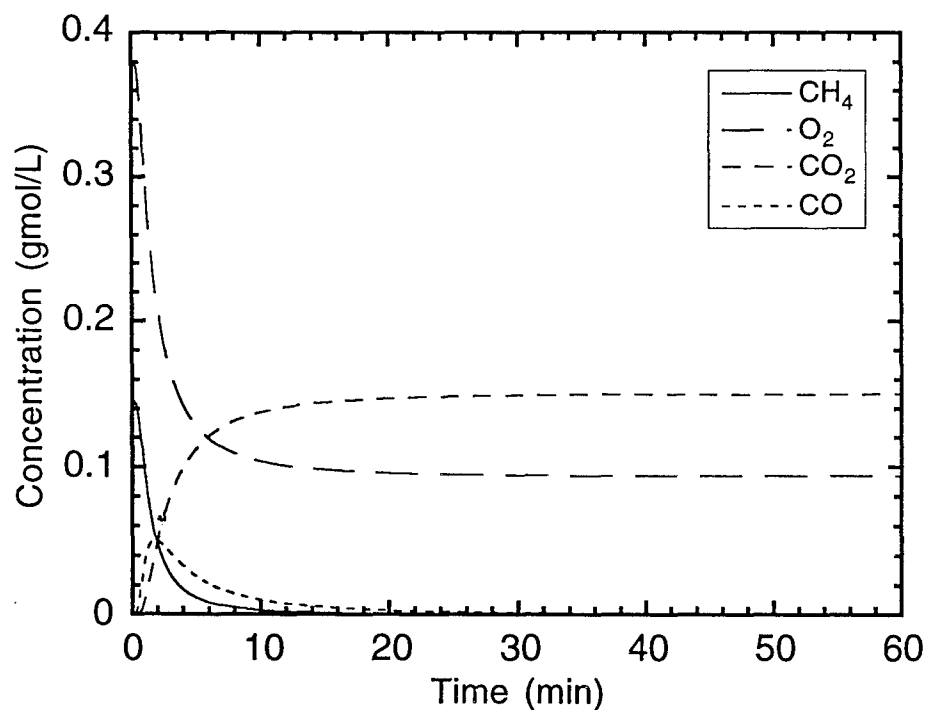


Figure 5.2. Model prediction of concentration histories for the conditions of Figure 5.1.

implies first-order in methane concentration and zeroth-order in oxygen). The line through the data is their reported best-fit, first-order rate equation. The *cross* symbols located above their data are predictions of the Pitz-C1 model obtained by integration to the experimental final methane concentrations. The model overpredicts the observed rates by a factor of  $e$ , but accurately captures the activation energy (slope) of the data. It should be pointed out that the Pitz-C1 model shows significant improvement over the original attempt to model this data (Webley and Tester, 1991).

The current methane data is represented by solid symbols in the lower right of Figure 5.3. Manipulating the data to extract a first-order rate coefficient is difficult since the observed methane reaction order deviates significantly from unity (see Section 4.2.5). One way to proceed is to remove initial methane and oxygen concentrations as variables in the comparison. This is done by approximating the observed data using Fit 3 of Section 4.2.5, while holding initial concentrations constant. Accuracy of the fit is sufficient for the purposes of this comparison. Apparent first-order rate coefficients are obtained by integrating the Fit 3 rate expression to a time at which methane concentration has dropped to  $1/e$  of its original value. Note that the choice of integration time and initial concentrations affects the calculated rate coefficients due to the non-first-order kinetics of the data. However, these factors do not shift the model and fit values relative to each other, only relative to the Webley data.

In our 270-bar methane experiments, initial concentrations were significantly higher, and temperatures were significantly lower than in the Webley experiments. At our conditions, Figure 5.3 shows that the Pitz-C1 model overpredicts rates by a factor of 20 and exhibits a reduced temperature dependence. In contrast, the model performs better at 137 bar, as shown in Figure 5.4. In this figure, points representing the experimental data (solid symbols) are approximated by integrating Fit 4 of Section 4.3.4. At this pressure, the model predictions (crosses) are much closer to the experimental data, especially at higher temperatures. The fact that model predictions worsen with increasing density is tied to the observed downturn in overall rates over the same density range (see Section 4.5). Identifying the reactions responsible for the downturn will enable the model to better predict both the trend and actual values of the observed rate coefficients. Section 5.4 addresses further the issue of density-dependent rates.

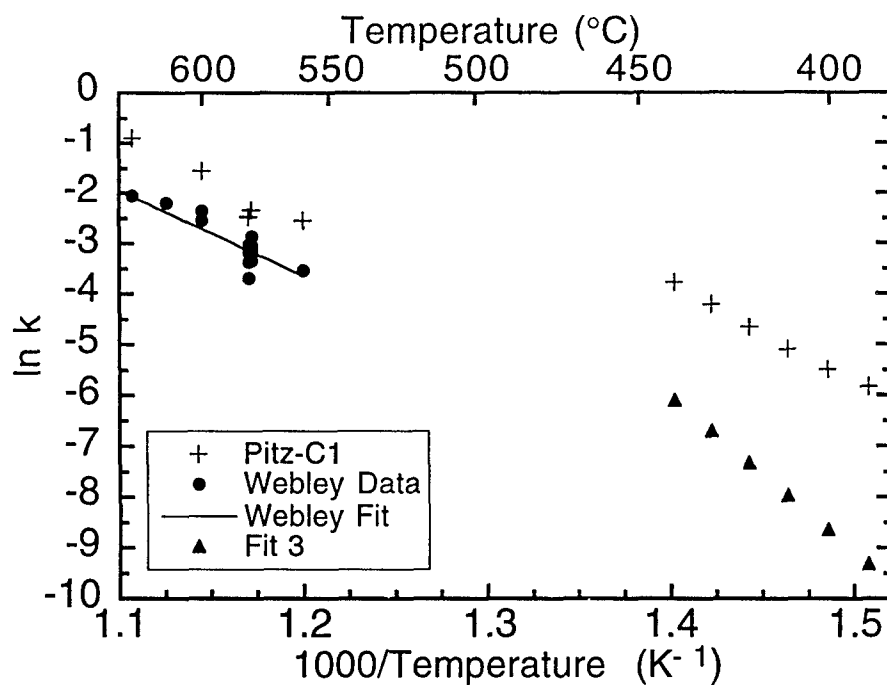


Figure 5.3. Experimental and predicted apparent first-order rate coefficients for Webley's data at 246 bar and the current data at 270 bar. (Current data is approximated by Fit 3.) For the Pitz-C1 and Fit 3 points,  $[\text{CH}_4]_{\text{initial}} = 0.05 \text{ gmol/L}$ ,  $[\text{O}_2]_{\text{initial}} = 0.15 \text{ gmol/L}$ .

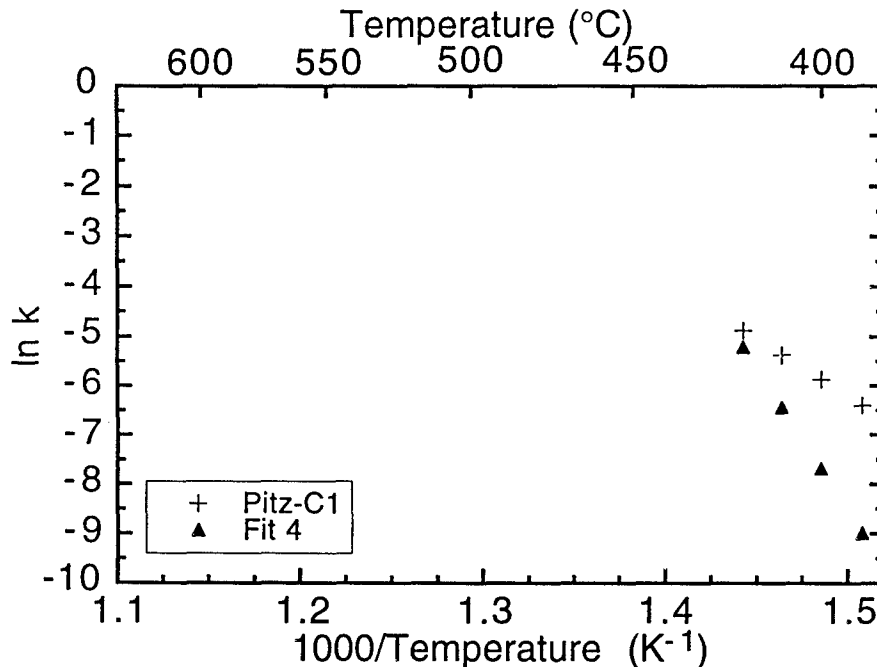


Figure 5.4. Current data (approximated by Fit 4) and Pitz-C1 model predictions for the 135-bar experiments. Initial concentrations are as in Figure 5.3.

Some of the disagreement between the Pitz-C1 model and current data in Figures 5.3 and 5.4 may be attributable to the fact that the developers of the various mechanisms were guided by the goal of fitting Webley and Holgate's low-concentration data. For example, in the  $\text{H}_2\text{-CO}$  sub-mechanism, uncertainties in the rate coefficient for the primary oxidizing reaction,  $\text{CO} + \text{OH} \rightarrow \text{CO}_2 + \text{H}$ , lead to predicted rates that vary by a factor of two (Holgate, 1993). The faster rate giving better agreement with experimental data was incorporated by Holgate. Again in the case of heat of formation of the hydroperoxyl radical, published data encompass a range of values from 0.5 to 3.0 kcal/gmol. Holgate chose the minimum value, dropping hydrogen consumption rates by a factor of eight over the maximum value (Holgate, 1993). Pitz used a possibly more acceptable value of  $\Delta H_f = 2.9$  kcal/gmol (Alkam, *et al.*, 1995), and then achieved agreement with observed data by shifting two elementary reaction rates (Pitz, 1995). This legitimate tuning of the mechanism, if performed for our data, could reduce model disagreement, but likely at the cost of disagreement with Webley and Holgate data.

Transport properties have not been included in the current model, and the issue of diffusion-limited reaction rates should be considered as a possible explanation for its poor performance. The most likely reactions to be affected by diffusion control are fast recombinations. To test this possibility, the recombination reaction of  $\text{H} + \text{O}_2$  to form  $\text{HO}_2$  was selected since it is an important forward path in the Holgate (and Pitz-C1) mechanism (Holgate, 1993). This reaction (Reaction 7 in Section 7.1) proceeds with a negligibly small activation energy. The high-pressure limit, appropriate for our conditions, has a preexponential factor of  $4.79 \times 10^{13}$  gmol  $\text{cm}^{-3}$   $\text{s}^{-1}$ . This value can be used as the reaction rate coefficient,  $k_{rxn}$  in the following comparison. Following the method outlined by Schroeder and Troe (1987), a diffusion rate constant,  $k_{diff}$ , can be calculated to compare with the reaction rate coefficient:

$$k_{diff} = 4\pi N_A R D,$$

where  $N_A$  is Avogadro's number,  $D$  is a diffusion coefficient, and  $R$  is an encounter distance estimated using Lennard-Jones diameters  $\sigma_A$  and  $\sigma_B$ :

$$R \approx \sqrt{2}(\sigma_A + \sigma_B)/2.$$

For the reactants diffusing toward each other,  $D$  is estimated as twice the experimentally measured self-diffusion coefficient of water ( $2 \times 1.5 \times 10^{-3} \text{ cm}^2 \text{ s}^{-1}$ ) (Lamb, *et al.*, 1981). The Leonard-Jones diameters of hydrogen and oxygen are approximated as 2.92 and 3.54 Å. The resulting estimate for  $k_{diff}$  is  $1 \times 10^{15} \text{ cm}^3 \text{ gmol}^{-1} \text{ s}^{-1}$ . Since  $k_{diff}$  is more than an order of magnitude faster than  $k_{rxn}$ , this recombination is not likely to be diffusion-limited at our conditions. The faster recombination,  $\text{H} + \text{OH} + \text{M} \rightarrow \text{H}_2\text{O} + \text{M}$ , may become diffusion-controlled—however, it is not among the dominant reactions identified in the Holgate study (Holgate, 1993). No other important forward reaction was identified as a potentially diffusion-limited step.

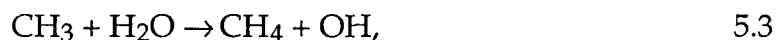
A final explanation for model discrepancies at our conditions is that chemical pathways may actually shift with changes in temperature and concentration. The maximum water density in our experiments is a factor of three higher than in Webley and Holgate's experiments. Chemical pathways that are not important at moderate densities and that may be missing from the Pitz mechanism could be necessary to predict rates at elevated densities. The current results point to the need for further modifications of elementary mechanisms in order to achieve better agreement over the full range of available experimental observations.

#### **5.4. Density Dependence**

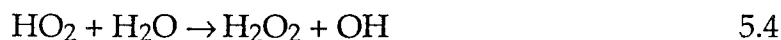
Previous modeling work has identified dominant pathways in methane oxidation. At the temperatures of SCWO, attack on  $\text{CH}_4$  is dominated by OH radicals through the reaction (Webley and Tester, 1991):



Webley noted that the reverse of Reaction 5.2 is important as well:



since 90% of the methyl radicals formed in his model were consumed in back-reaction with water. The dominant chain branching path consists of the reaction (Holgate, 1993):



coupled with



Holgate determined that the hydrogen peroxide dissociation, Reaction 5.5, is near its high-pressure limit at 246 bar, and in its fall-off regime below that pressure.

Through the explicit participation of water in Reactions 5.3 and 5.4, and through its participation as a collision partner in the unimolecular Reaction 5.5, changing water number density can be expected to affect the overall consumption of methane. Based on Reactions 5.3, 5.4, and 5.5, one can construct a trial hypothesis to explain the observed decline in reaction rates with water density. For this discussion, the observed variation of rate coefficient with water number density (Figure 4.16) is reproduced as Figure 5.5.

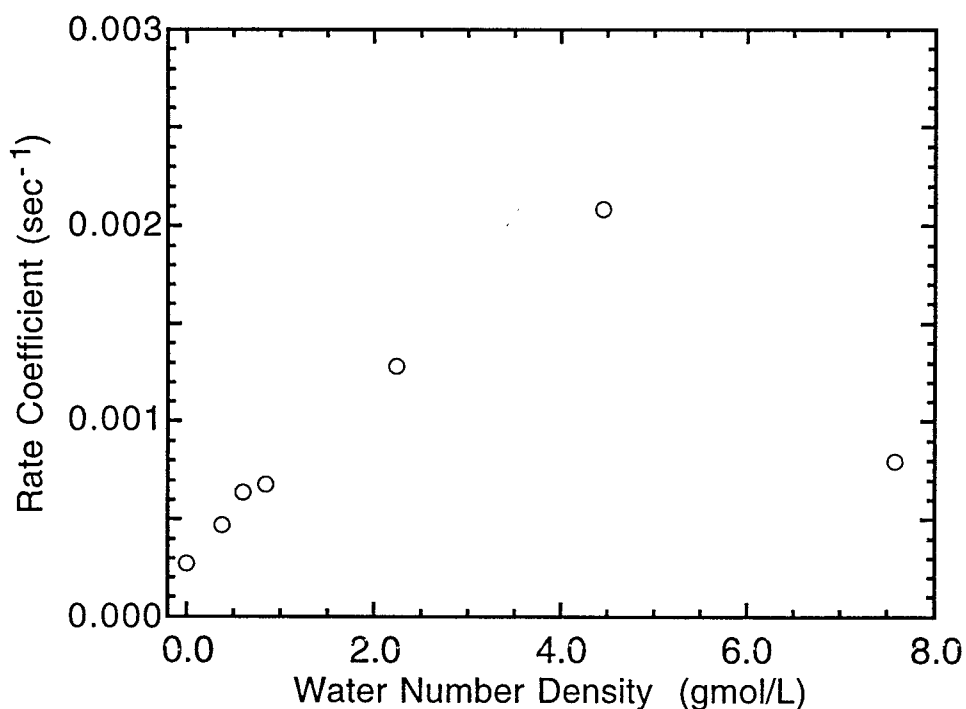


Figure 5.5. The variation of observed first-order rate coefficients with water number density at  $T = 412^\circ\text{C}$  and  $[\text{CH}_4]_{\text{initial}} = 0.05$  gmol/L (from Figure 4.16).

The hypothesis explains the data of Figure 5.5 in the following way. At water densities below 4 gmol/L, rate coefficients for Reactions 5.3, 5.4, and 5.5 increase with density. The rate increase in Reactions 5.4 and 5.5 increases



methane consumption through the production of hydroxyl radicals. The rate increase in Reaction 5.3 retards methane consumption. At low densities, Reactions 5.4 and 5.5 dominate, and the overall methane consumption rate climbs with density. Since the rates of Reactions 5.3, 5.4, and 5.5 all increase linearly with water density, the domination of 5.4 and 5.5 is unchanged as density rises.

If, however, as Holgate suggests, the decomposition of hydrogen peroxide reaches its high-pressure limit in the vicinity of 4 gmol/L, the rate coefficient of Reaction 5.5 freezes at that point. Then (depending on the relative rates of the pair of Reactions 5.4 and 5.5) the chain-branching path could become insensitive to further increases in water density. Reaction 5.3 on the other hand hits no such high-pressure limit since water's role in the reaction is as a reactant, not as an inert collision partner. As concentration rises above 4 gmol/L, the rate coefficient of Reaction 5.3 continues to rise. As it increases relative to the chain-branching pair, the effect is to slow the increase in overall methane consumption rate. Given a large enough change in water concentration, the overall rate could drop as in Figure 5.5.

To test the hypothesis, rates of methane consumption predicted by the Pitz-C1 mechanism can be compared as a function of water number density. Since the model was shown to overpredict rates in Section 5.3, the goal here is to examine rate *trends* rather than actual values. As in Chapter 4, the time required to destroy  $1/e$  of the initial methane is used to determine an apparent first order rate coefficient for each simulation. The solid symbols in Figure 5.6 represent predictions of the Pitz-C1 mechanism at conditions matching those of Figure 5.5. At water densities matching our experimental data, 0 - 8 gmol/L, the model predicts a constant increase in rates. At higher densities however, the model shows the same downturn observed in the experiments. The model misses the characteristic density at which the rate reaches a maximum, but produces the same abrupt reversal as in our experimental observations.

Taking this result as support of our hypothesis and taking the next logical step, rates of key elementary reaction steps in the Pitz-C1 mechanism were modified in an attempt improve predictions. Of the elementary Reactions 5.3 - 5.5, the density dependence of the overall rates proved most sensitive to Reaction 5.3. The open symbols in Figure 5.6 were produced by increasing the rate of Reaction 5.3 by a factor of 600. (The rate of Reaction 5.2 was unchanged.) The effect is to lower the density at which the maximum rate occurs. With this

modification, the model is able to predict a downturn in overall rates near the characteristic density observed in our experiments.

The results presented in Figure 5.6 suggest that current detailed mechanisms may already contain the reactions necessary to explain the pressure dependence of overall reaction rates at high water densities. Future work will include a sensitivity and flux analysis of the Pitz-C1 mechanism. The simplified hypothesis presented above was based on reported sensitivity results for conditions significantly different from the current work. A sensitivity analysis will uncover all elementary reactions that play an enhanced role at high water densities, and is necessary for a complete understanding of reaction rates at supercritical water conditions.

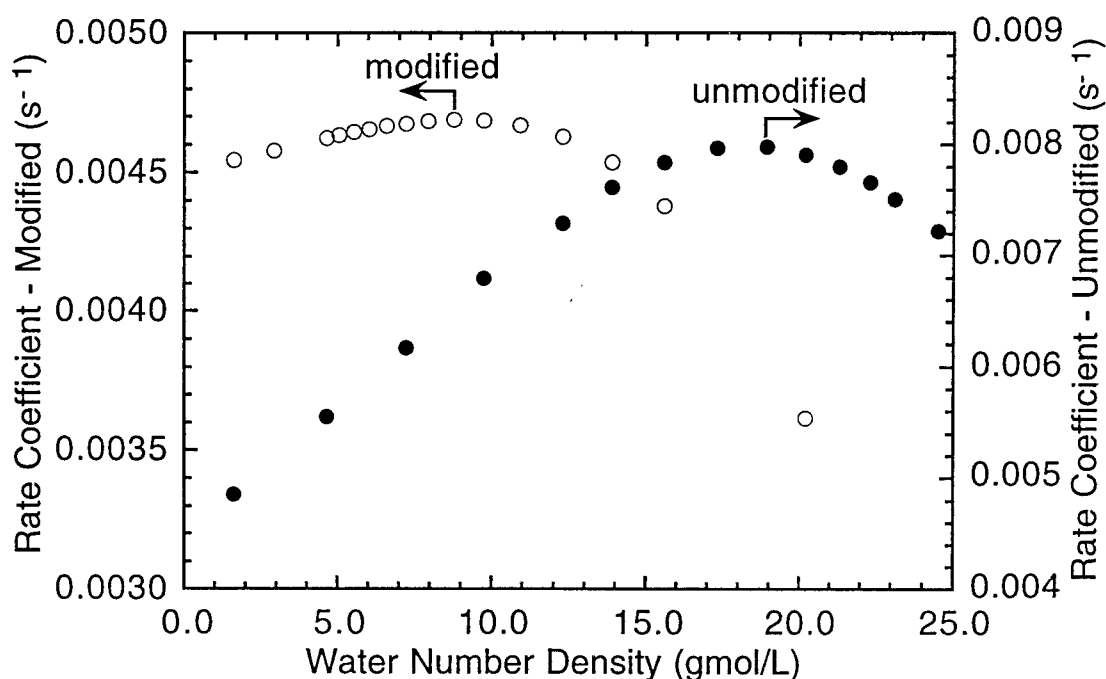


Figure 5.6. Model predictions of apparent first order rate coefficients for methane consumption as a function of water number density.  $T = 412\text{ }^{\circ}\text{C}$ ,  $[\text{CH}_4]_{\text{initial}} = 0.05\text{ gmol/L}$ ,  $[\text{O}_2]_{\text{initial}} = 0.30\text{ gmol/L}$ . The preexponential factor for Reaction 5.3 was multiplied by 600 in the modified model.

## 5.5. Flame Ignition Prediction

The flame ignition data of Chapter 3 provide another opportunity to compare experimental observations with model predictions. The model as described above is inappropriate for this task for at least two reasons: first, it includes no energy equation, and second, the poor performance of the Pitz-C1 in predicting rates at high densities suggests it would fail, as well, in predicting ignition at these same conditions. This section describes modifications made to the model in an attempt to predict the ignition of flames in our supercritical water reactor.

To specify reaction rates in the ignition model, the one-step mechanism determined by Fit 3 replaced the Pitz-C1 elementary reaction mechanism. Mulholland *et al.* (1992) have demonstrated that global chemistry mechanisms can successfully be used to model auto-ignition of simple hydrocarbons. They were able to derive single- and multi-step global mechanisms that adequately represented the weakly reacting regime leading up to ignition of methane in air at atmospheric pressure. The global fit to our 270-bar data should perform a similar function for current experimental conditions.

Furthermore, Mulholland determined that prediction of ignition was, to a first approximation, independent of reactor environment (Mulholland, *et al.*, 1992b; Mulholland, *et al.*, 1992a). Their models of a perfectly stirred reactor and a plug-flow reactor *both* matched trends in published ignition data for a series of hydrocarbons, in spite of entirely different fluid mechanics. For our flame experiments, an isobaric, adiabatic, plug-flow reactor model has been chosen based on the following heuristic scenario. To simplify the flow, one can imagine a jet of oxygen vertically traversing the reactor and exiting the top port. The water-fuel mixture is entrained by the oxygen jet until separating from the jet at the exit port and recirculating. In this simplification, ignition is determined by comparing the flow time to traverse the reactor with the chemical kinetics time specified by the global reaction mechanism. Radial mixing by diffusion is assumed fast enough to be ignored, and heat transfer losses from the central flow of fluid are neglected.

For our ignition model, the energy equation has been added to the model of Section 5.4, and temperature is tracked along with methane and oxygen concentrations as a function of time. As discussed by Mulholland (1992b), ignition can be estimated by the inflection point in the temperature versus time

curve. Figure 5.7 shows the temperature history predicted by the current model for a given initial temperature and initial reactant concentrations. The maximum slope of the temperature curve defines a critical time that is taken as the predicted time of ignition.

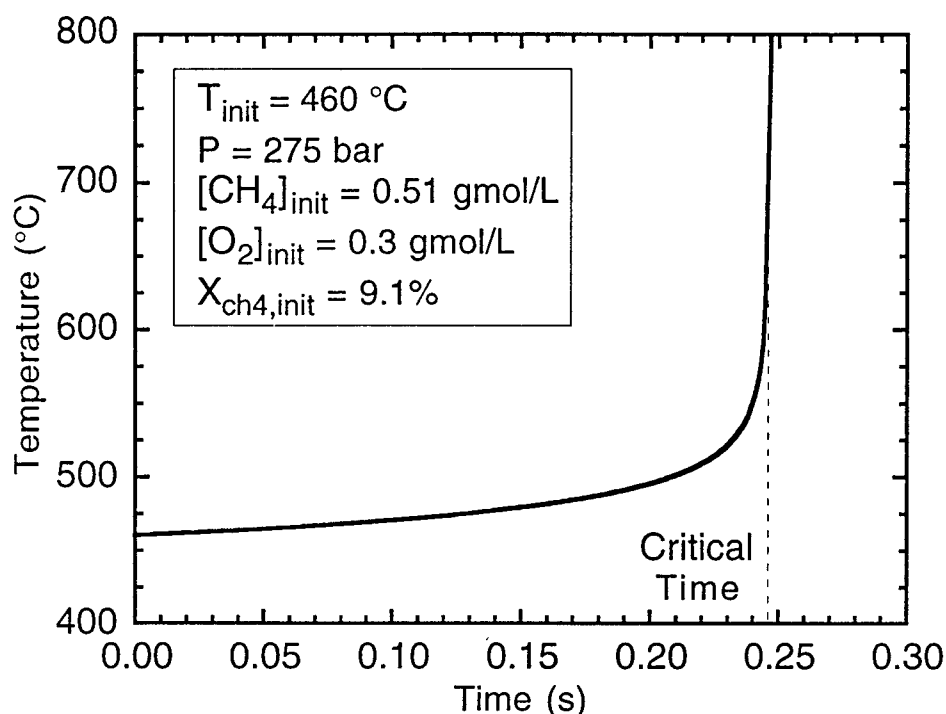


Figure 5.7. Predicted temperature history for the adiabatic, isobaric oxidation of methane using the reaction rate expression of Fit 3 of Section 4.2.5.

The methane flame experiment results presented in Chapter 3 (Figure 3.8) are in the form of minimum fuel fractions plotted as a function of temperature. To put the current model results in the same form, initial methane concentrations are varied at a fixed temperature until the predicted critical time matches an appropriate experimental flow time. The flow time in our reactor, based on injection velocity and reactor height, is about 0.25 seconds at conditions of the flame experiments. Since an initial fuel fraction of 9.1% produces the correct critical time of 0.25 s (see Figure 5.7), it is the predicted minimum fuel fraction for spontaneous ignition at 460 °C.

Figure 5.8 compares predicted and observed methane fractions required for spontaneous ignition in supercritical water. At low temperatures, the model predicts that flames should only ignite at very high fuel fractions. At higher

temperatures, model predictions approach the experimental observations. It should be pointed out that ignition model performance is not as poor as the figure at first suggests. The reaction rate expression used in the model was derived from isothermal kinetics experiments conducted on a time scale on the order of hours. It is encouraging that the model can approximate (at high temperatures) the ignition event that takes place over a much shorter time scale.

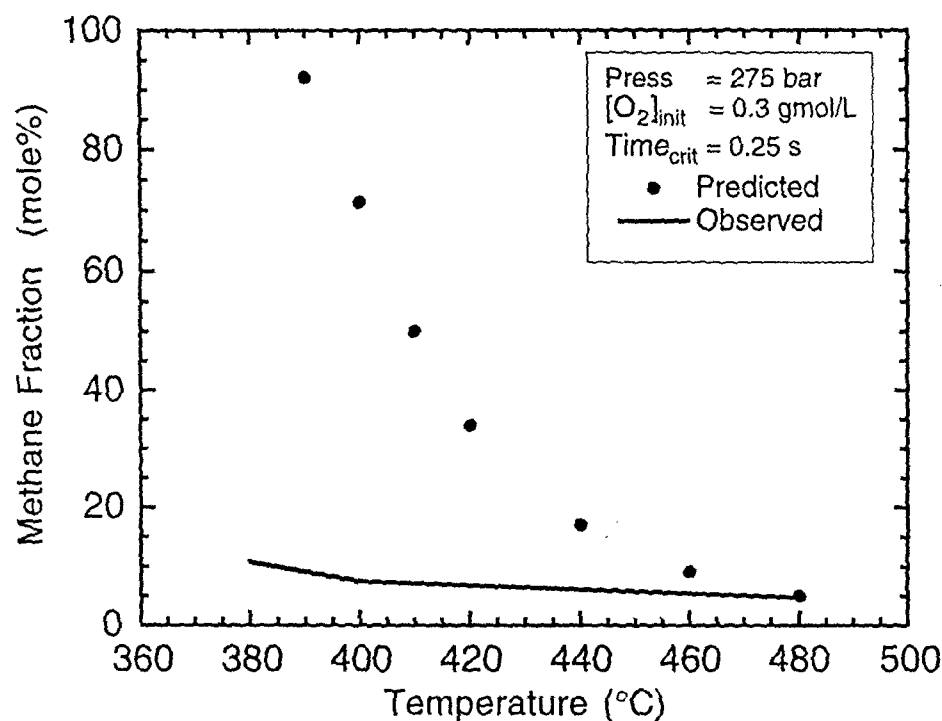


Figure 5.8. Predicted and observed minimum ignition fuel fractions for methane in supercritical water at  $P = 275$  bar. The observed line is extracted from Figure 3.8.

The deviation of predictions at low temperatures in Figure 5.8 is an indication that the ignition scenario used in the model is not the only means of ignition in the experiments. It is unavoidable that premixed parcels of fuel and oxygen actually recirculate within the reactor at time scales much longer than the 0.25 seconds specified for the model. The ignition process in our reactor at low temperatures thus would be better characterized by a model with longer residence times. The experimental data support this explanation in that ignition at lower temperatures often involved delays longer than a second.

## **5.6. Conclusions**

While the current modeling results for supercritical water oxidation of methane capture several important trends observed in the experiments, further work will be required for quantitative predictions. The Pitz-C1 elementary reaction mechanism shows moderate success at predicting overall methane consumption rates at 135 bar, but overpredicts rates at 270 bar. The model does predict the observed downturn in overall rate with increasing water density, albeit at a higher density. The attempt to predict flame ignition by adding a one-step reaction rate expression to an adiabatic, plug-flow model met with limited success. These efforts indicate that current tools for modeling SCWO require further modification. Previously available experimental observations covered a limited range of conditions. The current data widen the range of fuel concentrations and mixture densities available as input in the development of future models.



## 6. Summary and Conclusions

Experiments have been conducted to study the oxidation of methane and methanol in supercritical water. The research included two groups of experiments: (1) auto-ignition of methane and methanol diffusion flames, and (2) measurements of methane chemical kinetics. Both were performed in an optically accessible, high-pressure reactor using Raman spectroscopy to measure *in situ* concentrations of major species. Experimental pressures were varied from 35 to 275 bar to determine the effect of water density on the oxidation process. Initial fuel concentrations ranged as high as 3 gmol/L in the flame experiments and 0.2 gmol/L in the kinetics experiments. Initial temperatures varied from 380 to 510 °C. A current SCWO kinetic mechanism from the literature was incorporated into a real-gas model and predictions were compared with experimental observations. The following conclusions were drawn:

### *Flame Experiments:*

1. Slender flames ignite and burn steadily upon injection of oxygen into a mixture of supercritical water and fuel. Intensities of the flames vary dramatically with fuel concentration, while the flame aspect ratio appears insensitive to this parameter.
2. At temperatures above 470 °C, flames spontaneously ignite in mixtures containing only 6 mole% methane or methanol. This information is relevant to the design and operation of SCWO processes that may be susceptible to inadvertent flame formation.
3. At lower temperatures, methanol is less likely to ignite than methane.

### *Kinetics Experiments:*

1. Raman spectroscopy is well adapted to the *in situ* measurement of concentrations of multiple species during SCWO kinetics experiments.
2. Methane data from the constant volume reactor complements previous measurements primarily made in flow reactors. Advantages of our apparatus include: SCWO-process-like fuel concentrations, high data rates, long residence times, and *in situ* measurements. Disadvantages include: limited temperature range and non-negligible settling times.



3. Observed reaction rates at 270 bar can be approximated by a one-step rate expression that has a reaction order close to two for methane and approximately zero for oxygen. These values match earlier measurements of oxygen reaction orders, but not previous values of methane reaction order, which were close to unity. This new information is important since it characterizes destruction rates at concentrations typical of actual SCWO processes.
4. At a constant temperature of 412 °C, the rate of methane consumption in our apparatus rises steadily with water density up to ~ 5 gmol/L (P ~ 200 bar). At higher densities, however, the influence of pressure is reversed and the rate decreases. No such reversal was observed for argon, although the maximum attainable argon density was only 4 gmol/L.

#### *Model Assessments:*

1. A current elementary reaction mechanism adapted to supercritical water environments strongly overpredicts rates observed in the methane kinetics experiments at 270 bar; however, agreement at 135 bar is much better.
2. An analysis of the mechanism suggests that it contains the necessary elementary reactions to explain our observed downturn in overall reaction rate with increasing water density. However, the model predicts the reversal at a higher density than was experimentally observed. Adjustment of the rate of methyl recombination with water moves the point of reversal toward the observed density.
3. The derived global rate expression from our kinetics experiments predicts spontaneous flame ignition at the injection time scale of our reactor. However, the minimum fuel fractions for ignition are overpredicted, except at the highest temperatures.

#### *Recommendations for future research:*

1. Perform further experiments to identify the water density at which rates are a maximum. Extend argon measurements to higher densities.
2. Perform sensitivity and flux analyses on the Pitz-C1 mechanism to determine the key reactions for the conditions that were studied. Use the tuned mechanism to refine our understanding of the density dependence of overall oxidation rates in supercritical water.
3. Extend kinetics measurements to other fuels, including CO, and compare with previous observations.

## 7. Appendices

Included as appendices are three sections: (7.1) the elementary reaction mechanism used in the modeling; (7.2) a list of the flame ignition experimental data; and (7.3) a list of the methane kinetics experimental data.

### **7.1. Elementary Reaction Mechanism**

Listed on the following pages is the Pitz-C1 elementary reaction mechanism used to model the oxidation of methane in supercritical water. It consists of the Pitz mechanism (Alkam, *et al.*, 1995) with all C<sub>2</sub> species removed. The original reaction numbers from the complete mechanism are retained. Units of the preexponential factor,  $A$ , are gmol, cm, s, and K; units of activation energy are cal/gmol.

Rxn#	Elementary Reaction	A	b	E <sub>a</sub>
1	H + O <sub>2</sub> = OH + O	1.91E + 14	0	16440
2	H <sub>2</sub> + O = H + OH	5.13E + 04	2.7	6286
3	OH + H <sub>2</sub> = H + H <sub>2</sub> O	2.14E + 08	1.5	3430
4	OH + OH = O + H <sub>2</sub> O	5.63E + 11	0.3	1425
5	H <sub>2</sub> + M = H + H + M	8.51E + 19	-1.1	104370
6	H + OH + M = H <sub>2</sub> O + M	1.38E + 23	-2	0
7	H + O <sub>2</sub> = HO <sub>2</sub>	4.79E + 13	0	-384.8
8	H + HO <sub>2</sub> = OH + OH	1.70E + 14	0	870
9	H + HO <sub>2</sub> = H <sub>2</sub> + O <sub>2</sub>	6.61E + 13	0	2129
10	HO <sub>2</sub> + O = O <sub>2</sub> + OH	1.74E + 13	0	-399.1
11	OH + HO <sub>2</sub> = H <sub>2</sub> O + O <sub>2</sub>	1.45E + 16	-1	0
12	H <sub>2</sub> O <sub>2</sub> + OH = H <sub>2</sub> O + HO <sub>2</sub>	1.75E + 12	0	318
13	HO <sub>2</sub> + HO <sub>2</sub> = H <sub>2</sub> O <sub>2</sub> + O <sub>2</sub>	1.70E + 13	0	4211.3
14	OH + OH = H <sub>2</sub> O <sub>2</sub>	7.59E + 13	-0.4	0
15	H <sub>2</sub> O <sub>2</sub> + H = HO <sub>2</sub> + H <sub>2</sub>	4.79E + 13	0	7949
16	H <sub>2</sub> O <sub>2</sub> + H = H <sub>2</sub> O + OH	1.00E + 13	0	3590
17	O + H + M = OH + M	4.68E + 18	-1	0
18	O + O + M = O <sub>2</sub> + M	3.98E + 14	0	-1790
19	H <sub>2</sub> O <sub>2</sub> + O = OH + HO <sub>2</sub>	9.55E + 06	2	3970
20	CH <sub>3</sub> OH + O <sub>2</sub> => CH <sub>2</sub> OH + HO <sub>2</sub>	2.00E + 13	0	44910
21	CH <sub>2</sub> OH + HO <sub>2</sub> => CH <sub>3</sub> OH + O <sub>2</sub>	1.06E + 13	-0.5	-1500
22	CH <sub>4</sub> = CH <sub>3</sub> + H	3.71E + 15	0	103810
23	CH <sub>4</sub> + H => CH <sub>3</sub> + H <sub>2</sub>	2.24E + 04	3	8750
24	CH <sub>3</sub> + H <sub>2</sub> => CH <sub>4</sub> + H	2.89E + 02	3.1	8711
25	CH <sub>4</sub> + OH => CH <sub>3</sub> + H <sub>2</sub> O	1.93E + 05	2.4	2106
26	CH <sub>3</sub> + H <sub>2</sub> O => CH <sub>4</sub> + OH	4.82E + 02	2.9	14860
27	CH <sub>4</sub> + O => CH <sub>3</sub> + OH	2.13E + 06	2.2	6480
28	CH <sub>3</sub> + OH => CH <sub>4</sub> + O	3.56E + 04	2.2	3920
31	HCO + OH = CO + H <sub>2</sub> O	3.02E + 13	0	0
32	OH + CO = H + CO <sub>2</sub>	2.85E + 07	1.3	-765
33	HCO + M = H + CO + M	3.47E + 18	-1	17000
35	CH <sub>3</sub> OH => CH <sub>3</sub> + OH	1.90E + 16	0	91780
36	CH <sub>3</sub> + OH => CH <sub>3</sub> OH	1.98E + 12	0.4	-708
37	CH <sub>3</sub> OH => CH <sub>2</sub> OH + H	1.60E + 16	0	96790
38	CH <sub>2</sub> OH + H => CH <sub>3</sub> OH	1.28E + 14	0	381
41	CH <sub>3</sub> OH + HO <sub>2</sub> => CH <sub>2</sub> OH + H <sub>2</sub> O <sub>2</sub>	5.40E + 11	0	17800
42	CH <sub>2</sub> OH + H <sub>2</sub> O <sub>2</sub> => CH <sub>3</sub> OH + HO <sub>2</sub>	3.19E + 10	0	8150
47	CH <sub>3</sub> + HO <sub>2</sub> => CH <sub>3</sub> O + OH	3.20E + 13	0	0
48	CH <sub>3</sub> O + OH => CH <sub>3</sub> + HO <sub>2</sub>	3.33E + 14	0	25380
49	CO + HO <sub>2</sub> = CO <sub>2</sub> + OH	6.03E + 13	0	22950
51	CO + O = CO <sub>2</sub>	1.82E + 10	0	2431
52	CO + O <sub>2</sub> = CO <sub>2</sub> + O	2.51E + 12	0	47690
53	HCO + H = CO + H <sub>2</sub>	7.24E + 13	0	0
54	O + HCO = CO + OH	3.02E + 13	0	0

Rxn#	Elementary Reaction	A	b	E <sub>a</sub>
55	CH <sub>2</sub> O + M => HCO + H + M	3.30E + 16	0	81000
56	HCO + H + M => CH <sub>2</sub> O + M	1.40E + 11	1	-11770
57	CH <sub>2</sub> O + OH => HCO + H <sub>2</sub> O	3.43E + 09	1.2	-447
58	HCO + H <sub>2</sub> O => CH <sub>2</sub> O + OH	2.35E + 08	1.4	26120
59	CH <sub>2</sub> O + H => HCO + H <sub>2</sub>	3.30E + 14	0	10500
60	HCO + H <sub>2</sub> => CH <sub>2</sub> O + H	2.64E + 13	0	25170
61	CH <sub>2</sub> O + O => HCO + OH	5.00E + 13	0	4600
62	HCO + OH => CH <sub>2</sub> O + O	1.75E + 12	0	17170
63	CH <sub>2</sub> O + CH <sub>2</sub> OH => HCO + CH <sub>3</sub> OH	5.54E + 03	2.8	5862
64	HCO + CH <sub>3</sub> OH => CH <sub>2</sub> O + CH <sub>2</sub> OH	2.82E + 02	3.3	11510
65	CH <sub>3</sub> + OH => CH <sub>2</sub> O + H <sub>2</sub>	4.00E + 12	0	0
66	CH <sub>2</sub> O + H <sub>2</sub> => CH <sub>3</sub> + OH	1.20E + 14	0	71720
67	CH <sub>3</sub> + O => CH <sub>2</sub> O + H	1.30E + 14	0	2000
68	CH <sub>2</sub> O + H => CH <sub>3</sub> + O	1.70E + 15	0	71630
69	CH <sub>3</sub> + O <sub>2</sub> => CH <sub>3</sub> O + O	4.80E + 13	0	29000
70	CH <sub>3</sub> O + O => CH <sub>3</sub> + O <sub>2</sub>	3.04E + 14	0	733
71	CH <sub>2</sub> O + CH <sub>3</sub> => HCO + CH <sub>4</sub>	5.54E + 03	2.8	5860
72	HCO + CH <sub>4</sub> => CH <sub>2</sub> O + CH <sub>3</sub>	7.29E + 03	2.9	22510
73	HCO + CH <sub>3</sub> => CH <sub>4</sub> + CO	3.00E + 11	0.5	0
74	CH <sub>4</sub> + CO => HCO + CH <sub>3</sub>	5.14E + 13	0.5	90470
75	CH <sub>3</sub> O = CH <sub>2</sub> O + H	1.84E + 14	0	29110
76	CH <sub>3</sub> O + M = CH <sub>3</sub> O + M	0.00E + 00	0	0
79	HCO + HO <sub>2</sub> => CH <sub>2</sub> O + O <sub>2</sub>	1.00E + 14	0	3000
80	CH <sub>2</sub> O + O <sub>2</sub> => HCO + HO <sub>2</sub>	3.66E + 15	0	46040
81	CH <sub>3</sub> O + O <sub>2</sub> => CH <sub>2</sub> O + HO <sub>2</sub>	7.60E + 10	0	2700
82	CH <sub>2</sub> O + HO <sub>2</sub> => CH <sub>3</sub> O + O <sub>2</sub>	1.28E + 11	0	32170
83	CH <sub>3</sub> + HO <sub>2</sub> => CH <sub>4</sub> + O <sub>2</sub>	1.00E + 12	0	400
84	CH <sub>4</sub> + O <sub>2</sub> => CH <sub>3</sub> + HO <sub>2</sub>	7.63E + 13	0	58590
85	HCO + O <sub>2</sub> = CO + HO <sub>2</sub>	7.59E + 12	0	411.1
86	CH <sub>4</sub> + HO <sub>2</sub> => CH <sub>3</sub> + H <sub>2</sub> O <sub>2</sub>	1.12E + 13	0	24640
87	CH <sub>3</sub> + H <sub>2</sub> O <sub>2</sub> => CH <sub>4</sub> + HO <sub>2</sub>	7.43E + 11	0	5500
88	CH <sub>2</sub> O + HO <sub>2</sub> => HCO + H <sub>2</sub> O <sub>2</sub>	5.60E + 12	0	13600
89	HCO + H <sub>2</sub> O <sub>2</sub> => CH <sub>2</sub> O + HO <sub>2</sub>	7.79E + 11	0	10230
116	CH <sub>2</sub> + O <sub>2</sub> => HCO + OH	1.00E + 14	0	3700
117	HCO + OH => CH <sub>2</sub> + O <sub>2</sub>	4.12E + 13	0	76580
118	CH <sub>2</sub> + O => CH + OH	1.90E + 11	0.7	25000
119	CH + OH => CH <sub>2</sub> + O	5.86E + 10	0.7	25930
120	CH <sub>2</sub> + H => CH + H <sub>2</sub>	2.70E + 11	0.7	25700
121	CH + H <sub>2</sub> => CH <sub>2</sub> + H	1.90E + 11	0.7	28730
122	CH <sub>2</sub> + OH => CH + H <sub>2</sub> O	2.70E + 11	0.7	25700
123	CH + H <sub>2</sub> O => CH <sub>2</sub> + OH	8.21E + 11	0.7	43880
124	CH + O <sub>2</sub> => CO + OH	1.35E + 11	0.7	25700
125	CO + OH => CH + O <sub>2</sub>	5.19E + 11	0.7	185600
126	CH + O <sub>2</sub> => HCO + O	1.00E + 13	0	0

Rxn#	Elementary Reaction	A	b	E <sub>a</sub>
127	HCO + O => CH + O2	1.33E + 13	0	71950
128	CH3OH + OH => CH2OH + H2O	1.77E + 04	2.7	-883
129	CH2OH + H2O => CH3OH + OH	2.38E + 03	2.7	21860
130	CH3OH + H => CH2OH + H2	3.20E + 13	0	6095
131	CH2OH + H2 => CH3OH + H	9.12E + 12	0	13650
132	CH3OH + H => CH3O + H2	8.00E + 12	0	6095
133	CH3O + H2 => CH3OH + H	1.32E + 12	0.2	6018
134	CH3OH + CH3 => CH2OH + CH4	3.19E + 01	3.2	7170
135	CH2OH + CH4 => CH3OH + CH3	1.87E + 02	2.9	16100
136	CH3OH + CH3 => CH3O + CH4	1.45E + 02	3.1	6935
137	CH3O + CH4 => CH3OH + CH3	2.65E + 02	3.1	8115
138	CH3OH + O => CH2OH + OH	3.88E + 05	2.5	3080
139	CH2OH + OH => CH3OH + O	4.96E + 03	2.5	8781
140	CH2OH + O2 => CH2O + HO2	2.14E + 14	0	5000
141	CH2O + HO2 => CH2OH + O2	7.85E + 12	0.6	25860
142	CH2OH + M => CH2O + H + M	1.85E + 24	-2.5	34190
143	CH2O + H + M => CH2OH + M	1.06E + 23	-2	5901
144	CH2OH + OH => CH2O + H2O	2.40E + 13	0	0
145	CH2O + H2O => CH2OH + OH	1.18E + 12	0.9	90340
146	CH2OH + H => CH2O + H2	3.00E + 13	0	0
147	CH2O + H2 => CH2OH + H	3.27E + 11	0.9	75160
184	CH3OH + CH2O => CH3O + CH3O	1.53E + 12	0	79570
185	CH3O + CH3O => CH3OH + CH2O	3.00E + 13	0	0
186	CH2O + CH3O => CH3OH + HCO	1.15E + 11	0	1280
187	CH3OH + HCO => CH2O + CH3O	3.02E + 11	0	18160
192	CH3O + CH3OH => CH2OH + CH3OH	1.51E + 12	0	7000
193	CH2OH + CH3OH => CH3O + CH3OH	2.19E + 05	1.7	10850
194	CH3OH + OH => CH3O + H2O	1.77E + 04	2.7	-883
195	CH3O + H2O => CH3OH + OH	1.33E + 04	2.8	14220
206	CH3O2 + M => CH3 + O2 + M	4.03E + 19	-1	29800
207	CH3 + O2 + M => CH3O2 + M	1.41E + 15	0	-1100
208	CH3O2H => CH3O + OH	6.46E + 14	0	43000
209	CH3O + OH => CH3O2H	1.00E + 11	0	0
214	CH3O2 + CH2O => CH3O2H + HCO	5.60E + 12	0	13600
215	CH3O2H + HCO => CH3O2 + CH2O	8.00E + 11	0	10000
222	CH4 + CH3O2 => CH3 + CH3O2H	1.12E + 13	0	24640
223	CH3 + CH3O2H => CH4 + CH3O2	7.43E + 11	0	5500
226	CH3OH + CH3O2 => CH2OH + CH3O2H	6.30E + 12	0	19360
227	CH2OH + CH3O2H => CH3OH + CH3O2	1.00E + 09	0	10000
232	CH3O2 + CH3 => CH3O + CH3O	1.90E + 12	0	-1200
233	CH3O + CH3O => CH3O2 + CH3	2.00E + 10	0	0
236	CH3O2 + HO2 => CH3O2H + O2	4.60E + 10	0	-2600
237	CH3O2H + O2 => CH3O2 + HO2	3.00E + 12	0	39000
238	CH3O2 + HO2 => CH3O + OH + O2	1.00E + 11	0	0

Rxn#	Elementary Reaction	A	b	E <sub>a</sub>
239	CH <sub>3</sub> O + OH + O <sub>2</sub> => CH <sub>3</sub> O <sub>2</sub> + HO <sub>2</sub>	0.00E + 00	0	0
242	CH <sub>3</sub> O <sub>2</sub> + CH <sub>3</sub> O <sub>2</sub> => CH <sub>2</sub> O + CH <sub>3</sub> OH + O <sub>2</sub>	7.60E + 10	0	-500
243	CH <sub>2</sub> O + CH <sub>3</sub> OH + O <sub>2</sub> => CH <sub>3</sub> O <sub>2</sub> + CH <sub>3</sub> O <sub>2</sub>	0.00E + 00	0	0
244	CH <sub>3</sub> O <sub>2</sub> + CH <sub>3</sub> O <sub>2</sub> => O <sub>2</sub> + CH <sub>3</sub> O + CH <sub>3</sub> O	3.70E + 11	0	2200
245	O <sub>2</sub> + CH <sub>3</sub> O + CH <sub>3</sub> O => CH <sub>3</sub> O <sub>2</sub> + CH <sub>3</sub> O <sub>2</sub>	0.00E + 00	0	0
284	HCO + O => CO <sub>2</sub> + H	1.00E + 13	0	0
285	CO <sub>2</sub> + H => HCO + O	3.23E + 15	0	110200
286	CH <sub>3</sub> + M => CH <sub>2</sub> + H + M	4.68E + 16	0	93800
287	CH <sub>2</sub> + H + M => CH <sub>3</sub> + M	5.01E + 11	1	-18340
288	CH <sub>3</sub> + H => CH <sub>2</sub> + H <sub>2</sub>	7.24E + 14	0	15200
289	CH <sub>2</sub> + H <sub>2</sub> => CH <sub>3</sub> + H	1.46E + 14	0	10500
290	CH <sub>3</sub> + OH => CH <sub>2</sub> + H <sub>2</sub> O	1.50E + 13	0	5000
291	CH <sub>2</sub> + H <sub>2</sub> O => CH <sub>3</sub> + OH	1.31E + 13	0	15450
294	CH <sub>4</sub> + CH <sub>2</sub> => CH <sub>3</sub> + CH <sub>3</sub>	1.00E + 13	0	0
295	CH <sub>3</sub> + CH <sub>3</sub> => CH <sub>4</sub> + CH <sub>2</sub>	1.90E + 12	0	4225



## **7.2. Flame Ignition Experiments**

Listed in Section 7.2.1 are all the hydrothermal flame ignition trials performed at 275 bar. Section 7.2.2 lists the methanol trials.



## 7.2.1. Methane Hydrothermal Flame Ignition Trials

Methane Exper. #	Temp. (°C)	Pressure (bar)	Initial [CH <sub>4</sub> ] (gmol/L)	Initial X <sub>CH<sub>4</sub></sub> (mole%)	Auto Ignites?
11290	401	274	0.395	4.4	no
11290	402	274	0.584	7.4	yes
11290	406	275	0.863	12.4	yes
11290	408	271	0.690	9.8	yes
11290	409	276	0.741	10.4	yes
11290	409	274	0.609	8.3	yes
12050	405	275	0.820	11.6	yes
12050	407	277	0.520	6.6	no
12050	407	275	0.720	9.9	no
12050	406	280	0.920	13.0	yes
02061	403	278	0.926	13.0	yes
02061	401	275	1.277	19.9	yes
02061	405	276	1.522	25.6	yes
02061	405	275	0.939	13.8	yes
02061	408	280	0.801	11.1	yes
02061	409	277	0.545	7.1	yes
02071	404	280	0.333	3.5	no
02071	398	281	0.458	4.6	no
02071	396	278	0.648	7.2	no
02071	404	276	1.069	16.0	yes
02071	407	276	1.005	15.2	yes
02071	409	281	0.635	8.3	yes
02111	405	278	0.671	8.8	no
02111	402	277	0.802	10.7	yes
02111	410	276	0.851	12.4	yes
02111	407	276	0.814	11.6	yes
02111	402	280	0.737	9.4	no
02141	471	275	1.172	23.2	yes
02141	480	276	0.894	17.4	yes
02141	481	281	0.360	6.2	yes
02141	473	280	0.373	6.3	no
02141	474	279	0.203	3.3	no
02141	476	280	0.248	4.1	no
02141	478	276	0.271	4.7	yes
02141	478	278	0.438	7.7	yes
02181	383	279	0.705	5.1	no
02181	380	276	0.960	9.0	no
02181	377	275	1.502	18.7	yes
02181	380	274	1.304	15.9	yes
02181	380	277	1.066	10.7	yes
02181	382	275	0.945	9.9	no

## 7.2.2. Methanol Hydrothermal Flame Ignition Trials

Exper. #	Temp. (°C)	Pressure (bar)	Initial [CH <sub>3</sub> OH] (gmol/L)	Initial X <sub>CH<sub>3</sub>OH</sub> (mole%)	Auto Ignites?
02191	405	278	2.821	41.9	yes
02191	410	274	2.194	32.9	yes
02191	410	279	2.257	32.3	yes
02191	411	270	1.005	13.7	yes
02191	401	278	0.729	7.9	no
02201	404	279	1.228	15.4	yes
02201	408	277	1.364	18.4	yes
02201	407	274	2.041	29.9	yes
02281	470	264	2.945	58.2	yes
02281	475	277	2.568	48.7	yes
02281	474	270	1.123	20.6	yes
02281	472	272	0.757	13.3	yes
02281	473	273	0.346	5.8	yes
02281	476	274	0.286	4.8	no
03011	402	277	1.142	14.0	no
03011	404	278	2.188	31.2	yes
03011	400	280	0.860	9.3	no
03011	402	272	1.602	22.0	yes
03011	404	279	1.709	23.0	yes
03011	408	272	1.019	13.4	no
03131	402	280	1.183	14.3	no
03131	402	280	1.977	26.7	yes
03131	402	280	2.263	31.4	yes
03131	402	280	1.704	22.4	yes
03131	403	281	1.061	12.6	no
03141	382	278	2.143	22.7	no
03141	381	279	2.622	29.3	no
03141	380	278	3.640	44.2	yes
03141	381	279	3.088	36.1	yes
03191	501	276	1.731	34.5	yes
03191	508	273	1.163	23.3	yes
03191	509	278	0.752	14.4	yes
03191	511	271	0.455	8.9	yes



### **7.3. Methane Kinetics Experiments**

The following pages list experimental data from the methane oxidation kinetics experiments. Included are the 270-bar experiments, the 135-bar experiments, the experiments at 412 °C over a wide range of pressures, and the experiments in argon. The data for each experiment comprise a series of Raman measurements of CH<sub>4</sub>, O<sub>2</sub>, N<sub>2</sub>, CO<sub>2</sub>, and CO concentrations. Listed with each concentration measurement are the corresponding time, temperature, and pressure measurements. The full (as opposed to abridged) data sets for each experiment are listed.





Experiment no	Methane				Oxygen				Nitrogen				Carbon Dioxide				Carbon Monoxide			
	Time (min)	Temp (°C)	Press (bar)	Conc (gmol/L)	Time (min)	Temp (°C)	Press (bar)	Conc (gmol/L)	Time (min)	Temp (°C)	Press (bar)	Conc (gmol/L)	Time (min)	Temp (°C)	Press (bar)	Conc (gmol/L)	Time (min)	Temp (°C)	Press (bar)	Conc (gmol/L)
1	0.00	419	234.6	0.131	1.89	419	275.8	0.341	3.77	419	274.6	0.373	2.55	419	275.4	0.032				
	1.00	420	276.2	0.074	4.42	419	274.1	0.227	6.32	419	273.3	0.332	4.99	419	273.9	0.050				
	3.19	419	275.0	0.068	6.94	419	273.1	0.190	8.85	419	272.5	0.333	7.60	420	272.9	0.063				
	5.69	420	273.7	0.058	9.50	419	272.3	0.168	11.42	419	271.7	0.331	10.07	419	271.9	0.072				
	8.22	419	272.7	0.048	12.09	419	271.4	0.151	14.27	419	271.0	0.326	12.59	419	271.4	0.076				
	10.80	419	271.9	0.042	15.05	419	270.8	0.146	17.39	419	270.3	0.329	15.79	419	270.8	0.082				
	13.34	419	271.2	0.037	18.17	419	270.1	0.135	20.85	419	269.9	0.325	18.89	419	270.3	0.088				
	15.65	419	270.6	0.033	21.70	419	269.9	0.124	23.70	419	269.5	0.323	22.42	419	269.7	0.093				
	19.99	419	269.9	0.029	24.54	419	269.5	0.111	26.99	419	269.3	0.318	25.39	419	269.3	0.097				
	23.09	419	269.7	0.026	27.55	419	269.1	0.111	30.27	419	268.9	0.322	28.32	419	269.1	0.097				
	25.97	419	269.3	0.024	31.02	419	268.9	0.110	33.14	419	268.7	0.324	31.59	419	268.7	0.100				
	28.44	419	268.9	0.022	33.89	419	268.7	0.109	36.24	419	268.7	0.327	34.69	419	268.7	0.100				
	32.47	419	268.9	0.020	36.87	419	268.5	0.108	39.47	419	268.3	0.328	37.85	419	268.5	0.104				
	35.49	419	268.5	0.019	43.44	419	268.3	0.098	45.89	419	268.3	0.325	40.99	419	268.3	0.104				
	38.72	419	268.3	0.018	46.55	419	268.1	0.099	48.80	419	268.1	0.329	44.20	419	268.1	0.107				
	41.87	419	268.1	0.017	49.50	419	267.7	0.098	51.85	419	267.7	0.321	50.30	419	267.9	0.108				
	45.04	419	268.1	0.016	52.52	419	267.7	0.090	54.85	419	267.7	0.320	53.15	419	267.7	0.110				
	48.09	419	268.1	0.015	55.62	419	267.7	0.088	57.94	419	267.7	0.321	56.47	419	267.7	0.109				
	50.99	419	267.9	0.015	58.69	419	267.4	0.087	61.05	419	267.4	0.320	59.44	419	267.4	0.111				
	54.09	419	267.9	0.015	61.69	419	267.4	0.084	64.09	419	267.4	0.324	62.34	419	267.4	0.112				
57.17	419	267.7	0.014	64.90	419	267.4	0.084	67.55	419	267.2	0.324	65.80	419	267.2	0.115					
60.12	419	267.4	0.012	68.47	419	267.2	0.083	71.15	419	267.2	0.323	69.22	419	267.2	0.115					
63.24	419	267.4	0.012	72.10	419	267.2	0.083	74.92	419	267.2	0.324	73.50	419	267.2	0.113					
66.64	419	267.4	0.012	75.67	419	267.2	0.077	78.07	419	267.2	0.322	76.44	419	267.2	0.115					
70.15	419	267.2	0.012	78.82	419	267.0	0.077	81.02	419	267.0	0.320	79.55	419	267.2	0.114					
74.27	419	267.0	0.011	81.75	419	267.0	0.077	83.97	419	267.0	0.320	82.42	419	266.8	0.116					
77.24	419	267.0	0.010	84.59	419	266.8	0.077	86.94	419	266.8	0.318	85.25	419	266.8	0.116					
80.27	419	267.0	0.010	87.82	419	266.8	0.074	90.70	419	266.8	0.318	88.32	419	266.8	0.116					
83.25	419	267.0	0.010	91.50	419	266.8	0.073	93.92	419	266.8	0.319	92.39	419	266.8	0.118					
86.15	419	267.0	0.010	94.52	419	266.8	0.073	96.84	419	266.8	0.323	95.15	419	266.8	0.118					
89.17	419	266.8	0.009	98.17	419	266.8	0.073	100.20	419	266.8	0.323	98.44	419	266.8	0.118					
93.00	419	266.8	0.009	97.64	419	266.8	0.073	103.05	419	266.8	0.316	101.60	419	266.8	0.117					
96.02	419	266.8	0.009	100.92	419	266.6	0.072	106.80	419	266.6	0.322	104.60	419	266.6	0.117					
99.32	419	266.8	0.008	103.90	419	266.6	0.071	111.85	419	266.6	0.317	110.39	419	266.6	0.119					
102.42	419	266.8	0.009	109.45	419	266.6	0.069	114.99	419	266.6	0.317	113.39	419	266.6	0.119					
105.44	419	266.6	0.008	112.57	419	266.6	0.069	118.27	419	266.4	0.317	116.70	419	266.4	0.120					
110.85	419	266.6	0.007	115.82	419	266.6	0.069	121.20	419	266.4	0.316	119.79	419	266.4	0.118					
114.27	419	266.4	0.007	118.97	419	266.6	0.069	124.97	419	266.4	0.316	122.62	419	266.4	0.122					
117.50	419	266.4	0.007	121.90	419	266.4	0.066	127.19	419	266.4	0.316	125.82	419	266.4	0.121					
120.49	419	266.4	0.007	124.97	419	266.4	0.066	130.19	419	266.2	0.316	128.65	419	266.2	0.119					
123.42	419	266.4	0.007	127.90	419	266.4	0.066	133.14	419	266.2	0.317	131.74	419	266.2	0.122					
126.49	419	266.4	0.007	131.12	419	266.4	0.065	136.19	419	266.2	0.316	134.64	419	266.2	0.121					
129.39	419	266.2	0.006	133.95	419	266.2	0.063	139.39	419	266.2	0.319	137.85	419	266.2	0.121					
132.52	419	266.2	0.006	136.82	419	266.2	0.065	142.89	419	266.0	0.313	140.99	419	266.2	0.121					
135.40	419	266.4	0.006	140.15	419	266.0	0.065	145.82	419	266.0	0.309	144.44	419	266.2	0.125					
138.72	419	266.2	0.006	143.69	419	266.0	0.062	148.89	419	266.0	0.311	147.42	419	266.2	0.120					
141.79	419	266.0	0.005	146.70	419	266.0	0.061	149.25	419	266.0			150.92	419	266.0	0.124				
145.09	419	266.0	0.005	150.20	419	266.2	0.063													
148.25	419	266.0	0.005																	
151.69	419	266.0	0.005																	





	Methane				Oxygen				Nitrogen				Carbon Dioxide				Carbon Monoxide			
	Time (min)	Temp (°C)	Press (bar)	Conc (gmol/L)	Time (min)	Temp (°C)	Press (bar)	Conc (gmol/L)	Time (min)	Temp (°C)	Press (bar)	Conc (gmol/L)	Time (min)	Temp (°C)	Press (bar)	Conc (gmol/L)	Time (min)	Temp (°C)	Press (bar)	Conc (gmol/L)
0.00	395	234.8	0.117	1.90	397	280.4	0.374	5.05	395	281.9	0.421	4.29	395	281.7	0.013	3.40	396	281.4	0.009	
1.00	397	278.3	0.090	7.37	395	282.1	0.366	36.35	397	279.0	0.368	8.09	395	282.1	0.030	6.49	395	282.1	0.012	
5.70	395	282.1	0.078	10.34	397	281.7	0.315	40.70	397	278.8	0.401	11.20	397	281.7	0.034	9.49	397	281.7	0.012	
8.75	397	282.1	0.069	13.44	397	280.8	0.300	44.27	397	278.3	0.397	14.25	397	281.2	0.039	12.80	397	281.4	0.011	
11.99	397	281.0	0.065	16.74	397	280.6	0.287	48.07	397	278.1	0.386	17.60	397	280.6	0.043	15.90	397	281.0	0.009	
15.09	397	281.0	0.060	20.10	397	280.2	0.283	51.59	397	278.1	0.386	20.92	397	280.6	0.047	19.15	397	280.6	0.009	
18.37	397	280.8	0.060	23.70	397	280.2	0.279	54.65	397	277.9	0.396	24.75	397	280.0	0.053	22.94	397	280.2	0.008	
22.04	396	280.2	0.057	27.12	397	279.8	0.274	57.82	397	277.9	0.392	28.29	397	279.6	0.057	26.54	397	280.0	0.008	
25.64	397	280.0	0.050	30.92	397	279.4	0.266	61.42	396	277.2	0.391	31.72	397	279.4	0.061	30.14	397	279.4	0.008	
29.39	397	279.6	0.050	34.35	397	279.2	0.259	65.24	396	277.2	0.397	35.05	397	279.0	0.065	33.59	397	279.4	0.008	
32.77	397	279.2	0.047	38.02	396	278.6	0.252	69.39	397	277.2	0.388	38.57	397	278.8	0.068					
35.79	397	279.2	0.045	41.90	397	278.6	0.251	72.99	397	277.2	0.387	42.52	397	278.6	0.067					
39.35	397	278.8	0.042	45.57	397	278.3	0.244	76.47	397	276.8	0.388	46.29	397	278.3	0.072					
43.22	397	278.3	0.040	48.74	397	278.1	0.242	79.94	397	276.8	0.381	49.80	397	278.1	0.073					
47.19	397	277.9	0.039	52.34	397	277.9	0.238	83.07	397	276.6	0.387	53.05	397	277.9	0.077					
51.39	397	278.1	0.037	55.39	397	277.9	0.236	87.54	397	276.6	0.387	56.20	397	277.9	0.075					
55.99	397	277.7	0.037	58.60	397	277.7	0.232	91.27	397	276.4	0.381	59.75	397	277.7	0.075					
60.52	397	277.4	0.035	62.24	397	277.4	0.229	95.77	397	276.2	0.378	63.10	397	277.4	0.077					
63.77	397	277.4	0.034	66.04	397	277.2	0.226	99.34	397	276.2	0.384	66.99	397	277.2	0.080					
68.87	397	277.2	0.032	70.07	397	277.2	0.221	102.85	397	276.2	0.380	70.92	397	277.0	0.079					
71.89	397	277.0	0.030	73.90	396	277.0	0.217	105.74	397	276.0	0.376	74.62	397	276.8	0.081					
75.40	397	276.8	0.029	77.42	397	276.8	0.217	109.75	397	276.0	0.378	78.10	397	276.8	0.084					
78.85	397	276.6	0.028	80.77	397	276.6	0.213	113.37	397	275.8	0.380	81.55	397	276.6	0.083					
82.44	397	276.6	0.027	84.57	397	276.6	0.207	116.72	397	275.8	0.377	85.72	397	276.6	0.087					
86.72	397	276.4	0.026	86.99	396	276.6	0.199	120.45	397	275.8	0.371	89.24	395	276.4	0.086					
90.47	397	276.4	0.026	90.92	397	276.2	0.203	123.90	397	275.6	0.369	93.67	397	276.4	0.086					
94.95	397	276.2	0.024	100.24	396	276.0	0.197	130.70	397	275.6	0.369	97.57	396	276.2	0.088					
98.45	397	276.2	0.024	103.54	396	276.0	0.194	134.47	397	275.6	0.371	100.99	397	276.2	0.088					
101.89	397	276.2	0.023	106.55	397	276.0	0.193	137.94	397	275.4	0.372	104.25	397	276.0	0.088					
105.10	397	276.0	0.023	110.72	397	276.0	0.192	141.67	396	275.2	0.367	107.77	397	276.0	0.090					
108.75	397	276.0	0.022	114.07	397	276.0	0.197	145.99	397	275.2	0.366	111.57	397	275.8	0.092					
112.45	397	276.0	0.022	117.49	397	275.8	0.189	149.22	397	275.0	0.366	114.85	397	275.8	0.089					
115.92	397	276.0	0.021	121.45	397	275.8	0.185	153.15	397	275.0	0.369	118.14	397	275.8	0.091					
119.50	397	276.0	0.020	124.80	397	275.8	0.189	157.12	397	275.0	0.366	122.22	397	275.8	0.094					
123.00	397	275.8	0.020	128.15	397	275.6	0.187	161.14	396	274.8	0.364	125.72	397	275.8	0.091					
126.64	397	275.8	0.019	131.74	397	275.6	0.182	165.12	396	274.8	0.368	128.95	397	275.8	0.091					
129.65	397	275.6	0.019	135.87	397	275.4	0.181	169.10	397	274.8	0.369	132.92	397	275.6	0.092					
133.69	397	275.6	0.019	138.97	397	275.4	0.182	173.12	396	274.8	0.370	136.22	397	275.4	0.094					
137.04	397	275.6	0.019	142.82	397	275.2	0.179	177.12	396	274.8	0.364	139.79	397	275.4	0.092					
140.59	397	275.4	0.018	146.82	397	275.2	0.177	181.09	396	274.8	0.369	144.50	397	275.4	0.094					
143.25	397	275.2	0.018	150.10	397	275.2	0.177	185.09	396	274.6	0.373	147.64	397	275.2	0.094					
145.39	397	275.2	0.018	154.17	397	275.2	0.172	189.09	396	274.6	0.373	150.97	397	275.2	0.092					
152.10	397	275.0	0.017	158.10	367	275.0	0.174	193.10	396	274.6	0.370	155.12	397	275.0	0.093					
156.09	396	275.0	0.017	162.17	397	275.0	0.174	197.10	397	274.3	0.366	159.10	396	275.0	0.094					
160.14	397	275.0	0.016	166.10	397	275.0	0.172					163.12	397	274.8	0.094					
163.10	397	275.0	0.016	168.10	396	275.0	0.172					167.10	397	275.0	0.094					
168.10	396	274.8	0.016	170.15	396	275.0	0.172					171.12	396	275.0	0.096					
172.12	397	274.8	0.016	174.14	397	274.8	0.171					175.12	397	274.8	0.095					
176.14	396	274.8	0.016	178.10	397	274.8	0.174					179.09	397	274.8	0.096					
180.10	397	274.8	0.016	182.09	397	274.6	0.169					183.09	397	274.6	0.098					
184.10	396	274.6	0.015	186.20	396	274.6	0.167					187.14	396	274.6	0.099					
188.12	396	274.6	0.015	190.19	397	274.3	0.165					191.14	396	274.3	0.098					
192.10	396	274.6	0.015	194.09	396	274.6	0.169					195.10	396	274.6	0.097					
196.07	396	274.6	0.015	198.10	396	274.3	0.165					199.12	397	274.6	0.098					
200.09	397	274.6	0.015																	







[illegible]



[illegible]









Experiment #	Methane				Oxygen				Nitrogen				Carbon Dioxide				Carbon Monoxide			
	Time (min)	Temp (°C)	Press (bar)	Conc (gmol/L)	Time (min)	Temp (°C)	Press (bar)	Conc (gmol/L)	Time (min)	Temp (°C)	Press (bar)	Conc (gmol/L)	Time (min)	Temp (°C)	Press (bar)	Conc (gmol/L)	Time (min)	Temp (°C)	Press (bar)	Conc (gmol/L)
0.00	411	227.5	0.146	2.98	416	274.6	0.245	5.60	414	271.2	0.368	4.21	415	272.5	0.066	3.38	415	273.5	0.019	
1.51	418	277.2	0.096	7.00	414	270.6	0.152	9.08	414	269.5	0.375	7.66	414	270.1	0.093	6.13	414	270.8	0.017	
4.80	414	271.9	0.065	11.23	413	268.9	0.125	13.96	413	269.3	0.377	12.13	413	268.5	0.106	10.06	413	269.1	0.010	
8.46	414	269.7	0.040	15.76	413	267.9	0.111	18.85	413	267.3	0.371	16.83	413	267.9	0.115	14.81	413	268.1	0.009	
13.11	413	268.3	0.030	20.81	413	267.4	0.101	23.81	413	267.2	0.370	21.86	413	267.2	0.118	19.90	413	267.4	0.007	
17.85	413	267.7	0.024	25.83	413	267.0	0.092	28.85	413	266.8	0.374	26.86	413	266.8	0.125	24.83	413	267.0	0.007	
22.85	413	267.2	0.020	30.83	413	266.6	0.088	33.93	413	266.6	0.365	32.13	413	266.6	0.127	29.86	413	266.6	0.006	
27.81	413	266.8	0.017	35.88	413	266.4	0.088	38.93	413	266.2	0.371	36.84	413	266.6	0.124	34.86	413	266.4	0.006	
33.08	413	266.6	0.015	40.98	413	266.2	0.081	43.86	413	266.2	0.362	41.81	413	266.2	0.128	39.81	413	266.2	0.005	
37.98	413	266.4	0.013	45.90	413	266.2	0.079	48.83	413	266.0	0.365	46.85	413	266.0	0.129	44.83	413	266.2	0.003	
42.91	413	266.0	0.011	51.70	413	265.8	0.072	54.83	413	265.8	0.362	52.83	413	266.0	0.130	50.51	413	266.0	0.001	
47.81	413	266.0	0.011	57.01	413	265.8	0.074	59.81	413	265.8	0.366	57.85	413	265.8	0.131					
53.83	413	265.8	0.009	61.81	413	265.6	0.071	64.83	413	265.6	0.363	62.81	413	265.6	0.132					
58.81	413	265.8	0.009	65.86	413	265.6	0.072	68.86	413	265.6	0.361	66.85	413	265.6	0.130					
64.15	413	265.6	0.008	69.80	413	265.4	0.068	72.83	413	265.4	0.360	70.86	413	265.4	0.132					
68.15	413	265.6	0.007	73.83	413	265.4	0.069	76.90	413	265.4	0.366	74.81	413	265.2	0.133					
71.81	412	265.4	0.007	77.80	413	265.4	0.070	80.81	413	265.4	0.366	78.85	413	265.4	0.130					
75.90	412	265.4	0.006	81.81	412	265.4	0.070	84.81	413	265.2	0.356	82.83	412	265.4	0.131					
79.83	413	265.2	0.006	85.83	413	265.2	0.064	88.83	413	265.2	0.365	86.85	413	265.2	0.135					
83.85	412	265.4	0.006	89.81	413	265.2	0.069	92.83	413	265.2	0.365	90.83	413	265.2	0.134					
87.83	413	265.2	0.006	93.86	413	265.2	0.069	96.83	412	265.2	0.356	94.81	413	265.2	0.133					
91.85	413	265.2	0.005	97.83	413	265.2	0.067	100.80	413	265.0	0.361	98.83	413	265.0	0.135					
95.81	413	265.2	0.005	101.83	413	265.2	0.064	104.83	413	265.0	0.364	102.85	412	265.0	0.133					
99.85	413	265.2	0.004	105.81	413	265.0	0.066	108.83	413	265.0	0.361	106.83	413	265.0	0.133					
103.88	412	265.0	0.005	109.83	413	265.0	0.064	112.86	413	265.2	0.358	111.08	413	265.2	0.133					
107.86	413	265.0	0.005	113.83	413	265.0	0.064	116.88	412	265.0	0.358	114.85	413	265.0	0.132					
111.96	413	265.0	0.004	117.88	413	265.0	0.060	120.85	413	265.0	0.358	118.86	412	265.0	0.135					
115.83	413	265.0	0.005	121.88	413	265.0	0.058	124.81	413	265.0	0.352	122.86	413	265.0	0.135					
119.81	413	265.0	0.004	125.83	413	265.0	0.058	128.83	413	265.0	0.360	126.81	413	265.0	0.135					
123.83	413	265.0	0.004	129.81	412	265.0	0.065	132.83	413	264.8	0.359	130.83	412	265.0	0.135					
127.86	413	265.0	0.004	133.81	413	265.0	0.065	136.78	412	265.0	0.354	134.80	412	265.0	0.133					
131.81	412	265.0	0.004	137.81	413	265.0	0.061	140.80	413	264.8	0.357	138.85	413	264.8	0.137					
135.81	412	265.0	0.004	141.85	413	264.8	0.065	144.83	412	264.8	0.353	142.81	412	264.8	0.132					
139.85	412	265.0	0.004	145.81	412	264.8	0.060	148.81	412	264.8	0.355	146.83	412	264.8	0.134					
143.83	413	264.8	0.005	149.86	413	264.8	0.059	152.81	412	264.8	0.356	150.90	413	264.8	0.131					
147.83	413	264.8	0.004	153.81	412	264.8	0.062	156.86	413	264.8	0.353	154.85	413	264.8	0.133					
151.78	413	264.8	0.003	157.81	412	264.6	0.062	160.85	412	264.8	0.354	158.85	413	264.8	0.133					
155.85	413	264.8	0.004	161.81	413	264.6	0.059	164.90	412	264.6	0.356	162.81	412	264.6	0.136					
159.80	412	264.8	0.004	165.81	413	264.6	0.059	168.85	413	264.6	0.354	166.80	413	264.8	0.135					
163.85	412	264.6	0.004	169.80	412	264.8	0.059	172.85	412	264.6	0.358	170.83	413	264.6	0.136					
167.86	412	264.6	0.004	173.81	412	264.6	0.058					174.85	412	264.6	0.137					
171.86	413	264.6	0.004																	







## Experiment #07074

[illegible]





Methane				Oxygen				Nitrogen				Carbon Dioxide				Carbon Monoxide			
Time (min)	Temp (°C)	Press (bar)	Conc (gmol/L)	Time (min)	Temp (°C)	Press (bar)	Conc (gmol/L)	Time (min)	Temp (°C)	Press (bar)	Conc (gmol/L)	Time (min)	Temp (°C)	Press (bar)	Conc (gmol/L)	Time (min)	Temp (°C)	Press (bar)	Conc (gmol/L)
0.00	390	103.6	0.103	1.98	391	139.2	0.339	4.28	392	139.0	0.312	3.36	392	139.2	0.003	2.68	392	139.2	0.004
1.00	388	138.7	0.073	6.46	392	139.0	0.282	42.56	392	137.2	0.269	7.13	392	139.0	0.009	8.76	392	139.0	0.007
4.96	392	139.0	0.071	9.31	392	138.7	0.260	45.06	392	137.0	0.266	10.05	392	138.7	0.013	8.63	391	138.7	0.007
7.95	392	138.7	0.065	12.53	392	138.5	0.249	49.06	392	136.8	0.263	13.31	392	138.5	0.017	11.78	392	138.5	0.008
10.91	392	138.3	0.060	15.58	392	138.3	0.234	52.11	391	136.8	0.266	16.36	392	138.1	0.024	14.86	392	138.3	0.007
13.98	392	138.3	0.056	18.90	392	138.1	0.222	55.31	391	136.8	0.255	19.53	392	138.1	0.027	17.96	392	138.3	0.007
17.16	392	138.3	0.052	21.96	392	138.1	0.215	58.65	392	136.6	0.256	22.73	392	137.9	0.031	22.73	392	138.1	0.006
20.35	392	138.1	0.048	24.85	391	137.9	0.205	61.90	391	136.6	0.253	25.68	392	137.9	0.033	24.26	392	137.9	0.007
23.43	392	137.9	0.044	27.85	392	137.7	0.197	64.98	391	136.4	0.255	28.48	392	137.7	0.036	27.06	392	137.7	0.006
26.41	392	137.9	0.040	30.83	392	137.4	0.189	67.98	392	136.4	0.248	31.56	392	137.7	0.039	30.08	392	137.4	0.006
29.21	392	137.4	0.036	33.86	392	137.4	0.183	71.33	392	136.2	0.257	34.65	392	137.4	0.040	34.65	392	137.2	0.004
32.30	392	137.4	0.033	36.96	392	137.2	0.175	74.60	392	136.2	0.247	37.63	392	137.2	0.043	37.63	392	137.2	0.004
35.35	392	137.2	0.033	40.35	392	137.2	0.171	77.33	392	136.2	0.251	41.00	392	137.0	0.045	41.00	392	137.0	0.050
38.40	391	137.2	0.031	43.41	392	137.2	0.167	80.28	391	136.0	0.248	44.11	392	136.8	0.047	47.46	392	136.8	0.052
41.78	391	137.0	0.028	46.36	392	137.0	0.162	83.40	391	136.0	0.242	50.50	392	136.8	0.052	50.50	392	136.8	0.052
45.00	392	137.0	0.024	49.93	392	136.8	0.158	86.53	392	136.0	0.242	53.73	392	136.8	0.052	53.73	392	136.8	0.052
48.28	392	136.8	0.024	52.90	391	136.8	0.158	89.68	391	136.0	0.242	57.00	392	136.6	0.053	57.00	392	136.6	0.053
51.40	392	136.8	0.024	56.35	392	136.6	0.148	92.58	391	135.8	0.237	60.51	392	136.6	0.055	60.51	392	136.6	0.055
54.48	391	136.8	0.022	59.61	392	136.6	0.145	95.76	391	135.8	0.237	63.46	392	136.4	0.055	63.46	392	136.4	0.055
57.71	391	136.6	0.021	62.78	392	136.4	0.142	98.70	391	135.8	0.237	66.35	392	136.4	0.055	66.35	392	136.4	0.055
61.10	391	136.6	0.020	65.68	391	136.4	0.140	101.61	391	135.8	0.237	69.30	391	136.4	0.056	69.30	391	136.4	0.056
64.26	391	136.4	0.019	68.70	391	136.2	0.136	104.35	391	135.8	0.230	72.68	391	136.2	0.056	72.68	391	136.2	0.056
67.15	391	136.4	0.018	71.91	391	136.2	0.133	107.15	391	135.6	0.233	75.85	391	136.2	0.057	75.85	391	136.2	0.057
70.41	391	136.2	0.017	75.11	391	136.2	0.131	110.20	391	135.6	0.233	78.83	391	136.2	0.057	78.83	391	136.2	0.057
73.51	392	136.2	0.015	78.06	391	136.2	0.130	113.51	391	135.6	0.235	81.75	391	136.0	0.056	81.75	391	136.0	0.056
76.55	392	136.2	0.014	81.05	391	136.0	0.124	116.46	391	135.6	0.237	85.06	391	136.0	0.058	85.06	391	136.0	0.058
79.56	391	136.2	0.014	84.11	391	136.0	0.125	119.31	391	135.4	0.233	88.06	392	136.0	0.059	88.06	392	136.0	0.059
82.68	391	136.0	0.014	87.26	391	136.0	0.122	122.30	391	135.4	0.243	91.21	392	136.0	0.058	91.21	392	136.0	0.058
85.81	391	136.0	0.013	90.40	391	135.8	0.118	125.38	391	135.4	0.243	94.26	391	135.8	0.058	94.26	391	135.8	0.058
88.95	391	136.0	0.012	93.51	391	135.8	0.116	128.30	391	135.4	0.240	97.18	391	135.8	0.061	97.18	391	135.8	0.061
91.80	391	135.8	0.012	96.50	391	135.8	0.116	131.30	391	135.4	0.241	100.08	391	135.8	0.058	100.08	391	135.8	0.058
94.51	391	135.8	0.011	99.45	391	135.8	0.114	134.48	391	135.2	0.241	102.93	391	135.8	0.059	102.93	391	135.8	0.059
97.96	391	135.8	0.010	102.28	391	135.8	0.111	137.63	391	135.2	0.239	105.73	391	135.6	0.059	105.73	391	135.6	0.059
100.88	391	135.8	0.010	105.05	391	135.6	0.113	140.53	391	135.2	0.240	108.66	391	135.6	0.061	108.66	391	135.6	0.061
103.60	391	135.8	0.010	107.91	391	135.6	0.113	143.71	391	135.2	0.240	111.85	391	135.6	0.061	111.85	391	135.6	0.061
106.45	391	135.6	0.010	111.10	391	135.6	0.109	146.46	391	135.2	0.240	114.95	391	135.6	0.061	114.95	391	135.6	0.061
109.41	391	135.6	0.009	114.28	391	135.4	0.110	149.33	391	135.2	0.240	117.90	391	135.4	0.062	117.90	391	135.4	0.062
112.60	391	135.6	0.009	117.26	391	135.6	0.112	152.56	391	135.0	0.241	120.71	391	135.4	0.062	120.71	391	135.4	0.062
115.71	391	135.6	0.009	120.23	391	135.4	0.111	155.61	391	135.0	0.241	123.88	391	135.4	0.061	123.88	391	135.4	0.061
118.58	391	135.4	0.009	123.21	391	135.4	0.110	158.43	391	134.8	0.241	126.88	391	135.4	0.064	126.88	391	135.4	0.064
121.41	391	135.4	0.008	126.96	391	135.4	0.110	161.61	391	135.0	0.245	129.73	391	135.4	0.063	129.73	391	135.4	0.063
124.71	391	135.4	0.008	129.96	391	135.4	0.110	164.73	391	135.0	0.235	132.80	391	135.2	0.063	132.80	391	135.2	0.063
127.56	391	135.4	0.008	132.03	391	135.2	0.109					135.98	391	135.2	0.064	135.98	391	135.2	0.064
130.60	391	135.2	0.008	135.38	391	135.2	0.108					139.01	391	135.2	0.064	139.01	391	135.2	0.064
133.60	391	135.2	0.007	138.35	391	135.2	0.109					142.35	391	135.2	0.065	142.35	391	135.2	0.065
136.86	391	135.4	0.007	141.61	391	135.2	0.110					145.05	391	135.0	0.064	145.05	391	135.0	0.064
139.78	391	135.2	0.007	144.38	391	135.2	0.106					147.81	391	135.0	0.067	147.81	391	135.0	0.067
143.03	391	135.2	0.007	147.15	391	135.2	0.108					151.01	391	135.0	0.068	151.01	391	135.0	0.068
145.76	391	135.0	0.006	150.30	391	135.2	0.105					154.08	391	135.0	0.067	154.08	391	135.0	0.067
148.58	391	135.0	0.006	153.30	391	135.0	0.110					157.03	391	135.0	0.067	157.03	391	135.0	0.067
151.81	391	135.0	0.006	156.26	391	135.0	0.107					160.81	391	135.0	0.066	160.81	391	135.0	0.066
154.76	391	135.0	0.006	159.21	391	134.8	0.109					163.13	391	135.0	0.066	163.13	391	135.0	0.066
157.80	391	135.0	0.006	162.36	391	135.0	0.106					166.50	391	135.0	0.068	166.50	391	135.0	0.068
160.81	391	134.8	0.005	165.60	391	135.0	0.104												
163.98	391	135.0	0.005																
167.20	391	134.8	0.005																





## Experiment #09284

Methane				Oxygen				Nitrogen				Carbon Dioxide				Carbon Monoxide			
Time (min)	Temp (°C)	Press (bar)	Conc (gmol/L)	Time (min)	Temp (°C)	Press (bar)	Conc (gmol/L)	Time (min)	Temp (°C)	Press (bar)	Conc (gmol/L)	Time (min)	Temp (°C)	Press (bar)	Conc (gmol/L)	Time (min)	Temp (°C)	Press (bar)	Conc (gmol/L)
0.00	410	109.9	0.119	2.07	416	137.2	0.245	4.74	414	136.6	0.276	3.49	415	136.8	0.027	2.62	415	137.0	0.018
1.35	417	137.7	0.076	6.14	414	136.4	0.153	8.37	413	135.8	0.270	6.84	413	136.0	0.031	5.34	414	136.2	0.015
4.17	414	136.8	0.050	10.10	413	135.6	0.119	13.10	412	135.2	0.267	11.10	412	135.4	0.069	9.10	413	135.8	0.011
7.54	413	136.0	0.037	15.09	412	135.0	0.088	18.10	411	134.8	0.260	11.10	412	135.4	0.069	14.09	412	135.2	0.007
12.10	412	135.4	0.025	20.10	411	134.8	0.073	23.10	411	134.6	0.258	16.17	412	135.0	0.081	19.15	412	134.8	0.005
17.07	412	134.8	0.018	25.10	411	134.3	0.063	28.10	411	134.3	0.258	21.12	411	134.6	0.088	24.17	411	134.6	0.005
22.10	411	134.6	0.013	30.10	411	134.3	0.055	33.10	411	134.1	0.253	26.10	411	134.3	0.092	29.17	411	134.3	0.003
27.14	411	134.3	0.009	35.14	411	134.1	0.052	38.10	411	134.1	0.254	31.12	411	134.1	0.098	34.20	411	134.1	0.004
32.10	411	134.1	0.007	40.12	411	133.9	0.049	43.10	411	133.9	0.252	36.10	411	134.1	0.097	39.20	411	133.9	0.004
37.10	411	134.1	0.005	45.12	411	133.9	0.046	48.14	411	133.9	0.252	41.10	411	134.1	0.102	44.10	410	133.9	0.002
42.10	411	134.1	0.005	50.14	411	133.7	0.045	53.14	411	133.7	0.255	46.12	411	133.9	0.103	49.15	411	133.9	0.002
47.14	411	133.9	0.004	55.10	411	133.7	0.043	58.19	410	133.7	0.256	51.09	411	133.9	0.103	54.10	411	133.9	0.002
52.17	410	133.7	0.004	60.12	410	133.7	0.042	63.09	411	133.7	0.256	56.12	411	133.7	0.103	59.12	411	133.7	0.002
57.14	410	133.7	0.003	65.10	411	133.7	0.040	68.10	410	133.7	0.252	61.10	411	133.7	0.104	64.14	411	133.7	0.001
62.14	410	133.7	0.003	70.14	411	133.7	0.041	73.25	411	133.7	0.248	66.19	410	133.7	0.105	69.20	411	133.7	0.002
67.10	410	133.7	0.002	75.09	411	133.7	0.038	78.09	410	133.7	0.250	71.12	411	133.7	0.103	74.10	411	133.7	0.002
72.12	411	133.7	0.002	80.32	410	133.7	0.038	83.14	411	133.7	0.251	76.14	411	133.7	0.104				
77.15	411	133.7	0.002	85.10	410	133.7	0.038	88.09	411	133.7	0.251	81.19	411	133.7	0.104				
82.10	410	133.7	0.002	89.15	411	133.7	0.038	92.10	410	133.5	0.251	85.10	410	133.5	0.105				
87.09	411	133.7	0.002	93.09	410	133.7	0.039	96.10	411	133.5	0.251	89.10	410	133.7	0.106				
91.22	411	133.7	0.002	97.20	410	133.7	0.037	100.12	410	133.7	0.247	93.09	411	133.7	0.106				
95.09	410	133.7	0.002	101.10	411	133.5	0.037	104.09	410	133.7	0.249	96.15	411	133.7	0.107				
99.12	411	133.7	0.002	105.09	411	133.5	0.037	108.15	411	133.5	0.249	102.14	410	133.7	0.106				
103.17	411	133.7	0.001	109.12	410	133.7	0.037	112.10	410	133.5	0.250	106.15	411	133.7	0.107				
107.10	410	133.7	0.002	113.10	411	133.5	0.037	116.10	411	133.5	0.246	110.14	411	133.5	0.107				
111.10	410	133.5	0.002	117.09	411	133.5	0.034	120.09	411	133.5	0.251	114.15	411	133.5	0.104				
115.07	411	133.5	0.001	121.09	410	133.5	0.036	124.12	410	133.5	0.246	118.09	410	133.5	0.107				
119.10	410	133.5	0.001	125.09	410	133.5	0.036					122.09	411	133.5	0.103				
123.10	411	133.5	0.001									126.10	411	133.5	0.105				

## Experiment #10034

Methane				Oxygen				Nitrogen				Carbon Dioxide				Carbon Monoxide			
Time (min)	Temp (°C)	Press (bar)	Conc (gmol/L)	Time (min)	Temp (°C)	Press (bar)	Conc (gmol/L)	Time (min)	Temp (°C)	Press (bar)	Conc (gmol/L)	Time (min)	Temp (°C)	Press (bar)	Conc (gmol/L)	Time (min)	Temp (°C)	Press (bar)	Conc (gmol/L)
0.00	410	111.6	0.142	1.99	416	137.4	0.216	4.65	414	136.6	0.261	3.45	415	136.8	0.038	2.55	415	137.2	0.020
1.20	418	137.9	0.084	6.04	413	136.2	0.124	8.62	412	135.6	0.251	6.65	413	136.2	0.065	5.27	414	136.4	0.016
4.07	414	136.8	0.057	10.62	412	135.4	0.081	13.60	411	135.0	0.244	11.62	412	135.4	0.082	9.70	412	135.6	0.010
7.65	412	135.8	0.042	16.00	411	135.0	0.053	18.62	411	134.6	0.244	16.72	411	134.8	0.094	14.64	411	135.0	0.007
12.60	411	135.2	0.029	20.64	411	134.6	0.039	23.62	411	134.3	0.240	21.62	411	134.3	0.103	19.70	411	134.3	0.007
17.62	411	134.8	0.021	25.64	410	134.3	0.030	26.67	410	134.1	0.238	26.62	410	134.1	0.110	24.62	411	134.3	0.005
22.62	411	134.6	0.015	30.85	410	134.1	0.021	33.62	410	133.9	0.240	31.64	410	134.1	0.112	29.74	411	134.1	0.004
32.64	410	134.1	0.012	35.64	411	133.9	0.016	38.62	411	133.7	0.235	36.62	410	133.9	0.115	34.70	410	133.9	0.004
37.64	410	133.9	0.009	40.70	411	133.7	0.014	43.64	410	133.7	0.242	41.62	410	133.7	0.118	39.69	410	133.7	0.004
42.64	410	133.7	0.008	45.62	410	133.7	0.012	48.64	410	133.5	0.240	46.62	410	133.7	0.119	44.65	410	133.7	0.003
47.60	410	133.7	0.007	50.62	410	133.7	0.009	53.64	410	133.5	0.234	51.64	410	133.7	0.120	49.72	410	133.7	0.003
52.65	410	133.7	0.006	55.62	410	133.7	0.008	58.64	410	133.5	0.237	56.65	410	133.7	0.120	54.72	410	133.5	0.002
57.64	410	133.7	0.005	60.60	410	133.5	0.008	63.62	410	133.5	0.237	61.57	410	133.5	0.119	59.65	410	133.7	0.002
62.62	410	133.5	0.005	65.64	410	133.5	0.006	68.64	410	133.5	0.229	66.62	410	133.5	0.121	64.69	410	133.5	0.002
67.60	410	133.5	0.005	70.60	410	133.5	0.004	73.60	410	133.5	0.233	71.67	410	133.5	0.120	69.64	410	133.5	0.002
72.60	410	133.5	0.005	75.62	410	133.5	0.004	78.60	410	133.5	0.233	76.62	410	133.5	0.120	74.70	410	133.5	0.002
77.62	410	133.5	0.004	80.64	410	133.5	0.005	83.62	410	133.3	0.233	81.62	410	133.5	0.120	79.70	410	133.5	0.003
82.64	410	133.5	0.004	85.62	410	133.3	0.005	88.62	410	133.3	0.233	86.59	410	133.3	0.122	84.69	410	133.5	0.002
87.62	410	133.3	0.004	90.70	410	133.3	0.003	93.60	410	133.3	0.231	91.64	410	133.5	0.120	89.65	410	133.5	0.002
92.62	410	133.5	0.004	95.60	410	133.3	0.001	98.62	410	133.5	0.235	96.65	410	133.5	0.121	94.69	410	133.3	0.002
97.67	410	133.3	0.004	100.64	410	133.5	0.003	103.62	410	133.3	0.232	101.64	410	133.3	0.120	99.62	410	133.3	0.002
102.60	410	133.3	0.004	105.62	410	133.5	0.000	108.62	410	133.3	0.235	106.60	410	133.3	0.122	104.67	410	133.3	0.002
107.60	410	133.3	0.004	110.62	410	133.3	-0.001	113.62	410	133.3	0.235	111.60	410	133.3	0.122	109.70	410	133.3	0.002
112.64	410	133.3	0.004	115.87	410	133.3	0.001	118.62	410	133.3	0.230	116.64	410	133.3	0.120	114.67	410	133.3	0.001
117.60	410	133.3	0.004	120.60	410	133.3	0.000					121.60	410	133.3	0.122	119.69	410	133.3	0.002

## Experiment #10074a

Methane				Oxygen				Nitrogen				Carbon Dioxide				Carbon Monoxide			
Time (min)	Temp (°C)	Press (bar)	Conc (gmol/L)	Time (min)	Temp (°C)	Press (bar)	Conc (gmol/L)	Time (min)	Temp (°C)	Press (bar)	Conc (gmol/L)	Time (min)	Temp (°C)	Press (bar)	Conc (gmol/L)	Time (min)	Temp (°C)	Press (bar)	Conc (gmol/L)
0.00	410	111.8	0.121	1.70	417	138.1	0.157	5.43	414	136.6	0.192	3.33	415	137.4	0.016	3.33	415	137.4	0.016
0.97	417	138.7	0.090	6.10	413	136.4	0.065	8.37	413	136.0	0.185	7.10	413	136.2	0.060	9.18	413	135.8	0.012
4.82	414	136.8	0.048	10.02	413	135.6	0.030	12.13	413	135.4	0.182	10.75	413	135.6	0.069	12.88	412	135.2	0.009
7.72	413	136.0	0.037	14.92	412	135.2	0.005	16.88	412	134.8	0.176	15.57	412	135.0	0.083	17.60	411	134.8	0.007
11.40	412	135.4	0.028	18.33	411	134.8	-0.003	20.40	411	134.6	0.177	19.00	411	134.8	0.084	21.50	411	134.6	0.006
16.23†	412	135.0	0.021	22.28	411	134.6	-0.001	25.27	411	134.6	0.176	23.28	411	134.6	0.087	26.37	411	134.6	0.006
19.63	411	134.8	0.021	27.28	411	134.6	-0.001	30.28	410	134.6	0.176	28.28	411	134.3	0.085	31.35	411	134.6	0.004
24.28	411	134.6	0.022	32.28	411	134.3	-0.002	35.28	411	134.6	0.176	33.35	411	134.6	0.087	36.28	410	134.6	0.004
29.28	410	134.6	0.023																
34.28	410	134.6	0.024																

†Discard points at later times due to depletion of oxygen

## Experiment #10074b

[illegible]

## Experiment #10114

Methane				Oxygen				Nitrogen				Carbon Dioxide				Carbon Monoxide			
Time (min)	Temp (°C)	Press (bar)	Conc (gmol/L)	Time (min)	Temp (°C)	Press (bar)	Conc (gmol/L)	Time (min)	Temp (°C)	Press (bar)	Conc (gmol/L)	Time (min)	Temp (°C)	Press (bar)	Conc (gmol/L)	Time (min)	Temp (°C)	Press (bar)	Conc (gmol/L)
0.00	410	41.8	0.115	1.55	418	70.0	0.208	4.45	414	69.8	0.225	3.04	415	70.0	0.012	2.19	416	70.0	0.015
0.84	410	69.8	0.071	6.09	413	69.8	0.145	8.30	412	69.6	0.218	6.79	413	69.6	0.029	5.24	413	69.8	0.016
3.79	414	69.8	0.058	10.10	412	69.6	0.121	12.42	412	69.4	0.215	10.79	412	69.4	0.041	9.14	413	69.6	0.014
7.59	413	69.6	0.048	14.44	412	69.4	0.101	17.44	412	69.1	0.214	15.45	412	69.4	0.048	13.50	412	69.4	0.011
11.60	412	69.4	0.040	19.44	412	68.9	0.084	22.44	412	68.9	0.213	20.42	412	68.9	0.058	18.57	412	69.1	0.008
16.44	412	69.1	0.033	24.42	412	68.7	0.070	27.44	411	68.7	0.211	23.42	411	68.9	0.065	23.42	411	68.9	0.007
21.42	412	68.9	0.027	32.85	411	68.7	0.055	30.70	411	68.9	0.209	33.59	411	68.7	0.073	28.50	411	68.9	0.007
26.45	411	68.7	0.022	37.44	411	68.5	0.049	35.40	411	68.7	0.209	38.47	411	68.7	0.077	31.94	411	68.7	0.006
31.42	411	68.7	0.022	42.42	410	68.7	0.044	40.44	411	68.5	0.212	43.45	411	68.5	0.079	36.52	411	68.7	0.004
36.42	411	68.7	0.016	47.50	411	68.5	0.038	45.44	411	68.5	0.210	48.40	411	68.5	0.082	41.52	411	68.5	0.004
41.40	411	68.5	0.014	52.44	411	68.5	0.036	50.44	411	68.5	0.208	53.44	411	68.5	0.084	46.44	411	68.5	0.005
46.40	411	68.5	0.012	57.45	411	68.5	0.031	55.50	410	68.5	0.205	58.45	411	68.5	0.086	51.52	411	68.5	0.004
51.44	410	68.5	0.010	62.44	411	68.5	0.030	60.44	411	68.5	0.204	63.45	411	68.5	0.086	56.52	411	68.3	0.004
56.44	410	68.5	0.008	67.45	410	68.5	0.029	65.47	410	68.3	0.204	68.45	410	68.3	0.090	61.52	411	68.5	0.003
61.44	410	68.5	0.007	72.44	410	68.3	0.025	70.45	411	68.5	0.201	73.42	411	68.3	0.090	66.44	411	68.3	0.003
66.44	410	68.3	0.007	77.42	410	68.3	0.023	75.44	410	68.3	0.209	78.45	410	68.3	0.090	71.50	410	68.3	0.003
71.42	410	68.3	0.006	82.44	410	68.3	0.023	80.47	410	68.3	0.207	83.44	410	68.3	0.092	76.44	410	68.3	0.003
76.44	410	68.3	0.005	87.44	410	68.3	0.019	85.44	410	68.3	0.208	88.44	410	68.3	0.092	81.45	410	68.3	0.002
81.44	410	68.3	0.005	92.44	410	68.3	0.020	90.44	410	68.3	0.210	93.44	410	68.3	0.092	86.50	410	68.3	0.002
86.44	410	68.3	0.004	97.45	410	68.3	0.020	95.42	410	68.1	0.208	98.45	410	68.1	0.090	91.52	410	68.3	0.002
91.44	411	68.3	0.004	102.40	411	68.3	0.020	100.44	410	68.1	0.209	103.44	410	68.1	0.092	96.50	411	68.1	0.003
96.45	410	68.3	0.003	107.42	410	68.1	0.017	105.45	410	68.1	0.207	108.45	410	68.3	0.094	101.44	410	68.1	0.002
101.44	410	68.1	0.003	112.42	410	68.1	0.020	110.45	410	68.1	0.205	113.50	410	68.1	0.093	106.50	410	68.1	0.002
106.45	410	68.1	0.003	117.44	410	68.3	0.018	115.44	410	68.1	0.206	118.44	410	68.1	0.091	111.52	410	68.1	0.002
111.44	410	68.1	0.003													116.50	410	68.1	0.003
116.44	410	68.1	0.002														410	68.1	0.003

















## 8. References

- Alkam, M. K., Butler, P. B. and Pitz, W. J. (1995) "Methanol and Hydrogen Oxidation Kinetics in Water at Supercritical States." University of Iowa Report No. UIME PBB 95-001.
- Antal, M. J., Brittain, A., DeAlmeida, C., Ramayya, S. and Roy, J. C. (1987) "Heterolysis and Homolysis in Supercritical Water." In *Supercritical Fluids: Chemical and Engineering Principles and Applications*, Ed. T. G. Squires and M. E. Paulaitis, Washington, DC: American Chemical Society, 77-86.
- Armellini, F. J. and Tester, J. W. (1991) "Experimental Methods for Studying Salt Nucleation and Growth from Supercritical Water." *Journal of Supercritical Fluids*, **4**, 254-264.
- ASTM (1987) "Standard Guide for Evaluating Nonmetallic Materials for Oxygen Service." Report No. ASTM G 63-87.
- ASTM (1988a) "Standard Guide for Evaluating Metals for Oxygen Service." Report No. ASTM G 94-88.
- ASTM (1988b) "Standard Practice for Cleaning Methods for Material and Equipment Used in Oxygen-Enriched Environments." Report No. ASTM G 93-88.
- ASTM (1990) "Standard Guide for Designing Systems for Oxygen Service." Report No. ASTM G 88-90.
- Barner, H. E., Huang, C. Y., Johnson, T., Jacobs, G., Martch, M. A., *et al.* (1992) "Supercritical Water Oxidation: An Emerging Technology." *Journal of Hazardous Materials*, **31**, 1-17.
- Bechtold, J. K. and Margolis, S. B. (1992) "The Structure of Supercritical Diffusion Flames with Arrhenius Mass Diffusivities." *Comb. Sci. and Tech.*, **83**, 257-290.
- Bramlette, T. T., Mills, B. E., Hencken, K. R., Brynildson, M. E., Johnston, S. C., *et al.* (1990) "Destruction of DOE/DP Surrogate Wastes with Supercritical Water Oxidation Technology." Sandia National Laboratories Report No. SAND90-8229.
- Brennecke, J. F. (1993) "Spectroscopic Investigations of Reactions in Supercritical Fluids." In *Supercritical Fluid Engineering Science*, Ed. E. Kiran and J. F. Brennecke, Washington, D. C.: American Chemical Society, 201-219.



- Brown, M. S. and Steeper, R. R. (1991) "CO<sub>2</sub>-Based Thermometry of Supercritical Water Oxidation." *Appl. Spectrosc.*, **45**(10), 1733.
- Burke, S. P. and Schumann, T. E. W. (1928) "Diffusion Flames." *Ind. Eng. Chem. Res.*, **20**, 998.
- Butler, P. B., Bergan, N. E., Bramlette, T. T., Pitz, W. J. and Westbrook, C. K. (1991) "Oxidation of Hazardous Wastes in Supercritical Water: A Comparison of Modeling and Experimental Results for Methanol Destruction." *Spring Meeting of the Western States Section/The Combustion Institute*, Boulder, CO.
- Christoforakos, M. and Franck, E. U. (1986) "An Equation of State for Binary Fluid Mixtures to High Temperatures and High Pressures." *Ber. Bunsenges. Phys. Chem.*, **90**, 780-789.
- Connolly, J. F. (1966) "Solubility of Hydrocarbons in Water Near the Critical Solution Temperatures." *J. Chem. Eng. Data*, **11**(1), 13-138.
- Franck, E. U. (1979) "Sub- and Supercritical Water at High Pressure—Selected Results." In *Water and Steam*, Ed. J. Straub and K. Scheffler, New York: Pergamon Press, 465-476.
- Franck, E. U. (1987) "Fluids at High Pressures and Temperatures." *Pure and Appl. Chem.*, **59**(1), 25-34.
- Haar, L., Gallagher, J. S. and Kell, G. S. (1984) *NBS/NRC Steam Tables*. New York: Hemisphere Publishing.
- Heilig, M. and Franck, E. U. (1990) "Phase Equilibria of Multicomponent Fluid Systems to High Pressures and Temperatures." *Ber. Bunsenges. Phys. Chem.*, **94**(2), 27-35.
- Helling, R. K. and Tester, J. W. (1987) "Oxidation Kinetics of Carbon Monoxide in Supercritical Water." *Energy & Fuels*, **1**, 417-423.
- Helling, R. K. and Tester, J. W. (1988) "Oxidation of Simple Compounds and Mixtures in Supercritical Water: Carbon Monoxide, Ammonia, and Ethanol." *Environ. Sci. Technol.*, **22**, 1319-1324.
- Herzberg, G. (1945) *Molecular Spectra and Molecular Structure: II. Infrared and Raman Spectra of Polyatomic Molecules*. New York: Van Nostrand Reinhold Company, 301.
- Holgate, H. R. (1993) "Oxidation Chemistry and Kinetics in Supercritical Water: Hydrogen, Carbon Monoxide, and Glucose." Ph.D. Thesis, Massachusetts Institute of Technology.

- Holgate, H. R. and Tester, J. W. (1993) "Fundamental Kinetics and Mechanisms of Hydrogen Oxidation in Supercritical Water." *Comb. Sci. and Tech.*, **88**, 369-397.
- Holgate, H. R. and Tester, J. W. (1994a) "Oxidation of Hydrogen and Carbon Monoxide in Sub- and Supercritical Water: Reaction Kinetics, Pathways, and Water-Density Effects. 1. Experimental Results." *J. Phys. Chem.*, **98**, 800-809.
- Holgate, H. R. and Tester, J. W. (1994b) "Oxidation of Hydrogen and Carbon Monoxide in Sub- and Supercritical Water: Reaction Kinetics, Pathways, and Water-Density Effects. 2. Elementary Reaction Modeling." *J. Phys. Chem.*, **98**, 810-822.
- Holgate, H. R., Webley, P. A., Tester, J. W. and Helling, R. K. (1992) "Carbon Monoxide Oxidation in Supercritical Water: The Effects of Heat Transfer and the Water-Gas Shift Reaction on Observed Kinetics." *Energy & Fuels*, **6**(5), 586-597.
- Kee, R. J., Rupley, F. M. and Miller, J. A. (1990) "The Chemkin Thermodynamic Data Base." Sandia National Laboratories Report No. SAND87-8215B.
- Kee, R. J., Rupley, F. M. and Miller, J. A. (1991) "Chemkin-II: A Fortran Chemical Kinetics Package for the Analysis of Gas Phase Chemical Kinetics." Sandia National Laboratories Report No. SAND89-8009B.
- Lamb, W. J., Hoffman, G. A. and Jonas, J. (1981) "Self-Diffusion in Compressed Supercritical Water." *J. Chem. Phys.*, **74**, 6875.
- Lee, D.-S. and Gloyna, E. F. (1990) "Supercritical Water Oxidation of Acetamide and Acetic Acid." The University of Texas at Austin Report No. CRWR 209.
- Lee, D.-S., Li, L. and Gloyna, E. F. (1990) "Efficiency of  $H_2O_2$  and  $O_2$  in Supercritical Water Oxidation of 2,4-Dichlorophenol and Acetic Acid." *Journal of Supercritical Fluids*, **3**, 249-255.
- Levine, I. N. (1995) *Physical Chemistry*. New York: McGraw-Hill.
- Makel, D. B. and Kennedy, I. M. (1994) "Soot Formation in Laminar Inverse Diffusion Flames." *Combust. Sci. Technol.*, **97**, 303-330.
- Marquardt, D. W. (1963) "An Algorithm for Least-Squares Estimation of Nonlinear Parameters." *J. Soc. Ind. Appl. Math.*, **11**(2), 431-441.
- Marshall, W. L. and Franck, E. U. (1981) "Ion Product of Water Substance, 0-1000 °C, 1-10,000 bars." *J. Phys. Chem. Ref. Data*, **12**(2), 295-304.

- Martynova, O. I. (1976) "Solubility of Inorganic Compounds in Subcritical and Supercritical Water." In *High Temperature, High Pressure Electrochemistry in Aqueous Solutions*, Houston: National Association of Corrosion Engineers, 131-138.
- Masten, D. A., Foy, B. R., Harradine, D. M. and Dyer, R. B. (1993) "In Situ Raman Spectroscopy of Reactions in Supercritical Water." *J. Phys. Chem.*, **97**, 8557-8559.
- Modell, M. (1989) "Supercritical-Water Oxidation." In *Standard Handbook of Hazardous Waste Treatment and Disposal*, Ed. H. M. Freeman, New York: McGraw-Hill, 8.153-8.177.
- Mulholland, J. A., Sarofim, A. F. and Beér, J. M. (1992a) "Chemical Effects of Fuel Chlorine on the Envelope Flame Ignition of Droplet Streams." *Comb. Sci. and Tech.*, **85**, 405-417.
- Mulholland, J. A., Sarofim, A. F. and Beér, J. M. (1992b) "On the Derivation of Global Ignition Kinetics from a Detailed Mechanism for Simple Hydrocarbon Oxidation." *Comb. Sci. and Tech.*, **87**, 139-156.
- Norton, T. S. and Dryer, F. L. (1989) "Some New Observations on Methanol Oxidation Chemistry." *Comb. Sci. Tech.*, **63**, 107.
- Norton, T. S. and Dryer, F. L. (1992) "An Experimental and Modeling Study of Ethanol Oxidation Kinetics in an Atmospheric Pressure Flow Reactor." *International Journal of Chemical Kinetics*, **24**, 319-344.
- Peng, D.-Y. and Robinson, D. B. (1976) "A New Two-Constant Equation of State." *Ind. Eng. Chem., Fundam.*, **15**(1), 59-64.
- Pitz, W. J. (1995) "Personal communication."
- Pitz, W. J., Westbrook, C. K. and Leppard, W. R. (1991) "Autoignition Chemistry of C<sub>4</sub> Olefins under Motor Engine Conditions: A Comparison of Experimental and Modeling Results." SAE Report No. 912315.
- Reid, R. C., Prausnitz, J. M. and Poling, B. E. (1987) *The Properties of Gases and Liquids*. 4 ed., New York: McGraw-Hill, 592.
- Reynolds, W. C. (1986) "The Element Potential Method for Chemical Equilibrium Analysis: Implementation in the Interactive Program STANJAN, Version 3." Stanford University Report.
- Rice, S. F., LaJeunesse, C. A., Hanush, R. G., Aiken, J. D. and Johnston, S. C. (1994) "Supercritical Water Oxidation of Smoke, Dye, and Pyrotechnic Compositions." Sandia National Laboratories Report No. SAND94-8209.

- Rice, S. F., Steeper, R. R. and LaJeunesse, C. A. (1993) "Destruction of Representative Navy Wastes Using Supercritical Water Oxidation." Sandia National Laboratories Report No. SAND94-8203.
- Roper, F. G. (1977) "The Prediction of Laminar Jet Diffusion Flame Sizes: Part I. Theoretical Model." *Combustion and Flame*, **29**, 219-226.
- Roper, F. G., Smith, C. and Cunningham, A. C. (1977) "The Prediction of Laminar Jet Diffusion Flame Sizes: Part II. Experimental Verification." *Combustion and Flame*, **29**, 227-234.
- Schilling, W. and Franck, E. U. (1988) "Combustion and Diffusion Flames at High Pressures to 2000 bar." *Ber. Bunsenges. Phys. Chem.*, **92**, 631-636.
- Schmitt, R. G., Butler, P. B., Bergan, N. E., Pitz, W. J. and Westbrook, C. K. (1991) "Destruction of Hazardous Waste in Supercritical Water. Part II: A Study of High-Pressure Methanol Oxidation Kinetics." *Fall Meeting of the Western States Section/The Combustion Institute*, UCLA.
- Schmitt, R. G., Butler, P. B. and French, N. B. (1993) "Chemkin Real Gas: a Fortran Package for Analysis of Thermodynamic Properties and Chemical Kinetics in Nonideal Systems." University of Iowa Report No. UIME PBB 93-006.
- Schroeder, J. and Troe, J. (1987) "Elementary Reactions in the Gas-Liquid Transition Range." *Ann. Rev. Phys. Chem.*, **38**, 163-190.
- Sidebotham, G. W. (1988) "An Inverse Co-flow Approach to Sooting Laminar Diffusion Flames." Ph.D. Dissertation Thesis, Princeton University.
- Sidebotham, G. W. and Glassman, I. (1992) "Flame Temperature, Fuel Structure, and Fuel Concentration Effects on Soot Formation in Inverse Diffusion Flames." *Combustion and Flame*, **90**(3), 269-283.
- Spohn, P. D. and Brill, T. B. (1989) "Raman Spectra of the Species in Concentrated Aqueous Solutions of  $\text{Zn}(\text{NO}_3)_2$ ,  $\text{Ca}(\text{NO}_3)_2$ ,  $\text{Cd}(\text{NO}_3)_2$ ,  $\text{LiNO}_3$ , and  $\text{NaNO}_3$  up to 450 °C and 30 MPa." *J. Phys. Chem.*, **93**, 6224.
- Steeper, R. R. and Rice, S. F. (1994) "Optical Monitoring of the Oxidation of Methane in Supercritical Water." *Western States Section/The Combustion Institute*, Davis, CA, March 21-22.
- Steeper, R. R., Rice, S. F., Brown, M. S. and Johnston, S. C. (1992a) "Methane and Methanol Diffusion Flames in Supercritical Water." *Journal of Supercritical Fluids*, **5**(4), 262-268.

- Steeper, R. R., Rice, S. F., Brown, M. S. and Johnston, S. C. (1992b) "Methane and Methanol Diffusion Flames in Supercritical Water." Sandia National Laboratories Report No. SAND92-8474.
- Sychev, V. V., Vasserman, A. A., Zagoruchenko, V. A., Kozlov, A. D., Spiridonov, G. A., *et al.* (1987) *Thermodynamic Properties of Methane*. Washington: Hemisphere Publishing.
- Tester, J. W., Holgate, H. R., Armellini, F. J., Webley, P. A., Killilea, W. R., *et al.* (1993a) "Supercritical Water Oxidation Technology: Process Development and Fundamental Research." In *Emerging Technologies in Hazardous Waste Management III*, Ed. D. W. Tedder and F. G. Pohland, ACS Symposium Series, Washington, DC: American Chemical Society.
- Tester, J. W., Webley, P. A. and Holgate, H. R. (1993b) "Revised Global Kinetic Measurements of Methanol Oxidation in Supercritical Water." *Ind. Eng. Chem. Res.*, 236-239.
- Thomason, T. B. and Modell, M. (1984) "Supercritical Water Destruction of Aqueous Wastes." *Hazardous Waste*, 1, 453.
- Thornton, T. D. and Savage, P. E. (1990) "Phenol Oxidation in Supercritical Water." *Journal of Supercritical Fluids*, 3, 240-248.
- Thornton, T. D. and Savage, P. E. (1992) "Kinetics of Phenol Oxidation in Supercritical Water." *AIChE Journal*, 38(3), 321-327.
- Uematsu, M. and Franck, E. U. (1980) "Static Dielectric Constant of Water and Steam." *J. Phys. Chem. Ref. Data*, 15(3), 1087-1279.
- Warnatz, J. (1984) "Chemistry of High Temperature Combustion of Alkanes up to Octane." *Twentieth Symposium (International) on Combustion*, 845-856.
- Webley, P. A. (1989) "Fundamental Oxidation Kinetics of Simple Compounds in Supercritical Water." Ph.D. Thesis, Massachusetts Institute of Technology.
- Webley, P. A. and Tester, J. W. (1989) "Fundamental Kinetics of Methanol Oxidation in Supercritical Water." In *Supercritical Fluid Science and Technology*, Ed. K. P. Johnston and J. M. L. Penninger, Washington, DC: American Chemical Society, 259-275.
- Webley, P. A. and Tester, J. W. (1991) "Fundamental Kinetics of Methane Oxidation in Supercritical Water." *Energy & Fuels*, 5, 411-419.
- Webley, P. A., Tester, J. W. and Holgate, H. R. (1991) "Oxidation Kinetics of Ammonia and Ammonia-Methanol Mixtures in Supercritical Water in the Temperature Range 530-700°C at 246 bar." *Ind. Eng. Chem. Res.*, 30, 1745-1754.

- Wightman, T. J. (1979) "Studies in Supercritical Wet Air Oxidation." M. S. Thesis, University of California, Berkeley.
- Wilk, R. D., Cernansky, N. P., Pitz, W. J. and Westbrook, C. K. (1989) "Propene Oxidation at Low and Intermediate Temperatures: A Detailed Chemical Kinetic Study." *Combustion and Flame*, **77**, 145.
- Williams, F. A. (1985) *Combustion Theory*. The Benjamin/Cummings Pub. Co, Inc.
- Yang, H. H. and Eckert, C. A. (1988) "Homogeneous Catalysis in the Oxidation of p-Chlorophenol in Supercritical Water." *Ind. Eng. Chem. Res.*, **27**, 2009.
- Yetter, R. A. and Dryer, F. L. (1991) "A Comprehensive Reaction Mechanism for Carbon Monoxide/Hydrogen/Oxygen Kinetics." *Comb. Sci. and Tech.*, **79**, 97-128.



## UNLIMITED RELEASE

## INITIAL DISTRIBUTION:

Carl Adema  
SERDP Program Office  
North Stuart Street, Suite 303  
Arlington, VA 22203

Dr. Steven J. Buelow  
CST-6  
Los Alamos National Laboratory  
Los Alamos, NM 87545

Fenton Carey, Jr.  
U.S. Department of Energy (ST-60)  
Independence Avenue, S.W.  
Room GA 155  
Washington, DC 20585

Philip C. Dell'Orco  
Explosives Technology & Safety C920  
Los Alamos National Laboratory  
Los Alamos, NM 87545

Dr. Thomas H. Dunning, Jr.  
Molecular Science Research Center  
Pacific Northwest Laboratories  
P. O. Box 999, MS K2-20  
Richland, WA 99352

John Harrison  
SERDP Program Office  
North Stuart Street, Suite 303  
Arlington, VA 22203

Dr. Albert Lee  
PHY B312  
National Institute of Standards and  
Technology  
Gaithersburg, MD 20899

Dr. Oscar Manley  
ER-15, U.S. Department Of Energy  
Germantown Rd.  
Germantown, MD 20874

Dr. Robert Marianelli  
U.S. Department Of Energy  
Germantown Rd.  
Germantown, MD 20874

Dr. William Pitz  
Lawrence Livermore National Lab  
Box 808 L-014  
Livermore, CA 94551-0808

Dr. Gregory J. Rosasco  
PHY B312  
National Institute of Standards and  
Technology  
Gaithersburgh, MD 20899

Dr. J. M. H. Levelt Sengers  
PHY A111  
National Institute of Standards and  
Technology  
Gaithersburg, MD 20899

Dr. Michael Simonson  
Oak Ridge National Laboratory  
Bldg. 4500S, MS-6110  
Box 2008  
Oak Ridge, TN 37831-6110

Dr. Wing Tsang  
CHEM A260  
National Institute of Standards and  
Technology  
Gaithersburgh, MD 20899



Dr. Charles Westbrook  
Lawrence Livermore National Lab  
Box 808 L-014  
Livermore, CA 94551-0808

Jim Hurley  
USAF AL/EQS  
Barnes Drive, Suite 8000  
Tyndall Air Force Base, FL 32403

Richard Kirts  
Naval Civil Engineering Lab  
Laboratory Dr.  
Port Hueneme, CA 93043-4328

Crane Robinson  
Armament Research Development  
& Engineering Center (ARDEC)  
SMCAR-AES-P  
Building 321  
Picatinny Arsenal, NJ 07806-5000

Dr. Peter Schmidt  
Office of Naval Research  
Chemistry Division  
North Quincy Street  
Arlington, VA 22217-5660

Dr. Robert Shaw  
Chemical & Biological Sciences Div.  
Army Research Office  
Research Triangle Park, NC 27709

Dr. Martin A. Abraham  
Dept. of Chemical Engineering  
The University of Tulsa  
South College Avenue  
Tulsa, OK 74104-3189

Prof. Michael J. Antal, Jr.  
Hawaii Natural Energy Institute  
University of Hawaii at Manoa  
Honolulu, Hawaii 96822

Prof. Richard K. Chang  
Department of Applied Physics  
Yale University  
P. O. Box 208284  
New Haven, CT 06520-8284

Prof. Joseph W. Bozzelli  
Dept. of Chemical Engineering  
New Jersey Institute of Technology  
Newark, NJ 07102

Prof. Joan F. Brennecke  
University of Notre Dame  
Dept. of Chemical Engineering  
Notre Dame, IN 46556

Prof. Thomas Brill  
Dept. of Chemistry  
University of Delaware  
Newark, DE 19716

Dr. Kenneth Brezinsky  
Dept. of Mechanical and Aerospace  
Engineering  
Princeton University  
P. O. Box CN5263  
Princeton, NJ 08544-5263

Prof. Daniel Chang  
Dept. of Civil and Environmental  
Engineering  
University of California, Davis  
Davis, CA 95616

Prof. Charles A. Eckert  
Schools of Chemical Engineering and  
Chemistry  
Georgia Institute of Technology  
Atlanta, GA 30332-0100

Dr. Earnest F. Gloyna  
Environmental and Health Engr.  
University of Texas at Austin  
Austin, TX 78712

Prof. Michael R. Hoffmann  
Environmental Engineering Science  
California Institute of Technology  
Pasadena, CA 91125

Prof. Keith P. Johnston  
Dept. of Chemical Engineering  
University of Texas at Austin  
Austin, TX 78712

Prof. Ian Kennedy  
Dept. of Mechanical and  
Aeronautical Engineering  
University of California, Davis  
Davis, CA 95616

Prof. Michael T. Klein  
Dept. of Chemical Engineering  
University of Delaware  
Newark, DE 19716

Prof. Thomas. A. Litzinger  
Dept. of Mechanical Engineering  
Penn State University  
University Park, PA 16802

Prof. Mark A. McHugh  
Dept. of Chemical Engineering  
Johns Hopkins University  
Baltimore, MD 21218

Prof. Reginald Mitchell  
Dept. of Mechanical Engineering  
Stanford University  
Stanford, CA 94305

Prof. Howard B. Palmer  
The Pennsylvania State University  
Academic Projects Building  
University Park, PA 16802-2303

Dr. William Peters  
Energy Laboratory  
Massachusetts Inst. of Technology  
Massachusetts Avenue E40-451  
Cambridge, MA 02139-4307

Prof. Adel F. Sarofim  
Dept. of Chemical Engr. 66-466  
Massachusetts Inst. of Technology  
Massachusetts Avenue  
Cambridge, MA 02139

Dr. Phillip E. Savage  
Dept. of Chemical Engineering  
University of Michigan  
Ann Arbor, MI 48109-2136

Prof. Jan V. Sengers  
Institute for Physical Sciences and  
Technology  
University of Maryland  
College Park, MD 20742

Prof. Jefferson W. Tester  
Energy Laboratory  
Massachusetts Inst. of Technology  
Massachusetts Avenue  
Cambridge, MA 02139

Trienel Ahearn  
Labat-Anderson Incorporated  
Westpark Dr.  
Suite 4000  
McLean, VA 22102

K. S. Ahluwalia  
Foster Wheeler Development Corp.  
Engineering Science & Technology  
Peach Tree Hill Road  
Livingston, NJ 07039